# Chapter 1 Introduction

Nanotechnology is not a new technology, but a new concept for materials and devices fabrication process. The most important key point of the technique for fabrication of nanomaterials is how to control process parameters correctly. Nanomaterials are always sensitive to the parameters of the fabrication process. In order to control the uniformity of the nanomaterials dimensional size and material ordering, the concepts of self-assembly and bottom-up processes are introduced in the nanomaterials fabrication.

Recently, the fabrication of nanowires by non-lithographic methods such as ion deposition has been emphasized in the literature. Widely used ion deposition methods include, electrodeposition, vapor-phase epitaxy, thermal evaporation, thermal decomposition, and chemical vapor deposition (CVD). However, there are some process challenges associated with ion deposition methods such as, high cost of instrumentation, low yield and the need to control growth conditions carefully in order to prevent obstruction of wire growth due to blockage of pores. Furthermore, the quality of nanowires may be jeopardized by the presence of the catalyst required by the ion deposition process. In addition, these techniques are highly dependent on finding the appropriate chemical precursor.

Another approach that has been utilized for fabricating metallic nanowires is high pressure-high temperature injection of a liquid material into porous template. In this thesis, fabrication of Sn nanowires with 180

nm, 60 nm and 15 nm diameters were carried out by a similar pressure injection process but instead of a gas compressor the current method uses hydraulic pressure without any surfactant for impregnating the Sn melt into similar templates. We chose Sn in this study because of its potential application in electronic nanodevices.

In this thesis, the nanotemplates of anodic aluminum oxide (AAO) and anodic titanium oxide (ATO) were fabricated by an electrochemical process. The thickness and pore size of nanotemplates were controlled by the anodizing time, various solutions, applied voltages, heat treatment, and pore widening. In the template fabrication process, we discussed the mechanism of electro-polishing and anodizing oxides on the Al and Ti substrate. We also discussed, using 99.7% pure Al foil as a substrate and one-step anodization instead of 99.999% pure Al substrate and two-steps anodization to fabricate AAO. The mechanism of electropolishing and anodization were discussed, and the problems with the anodic nanotemplates were solved. AAO is a useful template for nanosphere and nanowires fabrication. We used AAO as a template for the fabrication of Sn nanospheres by thermal immersion methods and metal nanowires vacuum-hydraulic pressure method. Through various heat treatments, the metal nanowires could come out of AAO and form nanocrystals, whiskers, and nanospheres on the AAO surface. The templates (and within nanowires) images and nanomaterial characteristics of templates nanocrystals, whiskers, and nanospheres were checked by scanning electron microscopy (SEM), X-ray diffraction (XRD), differential scanning calorimetry (DSC), and transmission electron microscopy (TEM).

# Chapter 2 Literature Review

## 2.1 Nonlithographic fabrication of nano-technology

The modern science and technology of nano-materials has been studied in various disciplines including the fields of photonics [1,2], thermoelectrics [3], magnetics [4, 5], electronics [6], and biological sciences [7]. Since Iijima [8] successful growth carbon nanotube (CNT), great interest has been focused on one-dimensional materials, including nanotube and nanowire, because of their unique structure and properties as well as potential applications in electronic, mechanics, and optical devices [9]. The fabrication of structures with feature sizes smaller than 100 nm is an expensive and technically daunting task using conventional lithographic methods [10]. Therefore, it is natural to seek other possible fabrication techniques-nonlithographic methods [11] which may be better suited for mass production of nanoscale devices. While there are technological as well as economical limitation in lithography for ultra large scale integrated (ULSI) fabrication in the forthcoming stage of sub-100 nm scale, much effort has been focused on nanostructure formation by self-assembly methods. This offers a promising route to synthesize a large-area, ordered nanomaterials with high quality products, which is quite difficult to form by conventional lithographic process.

Studies of nano-techniques have addressed the fabrication of array nano-template [12-14], fabrication of nanowires [15, 16] and nanodots [17-23], measurement of optical [24, 25], magnetic [26], and electronic

characteristics [27-31] of nano-materials and the applications [32-40] of nano-materials. In nano-technology research, fabricating functional nanoscale structures and devices in a well-controlled way represents one of the most difficult challenges facing researchers and engineers. Due to the small dimensions of these nanoelements, a bottom-up self-assembly process provides a viable approach to overcoming such technological challenges.

The principal methods of fabricating nanochannel templates include bottom-up self-assembly processes of AAO [8, 13, 16], top-down nanopatterning processes of conventional photolithography-base techniques [41], scanning probe technology, and direct-write electron-beam lithography [42, 43]. However, the fabrication of structures with feature sizes smaller than 100 nm is a rather daunting task using the conventional electron beam and photolithographic techniques. The fabrication of nanomaterials with controlled size and composition is of fundamental and technological interest. The template synthesis method can produce nanomaterials of uniform size easily. In using templates to produce nanostructures, one must take into account the template's chemical, mechanical, and thermal stability, its insulating properties, the minimal diameter and uniformity of the pores, and the pore density. Aluminum anodization is one of the most controllable self-assembly processes. Anodic aluminum oxide (AAO) has received much attention, because of its high aspect ratio, uniform pore size, and ordering nanopores dispersion. Additionally, it is stable in the chemical and thermal surrounding, and an inexpensive process for fabrication. Detail on the

structure and preparation of alumina templates can be found elsewhere [44-47]. Template synthesis is an elegant chemical or thermo approach for the fabrication of nanomaterials. Several procedures have been proposed and applied to the synthesis of nanostructure materials using alumina as a template, such as electrodeposition [48], the high-pressure injection process [40], and chemical vapor deposition [49].

## 2.2 The characteristics and fabrication of nanoscal template

### 2.2.1 Electropolishing of aluminum

In order to obtain an optically level surface for fabricating nanoscale template, the substrate of aluminum surface must be electro-polished (EP) before the AAO process. Electropolishing was invented by Pierre Jacquet of France in 1929 and was first successfully applied to metallographic sample preparation in 1935 [50]. It is best suited for pure metals and single-phase alloys. On the contrary, multiphase alloys are often quite difficult because of differences in the polishing rates of the constituents. There are some important conditions for the EP. Examples of those conditions are initial surface roughness, electrolytic composition, electrolytic temperature, stirring rate of electrolyte, applied voltage, current density, and polishing time.

If the roughness of initial surface is too coarse, EP time will be long, with excessive metal removal and waviness. For the voltage, the applied voltage is determined by the curves of voltage vs. current density (I-V curve), showed as Fig. 2.1. In the curve the plateau area is the suitable parameter for the EP. Focusing on the electrolytes, it must be rigorously controlled within very narrow limits to get satisfactory results. It always contains a solvent, attacking ions solution, and a viscous solution. The solvent can be methanol ($CH_3OH$) or ethanol ($C_2H_6O$), the attack ions solution can be perchloric acid ($HClO_4$), hydrochloric acid ($HCl$), sulphuric acid ($H_2SO_4$), or phosphoric acid ($H_3PO_4$), and the viscous solution can be glycol monobutylether ($(CH_3(CH_2)_3OCH_2CH_2OH$) or

glycerine ($C_3H_5(CH_3)_2$). For the electrolyte temperature and stirring rate, when the bath temperature or stirring rate rises, the resistance of the bath decreases and the potential required to produce the plateau current density decreases. In addition, the bath viscosity decreases, making it more difficult to maintain a viscous anode layer.

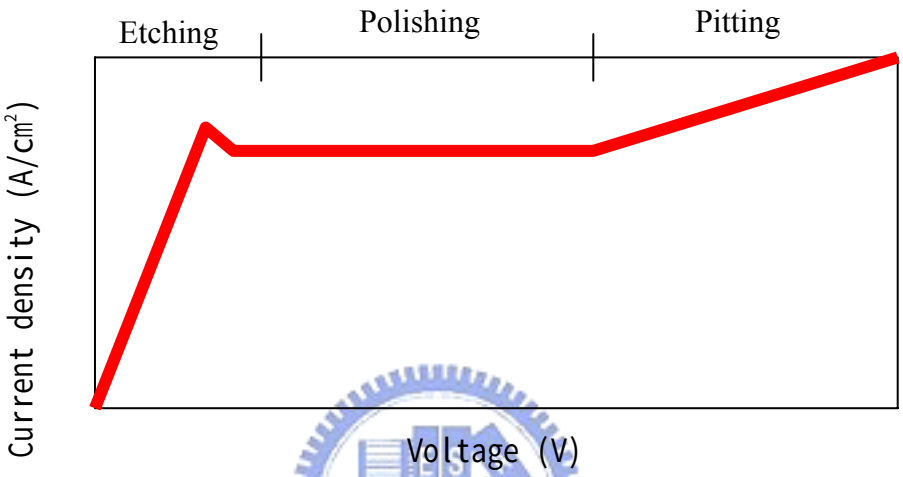


**Fig. 2.1** The I-V curve of etching, polishing and pitting sections.

### 2.2.2 Anodizing of aluminum

When anodized in an acidic electrolyte and controlled in the suitable conditions, aluminum forms a porous oxide with very uniform and parallel cell pores. Each cell contains an elongated cylindrical sub-micron or nanopore normal to the aluminum surface, extending from the surface of the oxide to the oxide/metal interface, where it is sealed by a thin barrier oxide layer with approximately hemispherical geometry. Its structure is described as a close-packed array of columnar cells. The pore diameters and pore densities of anodic alumina film can be finely controlled by appropriately carrying out the electrochemical process parameters. [51,52]. Unstable metals such as Al, Ti, Mg, Zr, Si et.al dissolve by active corrosion in many solutions and become passive. This behaviour is due to the inhibition of active dissolution by a more or less spontaneous formation a dense passive film of limited ionic conductivity. Passive films are formed from the metal itself and components of the environment, usually in water and in contact with air or anodic with water. Anodic treatments of aluminum were intensively investigated to obtain protective to decorative film on its surface. [53-57] Since the early years, anodic aluminum coloring processes at DC or AC voltage based on either chromic ($CrO_3$), sulfuric ($H_2SO_4$) or oxalic ($C_2H_2O_4$) acid as electrolytes have been paid attention to [58]. Consequently, it was observed that additives such as metal salts like copper (Cu), nikel (Ni), silver (Ag), arsenic (As), antimony (Sb), bismuth (Bi), tin (Sn), or lead (Pb) can be used to change the physical and chemical properties as well as the colors of the oxide. [59-64]

Honeycomb structures with high aspect ratios on the nanometer scale

have received interest for various applications. To obtain an nanochannel array as a template, nanoporous alumina formed by anodization has widely been studied for several decades [12, 44, 45]. Aluminum in the presence of air or aqueous electrolytes is always covered with a thin natural layer of alumina. When a positive voltage is applied to an aluminum substrate in a suitable electrolyte, pores form on the surface at almost random positions. However, under specific conditions, almost perfect hexagonally ordered pores in anodic alumina can be obtained.

Anodic alumina has called by various names; such as, anodic aluminum oxide (AAO) [65,66,72-75], anodic alumina nanoholds (AAN) [76], anodic alumina membrane (AAM) [77, 78], or porous anodic alumina(PAA) [79]. The anodizing oxide film of AAO consists of two layers: the porous thick outer layer (porous type) that grows on an inner layer (barrier type), which is thin, dense and dielectrically compact, and called the barrier layer, the active layer or the dielectric layer. The barrier layer is very thin, typically with a thickness of between 0.1 and 2% of that of the entire film [8]. Depending on the various electrolytes, anodizing time, and anodizing voltage, AAO could be formed to compact alumina, thick porous alumina, or etching types. Compact alumina (no pores) was formed in a very weak acid or neutral solution, and thickness was determined by applied voltage. Thick porous alumina formed in a medium acid solution, and thickness was determined by anodizing time. Pore density increased when anodizing time increased, but decreased when anodizing voltage increased. For etching alumina formed in strong acid or basic solutions, thickness was determined by diffusion limits of electrolyte,

and pore density increased when anodizing time increased. It is generally accepted that the thickness of barrier-type alumina is mainly determined by the applied voltage, even though there is a small deviation depending on the electrolytes and temperature. The thickness of the barrier layer is a function of the anodizing voltage (1~1.4 nm/V) [80]. The maximum attainable thickness in the barrier-type alumina film was reported to be less than 1 μm, corresponding to breakdown voltage in the range of 500~700 V (DC) [81-83]. The anodization ratio, which is defined as oxide thickness formed per voltage (nm/V), demonstrates that the barrier type films are also strongly influenced by the type of metal. For example, metals anodization ratios are: Ta (16), Nb (22), Zr (20~27), W (18), Si (4~7), and Al (10~13) [81]. Al, Ti, Ta, Nb, V, Hf, and W are classified as active metals because their surface is immediately covered with a native oxide film of a few nanometers when metals are exposed to oxygen containing surrounding. A dense of spontaneous film and high anodization ratio make those oxides as a candidate of template materials.

Between 1960 and 1990, studies by the Manchester group (led by Thompson and Wood) [45, 64-69] resulted in a deep insight in the growth mechanisms of anodic alumina oxide film. They discovered the various anions contaminate in the AAO by various electrolytes. Relatively pure alumina region to acid anion-contaminated material, which seem to increase in the order: $H_2SO_4$ >$C_2H_2O_4$ > $H_3PO_4$ > $CrO_3$. Spooner [65] presented the following composition of an alumina film anodized using sulphuric acid electrolyte; $Al_2O_3$(78.9%), $Al_2O_3 \cdot H_2O$(0.5%), $Al_2(SO_4)_3$,

$H_2O$(0.4%). Akahori [85], the melting point of the barrier oxide is near 1000 $^oC$, also the AAO template is stable around 800 $^oC$ [86] which is lower than that of bulk alumina (2017$^oC$ for $Al_2O_{3(\gamma)}$). It is believed that the low melting point of AAO than pure aluminua because of the inclusions are in the porous structure AAO. Furthermore, numerous researchers have proposed the mechanisms by which AAO. Jessensky [70] proposed a mechanical stress model to explain the formation of hexagonally-ordered pore array. It proposes that the mechanical stress at the metal/oxide interface causes repulsive force between the neighboring pores which promotes the formation of an ordered hexagonal pore array. Murray Hill [71] noted **(1)** that AAO grows by the migration of ions $OH^-$ and $O^{2-}$ through an existing film and the subsequent combination of these ions with $Al^{+3}$ to form a new oxide, and **(2)** in the deposition of an existing film, $Al^{+3}$ ions not consumed by ion migration are ejected at the film/solution interface form hydrates ions in solution. Setoh and Miyata [72] stated that the barrier layer permits the passage of oxygen formed from the water in the pores and acts continually on the aluminum to generate a new barrier film. The pores in the barrier layer are formed by anion attacks, and oxygen is locked in them. Ying [16], The voltage determines the barrier layer thickness and AAO cell size of the film. As two experience formulas can estimate the pore size and the pore distance of AAO. The pore size with voltage is: C=mV, where C is cell size (nm), V is anodizing voltage (V), and m is a constant (2~2.5). The pore distance with voltage is V=(2R-10)/2, where 2R is spacing distance (5~1000 nm).

In any electrolyte, high anodizing voltage, low electrolyte temperatures and low acid concentrations favor film growth. However, low applied voltage, high acid concentrations and high anodizing temperature favor film dissolution. When the rate of film growth has fallen to the rate of dissolution of the film in the electrolyte, the thickness of the film remains constant. Most of the very many electrolytes of AAO found in patents and the literature [16, 17, 35-37, 64, 66, 74-76] are based on an acidic solution, as Tab. 2-1. These include for example, chromic acid ($CrO_3$, 2.5~3%, 40V, 40°C), sulfuric acid ($H_2SO_4$, 15~20%, 14~22V, 18~25°C), oxalic acid ($C_2H_2O_4$, 5~10%, 50~65V, 30°C), boric acid ($H_3BO_3$, 9~15%, 50~500V, 90~95°C) and phosphoric acid ($H_3PO_4$, 10%, 10~12V, 23~25°C). Restated, the thick outer porous layer has morphology of an array of self-organized hexagonal nano-pores under suitable conditions of voltage, temperature, current density and electrolytic composition. The films formed in acid solutions below approximately 100 V are generally believed to be completely amorphous. At higher voltages, crystalline forms of γ-alumina are thought to be generated as local islands within the amorphous film.

**Tab. 2.1** The conditions of anodic to aluminum.

| Electrolyte | Time (Hr) | Applied Vol. (V) | Temp. ($^{o}$C) | Ref. |
|---|---|---|---|---|
| 0.3M ($H_2C_2O_4$) | 48 | 40 | 1 | [12] |
| 0.3M ($H_2C_2O_4$) | 10 | 40 | 5 | [13] |
| 0.3M ($H_2SO_4$) | 10 | 27 | 5 | [13] |
| 20% ($H_2SO_4$) | 24 | 18.7 | 1 | [16] |
| 15~20% ($H_2SO_4$) | - | 13~25 | 0~10 | [16] |
| 3~5% ($H_2SO_4$)+4%($H_2SO_4$) | - | - | 0~10 | [16] |
| 4~8% ($H_3PO_4$) | - | 15~120 | 0~10 | [16] |
| 15% ($H_2SO_4$) | 0.5 | 40mA/cm$^2$ | 25 | [17] |
| 0.3M ($H_2C_2O_4$) | - | 40 | 17 | [84] |
| 0.5M ($H_2SO_4$) | - | 25 | 10 | [84] |
| 0.3M ($H_2C_2O_4$): 0.3M ($H_2SO_4$)=3:2 | - | 30 | 5 | [84] |

## 2.3 Fabrication of nanowires and its application

With the continued demand for miniaturization of electronic and optical devices, nanowires with enhanced mechanical and electrical properties are needed. To develop scaled-up functional devices highly ordered nanowire arrays are essential. Many candidate materials (metals, alloys, oxides and semiconductors) were studied for various potential applications in nanotechnology and have shown some promising results. Solid metallic nanowire is a one-dimensional material. It has been exploited for a wide range of applications that take advantage of their large aspect ratio (length/diameter). The applications of metallic nanowires are desirable for wide-field sensing [87-89] and thermoelectric materials applications [90]. Further developing methods to synthesize nanowires cheaply and efficiently is of paramount importance for manufacturing future generation nanodevices.

Recently, fabricating nanowires by ion deposition or non-lightgraphic methods are emphasized in the literatures [91-95]. The ion deposition methods such as, electrodeposition [96], metalorganic vapor-phase epitaxy [97], thermal evaporation [98-100], thermal decomposition [101], physical vapor deposition (PVD) [102], and chemical vapor deposition (CVD) [103] are famous used for nanowires fabrication. The electrodeposition technique has proved to be cheaper and high yield method for producing nanowires from different materials. However, there are some drawbacks associated with most electrodeposition processes including lack of length uniformity and control. The quality of nanowires may also be jeopardized by the

presence of the conducting substrate required by the deposition processes. Another major problem with these preparation methods is that success of the processes is highly dependent on finding the appropriate chemical precursor.

Metal casting is a well-established metal processing method and has been used in metallurgy for several decades. The experiences gained from this traditional casting process combined with emerging nanotechnology methodologies can potentially be useful in keeping the cost of nanomaterials fabrication low, improve the fabrication efficiency and reduce the overall complexity of the fabrication process. Recently, a high temperature gas pressure chamber has enabled the injection of bismuth (Bi) melt into AAO template as small as 13 nm in diameter [40]. Unlike most electrodeposition methods the injection process does not require a conducting substrate or catalyst. It should be noted that the main constraint in this process is the high external pressure required to overcome the surface tension of the liquid metal melt to fill nanochannels. The smallest nanochannel that could be filled was thus compromised by the maximum pressure limit the gas chamber could sustain and operate safely. In case higher pressure was required, wetting agent was added to the Bi metal to lower the surface tension and hence reduce the required pressure to within the limit of the equipment. In the work done by Zhibo's group [40, 104], gas pressure injection process, the template was first dried and stabilized at $350^0$C for 2hr and degassed at $250^0$C for 8hr before injection. Their injection process lasted 5hr. They have stated that after injection, cooling the chamber to room temperature over a period longer than 12hr was

crucial for achieving single crystal Bi nanowires. Since the equipment they used could only sustain pressures up to 345 bar, They used wetting agents to lower the contact angle and hence the pressure required. By doing so, for an average channel diameter of 56 nm, they had improved the filling ratio to more than 90% from only 10% with out using any surfactant. Bi melt was injected into the AAO successfully by gas injecting. However, the high pressure is depends on the gas compressor. Additionally, the positive pressure chamber is expensive and dangerous to operate.

For the above problem, the process can be improved by negative pressure injected casting process when the injected casting chamber is modified. In our process, fabrication of Sn nanowires was carried out by a similar pressure injection process but instead of a gas compressor the current method uses hydraulic pressure without any surfactant for impregnating the Sn melt into similar templates. We chose Sn in this study because of its potential application in electronic nanodevices.

The study of Sn nanowires has been motivated by the attractive properties of bulk Sn and the novel properties of nanostructures such as nanowires. Bulk Sn has excellent ductility, electrical conductivity, resistance to corrosion and has been extensively used in the integrated circuit (IC) industry. Sn-based alloys are also among the most promising lead-free solders. Sn metal has low electrical resistivity ($11\times10^{-8}$ Ωm, at 298 K) [114], a low melting point (~232$^{o}$C) and high surface tension (0.544N/m, at 504 K) [115], and is weldable with Cu and Al. It is widely used as the base material of solder in the integrated circuit packaging industry. As technology moves towards manufacturing nanodevices, the

wire diameter in integrated circuits decreases to the nanometer scale; hence nanoscale solders will soon be in demand. For example, ball grid array (BGA) chips typically use a group of solder dots, or balls, to connect circuit wires. Therefore, it is of interest to develop cost-effective and efficient manufacturing methods to fabricate good quality Sn nanowires and investigate whether the attractive physical properties of the bulk Sn are maintained and also enhanced at nano scale as some theoretical predictions indicate.

## 2.4 The characteristics and fabrication of nanospheres

High-grade metal powders must meet specific quality criteria: spherical shape, high cleanliness, and homogeneous microstructure. Surfaces covered by dense arrays of nanometer-scale particles have potential applications in diverse areas such as optoelectronics, information storage, and sensing. In general, powder can be fabricated by gas atomization (GA), water atomization (WA) [105], ultrasonic gas atomization (USGA) [106], centrifugal atomization (CA) [107], laser spin atomization (LSA) [108], the rotating electrode process (REP) [109], pulverization sous vide (PSV) [110], and the rapid spinning cup (RSC) [111], or rotating perforated cup (RPC) method [112]. In the above methods, micron- and sub-micron scale powder can be fabricated easily; however, it is difficult to control particle size at the nanoscale level, size uniformity, and size distribution in a narrow range. Lithographic techniques offer the best control over nanoparticle size, shape, and spacing; however, these techniques can be expensive, limited to serial processing, and suitable to only a small number of material systems. Nanotechnologies, such as rapid solidification, plasma processing, in-situ chemical reaction, chemical vapor deposition, high-energy ball milling, and sol-gel [113], are powerful processes for fabricating a high-quality nanoparticles. Among these methods, the rapid solidification process (RSP) is an effective and cost-efficient for realizing spherical alloy particles on a substrate surface.

# Chapter 3 Experimental Procedures

## 3.1 Electropolishing (EP) of aluminum foil

Specimens of 99.999% aluminum, with dimensions 1 $cm^2$ × 0.3 mm were cut down from a $1cm^3$ specimen. Before EP, the specimens were abraded using 4000-grit SiC papers and mechanical polishing by 0.05 μm alumina powder. They were then annealed at 550 $^oC$ for 1 hour in the air furnace. After pre-treatment, the specimens used as anodic electrode as well as a platinum plate as counter electrode. Both were placed in the electrolyte with 15 vol% perchloric acid ($HClO_4$, 70%) – 70 vol% ethanol ($C_2H_6O$, 99.5%) – 15 vol% ethylene glycol monobutylether ($(CH_3(CH_2)_3OCH_2CH_2OH)$, 85%), applied 40 V and $180mA/cm^2$ in bath with stirring at 25 $^oC$ for 11 min, at a constant stirring rate of 200 rpm for EP. The electrochemical setup schematic of EP is showed in Fig. 3.1. The morphology of the aluminum surface after EP was observed by optical microscopy (OM), showed as Fig. 3.2.

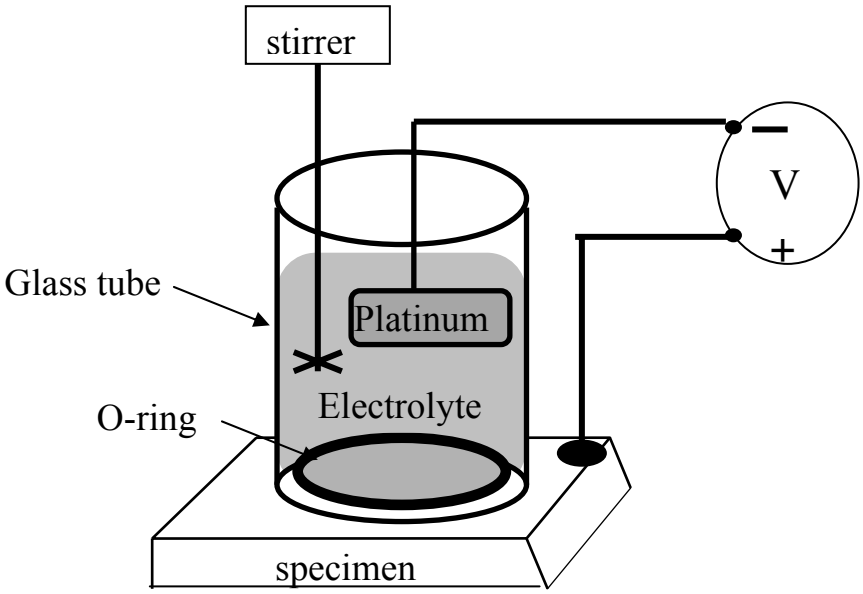


**Fig. 3.1** Schematic diagram of electropolishing and anodization setup.

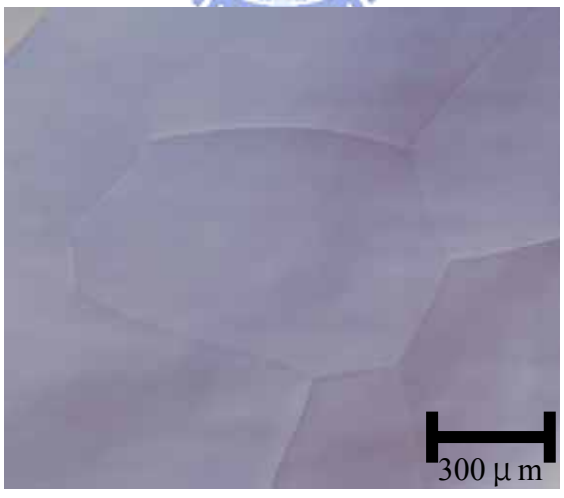


**Fig. 3.2** The optical microscopy image of aluminum surface after electropolishing.

### 3.2 Anodic Aluminum oxide (AAO)

Pore diameters of 15 nm, 60 nm and 180 nm AAO were fabricated by anodization process. The same EP equipment setup was used for fabrication AAO on Al substrate surface. The 15 nm pore size AAO were made by 10 vol% sulphuric acid ($H_2SO_4$, 98%) at 8 $^oC$, 18V; 60 nm pore size AAO were made by 3 vol% oxalic acid ($C_2H_2O_4$, 99%) at 40V, 20 $^oC$; 180 nm pore size AAO were made by 2 vol% phosphoric acid ($H_3PO_4$, 95%) at 120V, 20 $^oC$. Additionally, the AAO forming is through two-steps anodization or one-step added heat treatment processes. For two-steps anodization, the specimen was first through anodization for 30 min in the specific electrolyte of $H_2SO_4$, $C_2H_2O_4$, or $H_3PO_4$ solution. The first anodization film was remove by a mixture solution of 6 vol% $H_3PO_4$ + 1.8 wt% chromic acid ($CrO_3$) at 60$^oC$ for 40 min. Then the ordering nanopatterns will remain on the aluminum surface, showed as Fig. 3.3(a) anodization by 10 vol% $H_2SO_4$ electrolyte, and Fig. 3.3 (b) anodization by 3 wt% $C_2H_2O_4$ electrolyte, and Fig. 3.3 (c) anodization by 2 vol% $H_3PO_4$ electrolyte.

The ordering of the second anodization film will be based on the surface pattern of the aluminum substrate. Therefore, the more ordered nanochannels of AAO will form on the aluminum surface. Figure 3.4 compares the different morphology of AAO between the first anodization Fig. 3.4 (a), and the second anodization Fig. 3.4 (b) by 3 wt% $C_2H_2O_4$ electrolyte. In order to get the ordered pores on the 2$^{nd}$ anodization AAO,

AAO was put through pore widening in 5 vol% $H_3PO_4$ solution for 30 min at 30 $^oC$, as the SEM image showed in Fig. 3.5. Furthermore, the retained substrate of aluminum could be removed by a saturated copper chloride ($CuCl_2$, 99%) + 8 vol % hydrochloric acid (HCl, 95%) at 25 $^oC$; also, the AAO bottom view of barrier layer could be observed by SEM, showed as Fig. 3.6(a) by 10 vol% $H_2SO_4$ series anodization, Fig. 3.6(b) by 3 vol% $C_2H_2O_4$ series anodization, and Fig. 3.6(c) by 2 vol% $H_2PO_4$ series anodization. The flow sheet of AAO process by two step anodization is shown in Fig. 3.7.

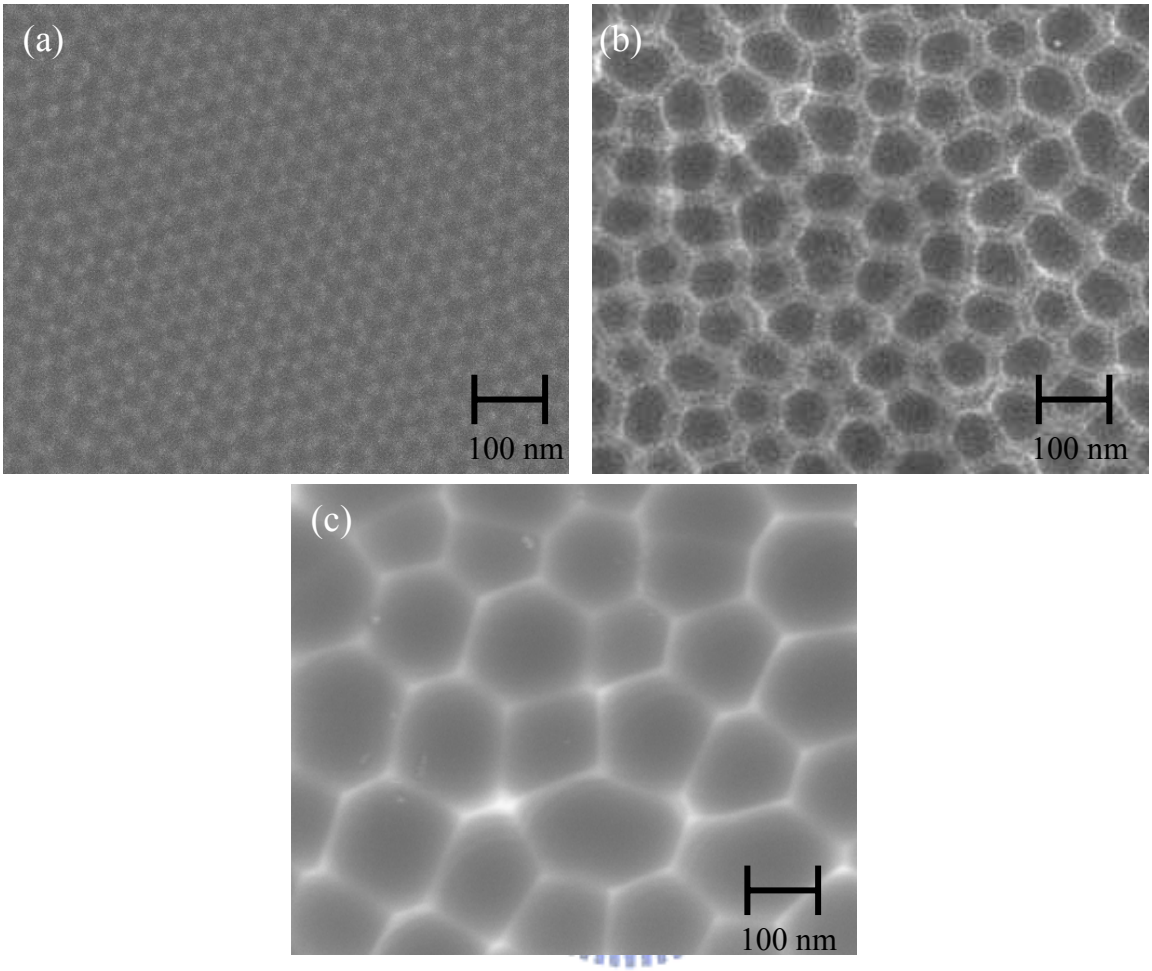


**Fig. 3.3** The first anodization films were removed by mixture of 6 vol% $H_3PO_4$ and 1.8 wt. % chromic acid ($CrO_3$) solution, the ordering nanopattern retained on the aluminum surface. The electrolyte of first anodization is by 10 % $H_2SO_4$ (a), by 3 % $C_2H_2O_4$ (b), and by 2 % $H_3PO_4$ (c).

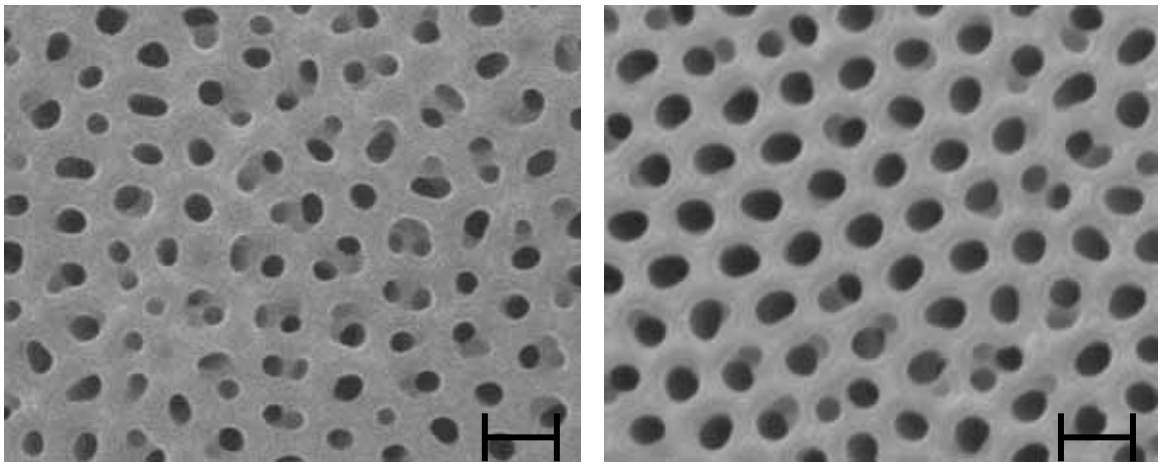


**Fig. 3.4** The surface morphology of AAO compartment between the first anodization (a), and the second anodization by 3 % oxalic acid electrolyte.

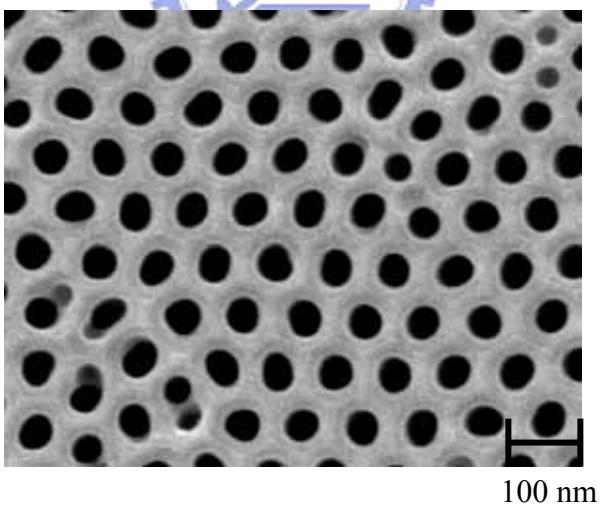


**Fig. 3.5** The SEM image of 2nd anodization AAO after pore widening by 6 % phosphoric acid.

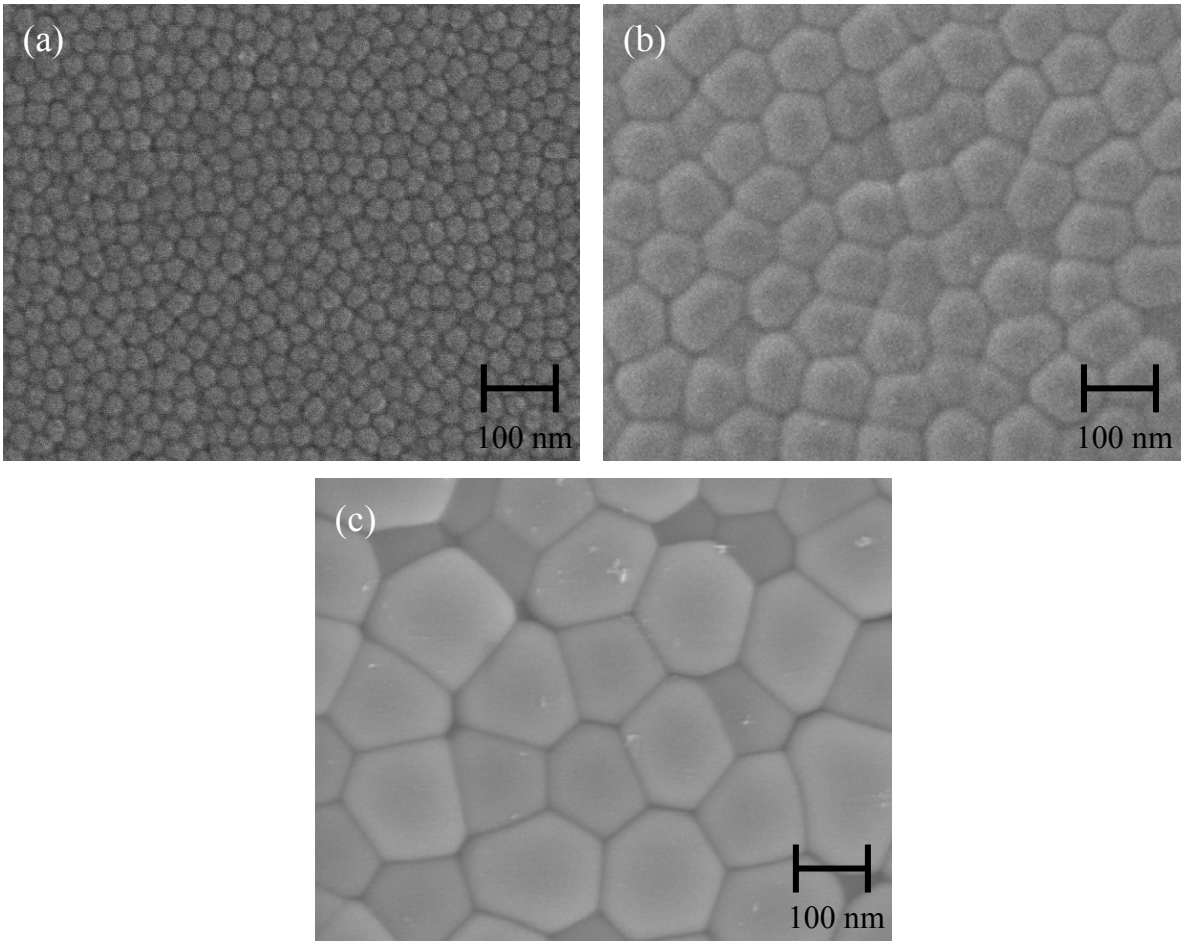


**Fig. 3.6** The SEM images of AAO bottom view of barrier layer; anodization by 10 vol. % $H_2SO_4$ electrolyte (a), anodization by 3 vol. % $H_2C_2O_4$ electrolyte (b), and anodization by 2 vol. % $H_3PO_4$ electrolyte (c).

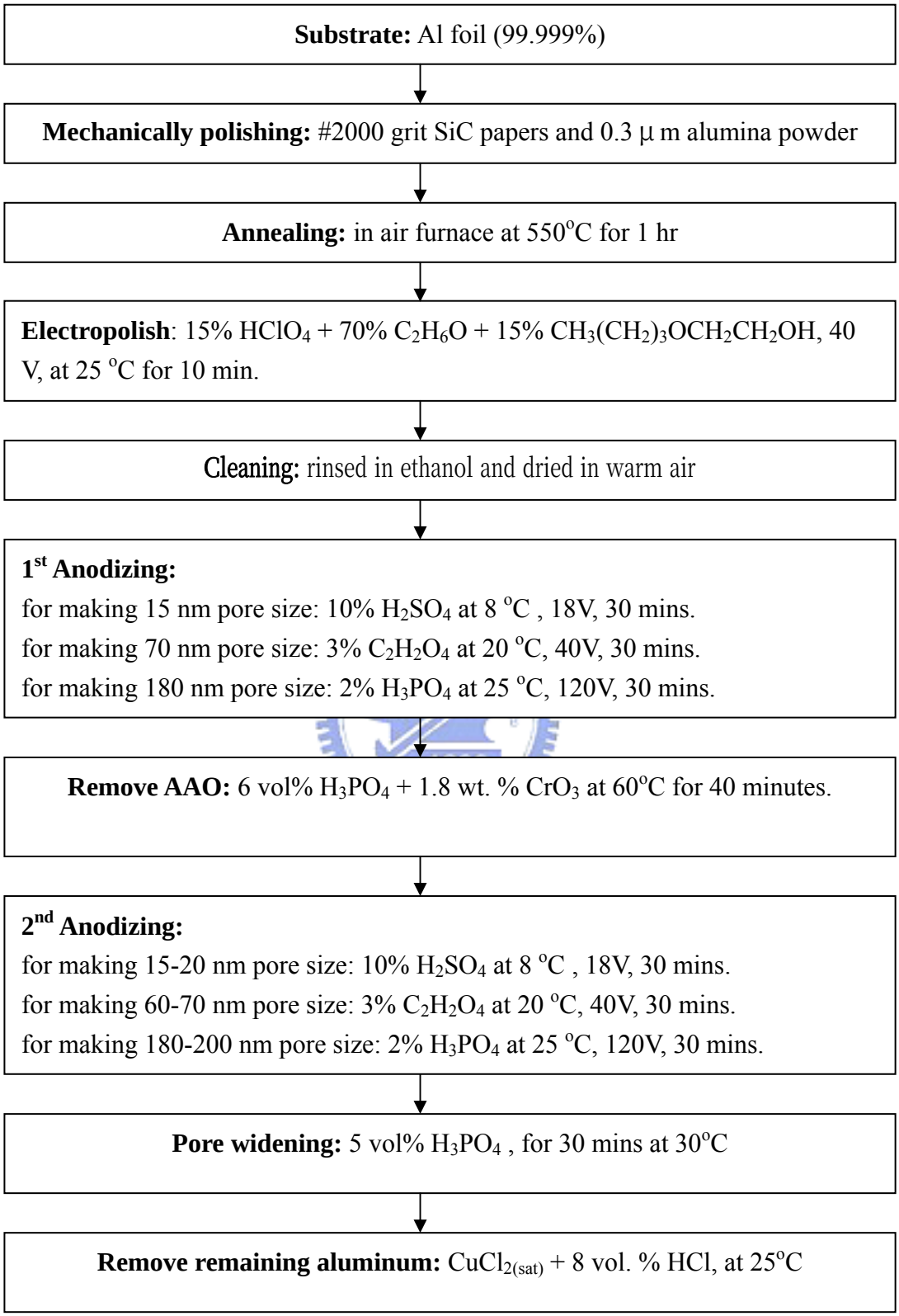


**Fig. 3.7** The flow sheet of AAO process by two steps anodization.

Based on the above EP and the 1st anodization, the AAO removal processes, and 2nd anodization steps can be replaced by the lasting annealing and pore widening process in AAO after 1st anodization. Also, the high purity (99.999%) aluminum foil could be replaced by general purity (99.7%) aluminum foil. For example, Fig. 3.8 showed the SEM image of general #1070 (99.7% purity) aluminum foil through 1st anodization, 4 hr at 600°C annealed in the air furnace, and 85 min. 5 vol% $H_3PO_4$ pore widening at 30 °C for 85min. The flow sheet of the AAO process by 99.7 % purity aluminum foil is shown in Fig. 3.9.

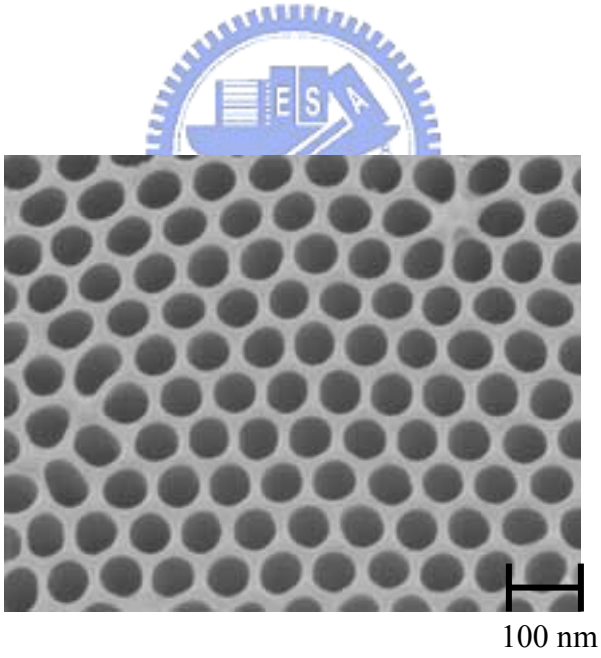


**Fig. 3.8** SEM image of AAO forming on the 99.7% purity aluminum foil through 1st anodization, 4 hr at 600°C annealed in the air furnace, and 85 min. 6 vol% $H_3PO_4$ pore widening at 30°C for 85min. processes.

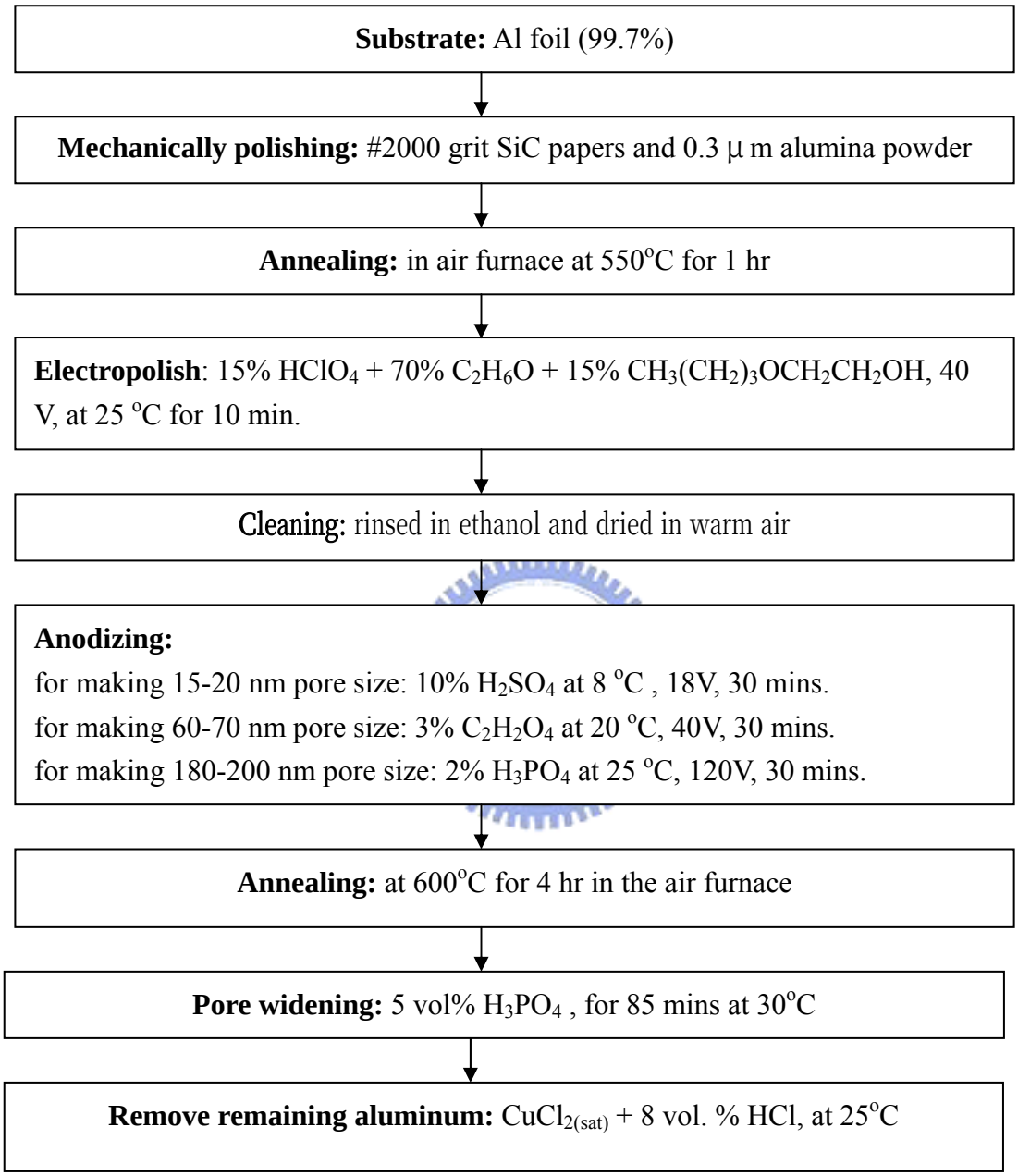


**Fig. 3.9** The flow sheet of AAO process by 99.7 % purity aluminum foil.

## 3.3 Fabrication of tin (Sn) nanowires

Hydraulic force injecting equipment, showed as Fig. 3.10, was used to fabricate the metal nanowires. The vacuum chamber and mold were made from 316L stainless steel (316L S.S.). For the process, the applied force was supplied by hydraulic force, and the argon gas was used to clean the chamber. A piece of tin (Sn) metal was on the surface of AAO and both were in the vacuum chamber where vacuum was under $10^{-3}$ torr controlled by the rotary pump. When the chamber was superheated (300$^{o}$C) up to the Sn melting temperature (232$^{o}$C), the Sn melted and spread over the AAO surface. A hydraulic force (1.2 ~3 tons) was applied on the liquid melt and the molten melt was injected into AAO (pore size with 60 nm diameter). After the molten Sn solidified in AAO, the Sn nanowires formed. The top view and cross section view of Sn in AAO were showed as Fig. 3.11 (a) and Fig. 3.11(b). The topographies of the nanowires were observed using a LEO 1530 scanning electron microscope (SEM), and JOEL 6500 SEM; the details of the morphology of the nanowires was observed using a JEOL 2010 transmission electron microscope (TEM); the composition of the nanowire was detected by PHILIPS X'Pert Pro X-ray diffraction (XRD) and Energy dispersive spectrum analysis (EDS) in JEOL JSM-2010 TEM.

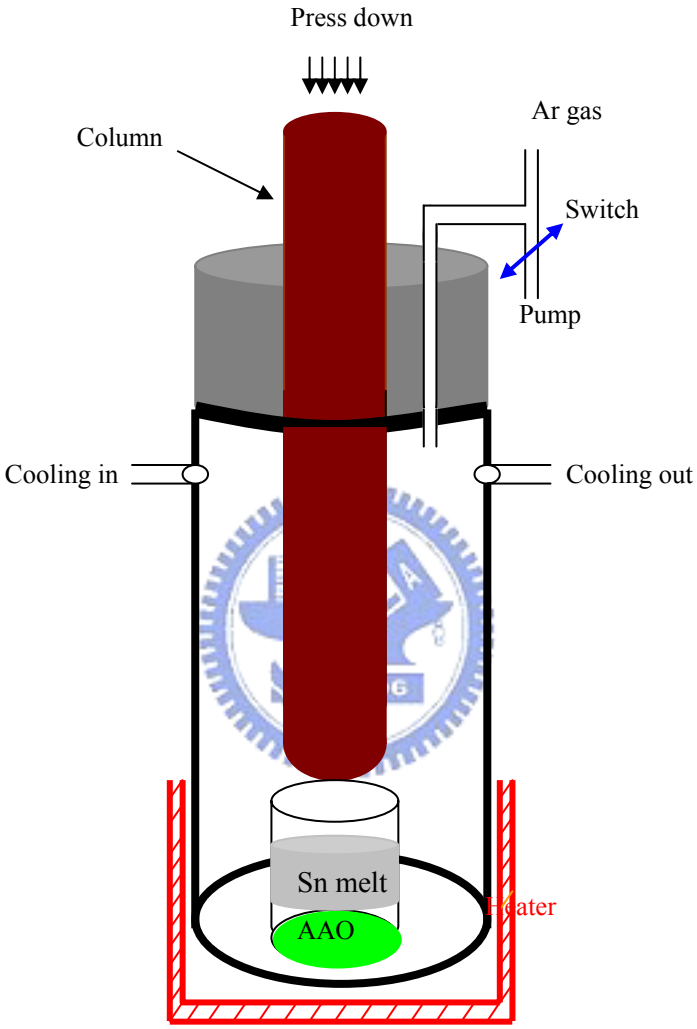


**Fig. 3.10** The experiment equipment for making metal nanowire.

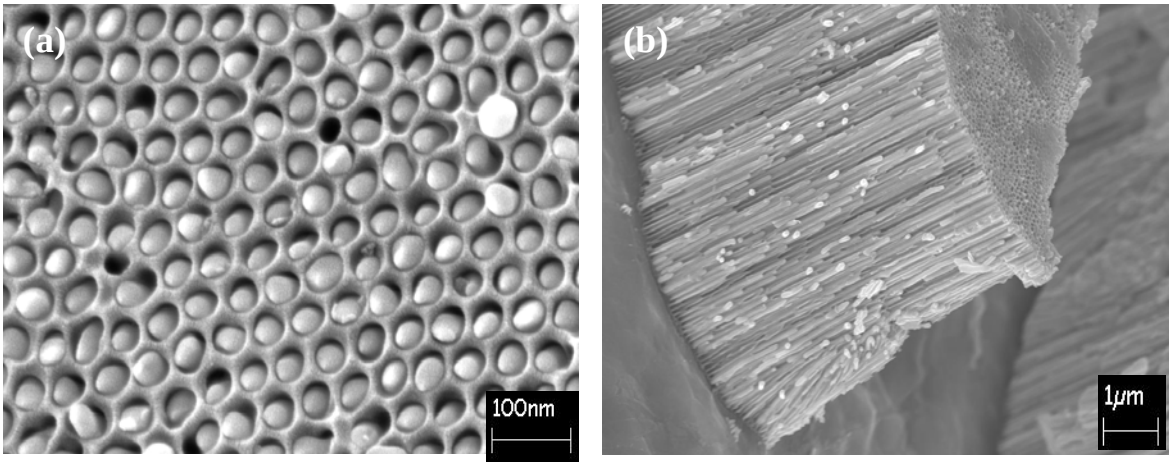


**Fig. 3.11** SEM image of Sn melt inside AAO, which formed Sn nanowires: (a) top view, (b) cross-section view.

## 3.4 Methods of nanospheres process

There are three different methods to synthesize nanospheres using AAO as a template. The methods include thermal expansion, physical vapor deposition (PVD), and thermal immersion. For the first method of thermal expansion process, tin nanowires were formed in AAO by hydraulic pressure process first. Second, the remainder of the Sn metal was removed from the AAO surface. Then, the specimen of AAO with Sn nanowires inside were reflowed in the silicate oil at 300$^{o}$C for 40 min, so the extra molten Sn could come out on the AAO because of the thermal expansion effect. When the extra molten Sn solidified, the Sn spheres formed. The SEM image of Sn nanospheres showed as Fig. 3.12. The flow sheet showed as Fig. 3.13.

The second method of PVD process, because the high surface tension difference between AAO and Sn, the Sn can be deposited on the AAO surface forming nanospheres. For example, the 10 nm thickness of Sn film deposited on 60 nm pore diameter AAO surface by E-beam formed Sn nanospheres, showed as Fig. 3.14. In the third thermal immersion process, a piece of metal was placed on the AAO surface and both were sealed in a glass tube where vacuum was under $10^{-6}$ Torr controlled by a rotary and molecular turbo pump. The melt would spread on the AAO surface when the temperature up to the melting temperature of the metal. As a result, nanoparticles nucleated and grew on the pores of AAO when the melt solidified. Figure 3.15 showed, metal nanospheres on AAO by thermal immersion process.

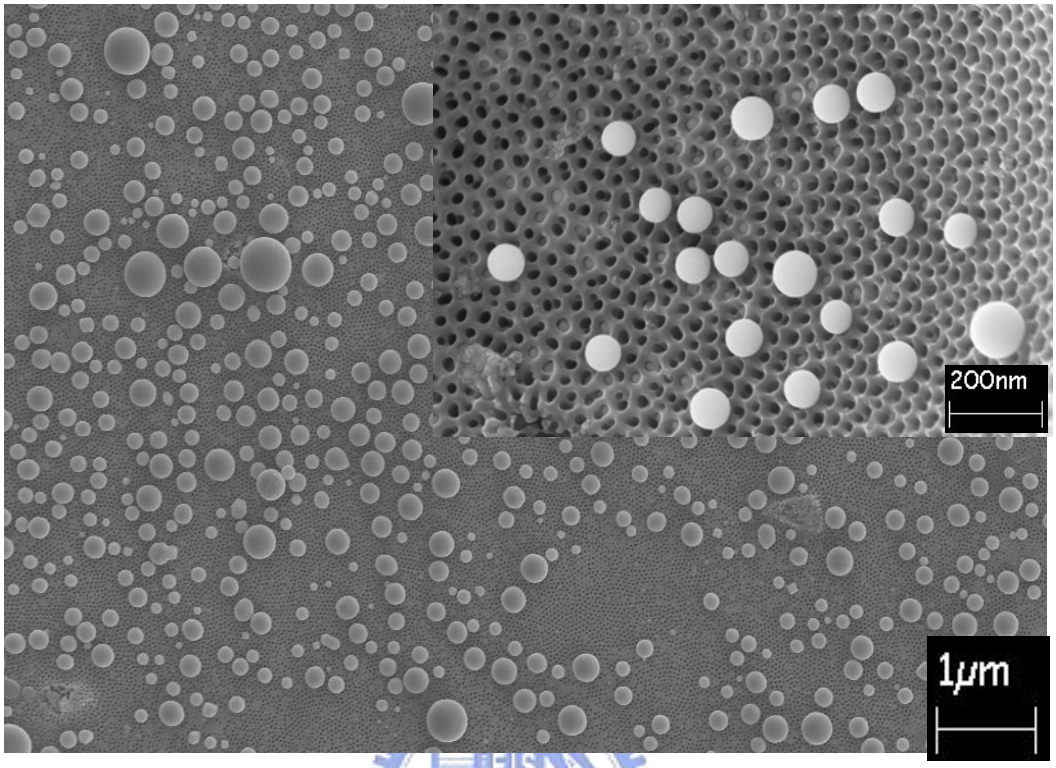


**Fig. 3.12** The Sn nanospheres formed by thermo expansion process.

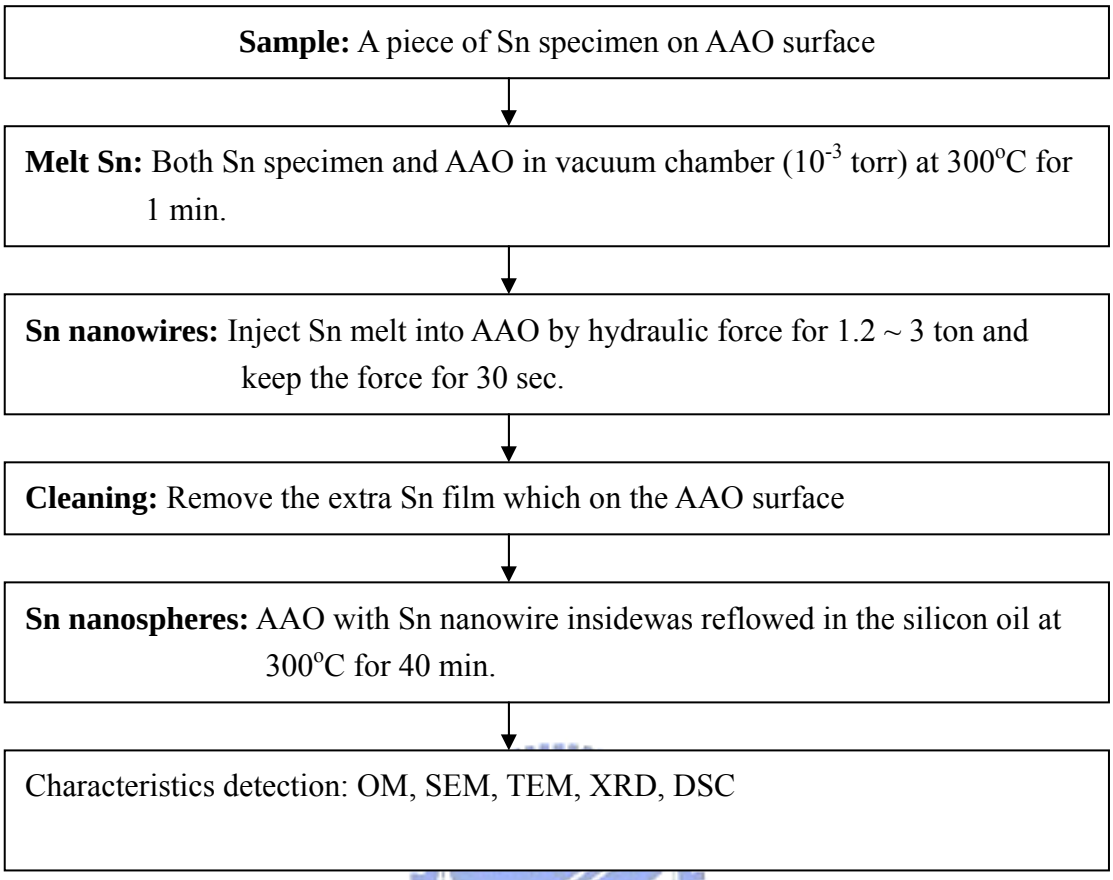


**Fig. 3.13** The flow sheet of Sn nanospheres fabricated by oil reflowing.

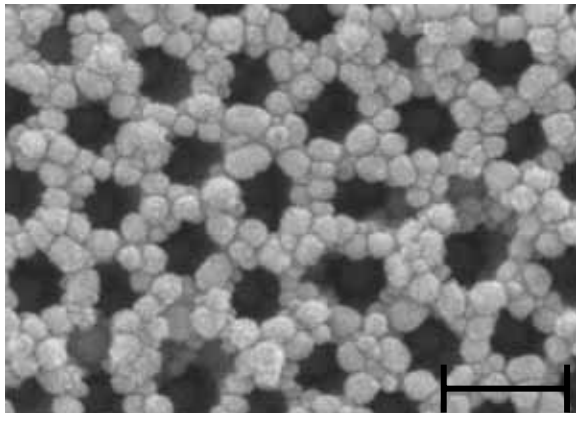


**Fig. 3.14** Sn spheres forming on the AAO surface by E-beam deposition process.

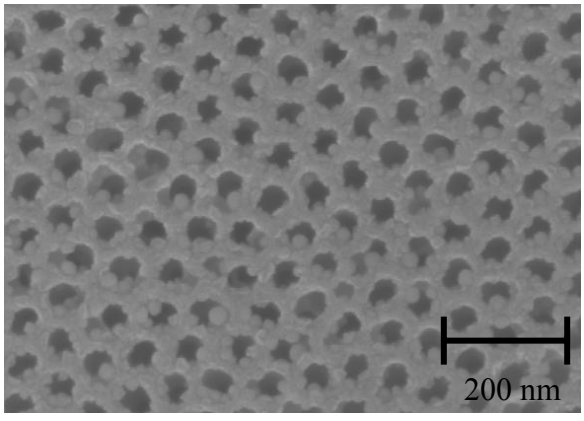


**Fig. 3.15** The SEM image of nanospheres on AAO by thermal immersion process.

# Chapter 4 Results and Discussions

## 4.1 Electrochemistry of aluminum

### 4.1.1 Electropolishg of Al

Because aluminum is a soft and ductile material, it difficult to obtain an optical lever surface by mechanical and chemical polishing. The surface always retains scrapes after mechanical polishing even by # 4000 SiC papers and 0.05 μm $Al_2O_3$ powder, showed as Fig. 4.1 (a). The scrapes can be removed by chemical polishing; however, there still remained some pitting and reaction film on the Al surface by chemical ions attacking, showed as Fig. 4.1 (b). The problems of mechanical and chemical polishing on the soft and ductile materials can be solved by

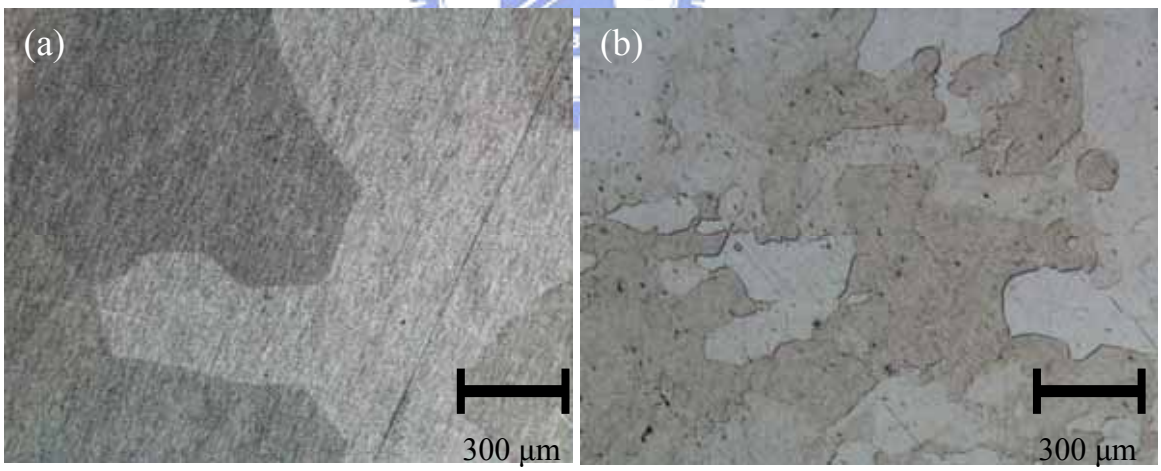


**Fig. 4.1** The OM images of mechanical polishing (a), and chemical polishing on pure Al (b).

electropolishing (EP).

Figure 4.2 showed the pure Al specimen without annealed before EP, the EP surface presents the microstructure in disordered sizes and shapes.

However, A clean and plane surface of pure Al after annealing at 550 $^{o}$C for 1 hr then EP was showed as Fig. 4.3. Therefore, the surface energy of the substrate must be reduced by annealing before EP. The quality of EP surface is also influenced by plastic deformation, applied voltage, and solution agitating. Figure 4.4 (a) showed the plastic deformation caused when the substrate is pre-polished by $Al_2O_3$ powder. Figure 4.4 (b) showed pitting by high voltage, and Fig. 4.4. (c) showed waviness when without stirring in the electrolyte.

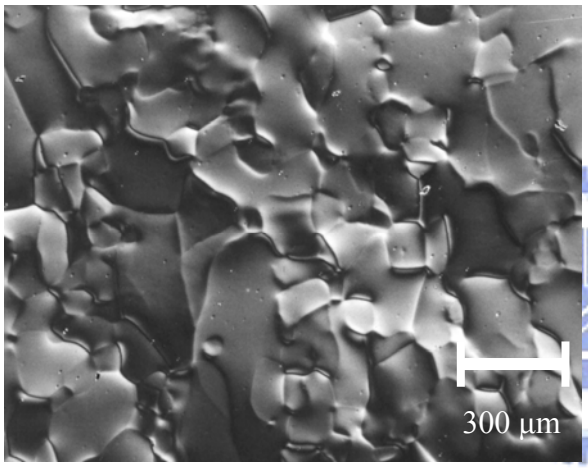


**Fig. 4.2** The OM images of EP Al surface without annealing before.

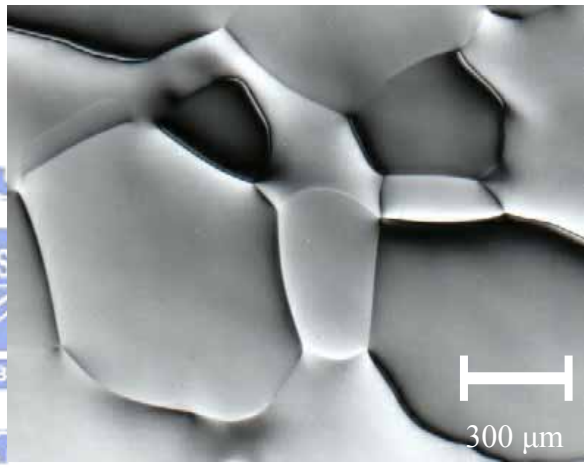


**Fig. 4.3** The OM images of Al surface after annealing and EP.

The EP voltage and EP time are the important conditions in the EP process. Two conditions can be observed by voltage-current density (V - A/cm$^2$) and time- current density (sec - A/cm$^2$) curves. Figure 4.5 and Fig. 4.6 showed those two curves when pure Al is EP in $HClO_4$ base electrolyte. In the curves the plateau area is suitable for the EP. Therefore, the EP voltage and EP time can be decided in the range of 35 ~42 V (DC) and 600~700 sec. In the experiment, applied voltage of 40V for 660 sec was

used for Al EP. Figure 4.7 showed the EP progress on the insufficient EP time from 10 to 620 sec. However, the EP surface will damage by excessive EP time, Fig. 4.8 showed the rough surface when the EP reached to 1000 ~ 1400 sec.

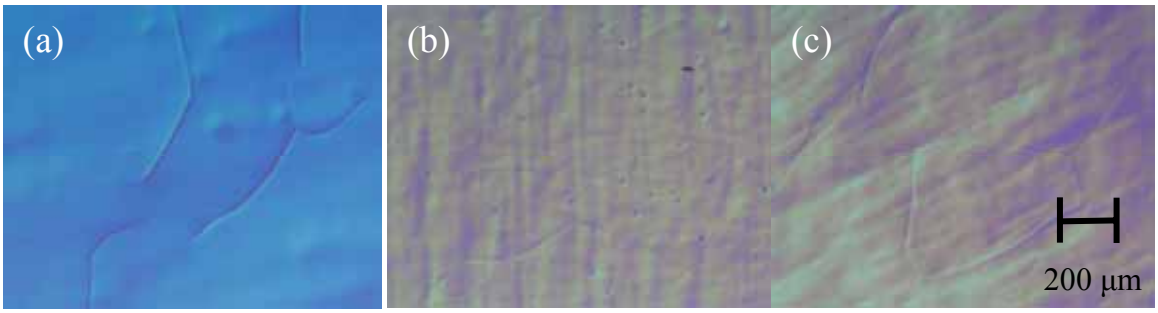


**Fig. 4.4** The OM images of the defects on Al surface after EP; plastic deformation when pre-polishing by $Al_2O_3$ powder (a), pitting by high voltage (b), and waviness by without stirring.

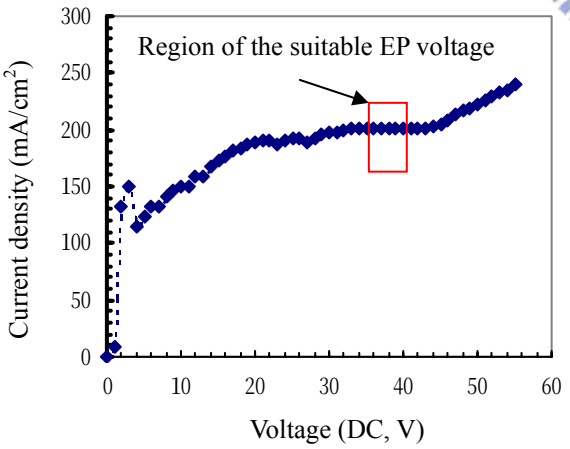


**Fig. 4.5** The curve of voltage vs. current density of Al EP.

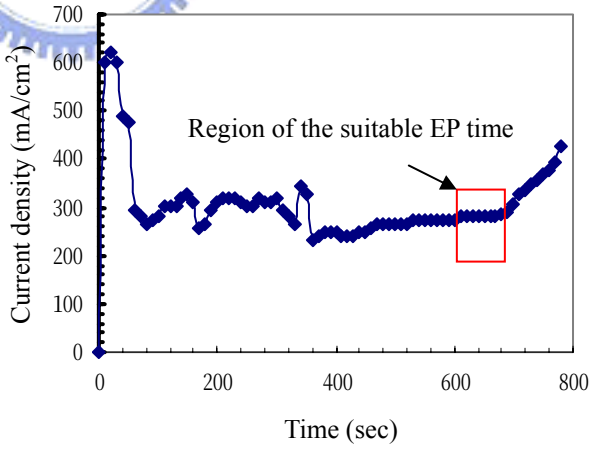


**Fig. 4.6** The curve of time vs. current density of Al EP.

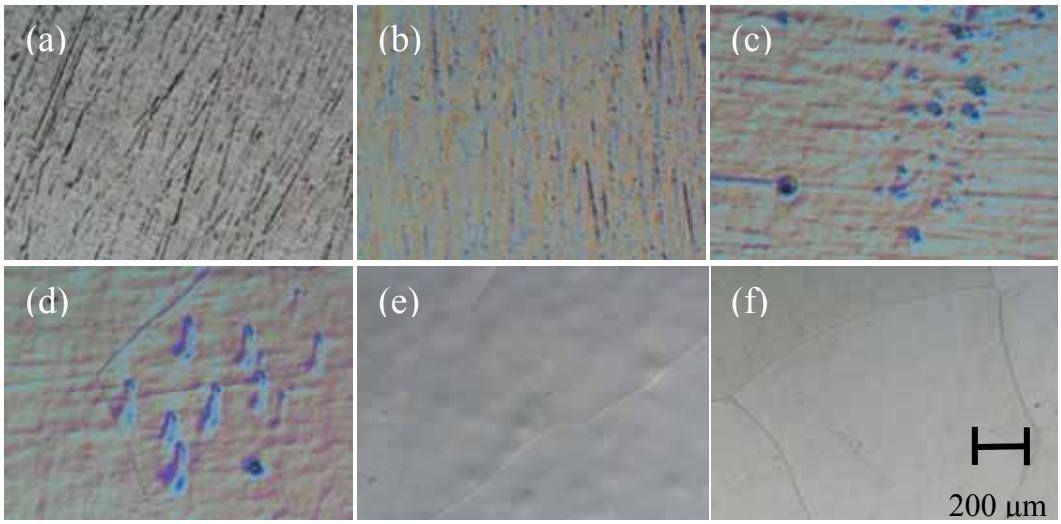


**Fig. 4.7** The OM images of insufficient EP time; 5 sec (a), 10 sec (b), 35 sec (c), 50 sec (d), 500 sec (e), 620 sec (f).

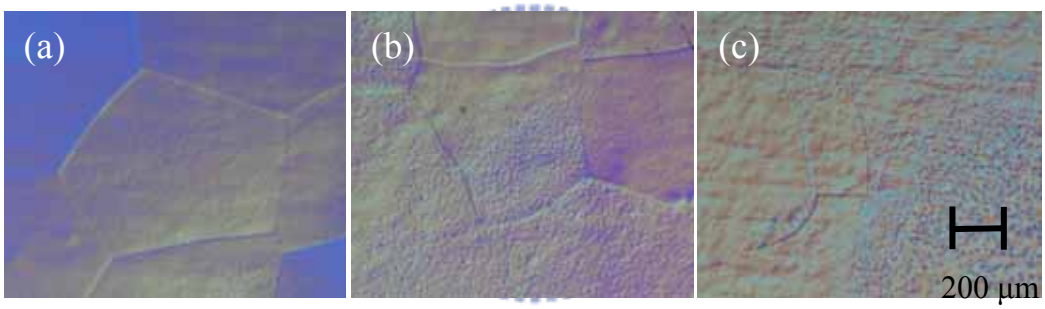


**Fig. 4.8** The OM images of excessive EP time; 1000 sec (a), 1200 sec (b), 1400 sec (c).

### 4.1.2 Pourbaix diagram of Al

A metal in water ($H_2O$) solution may react to 3 types of general reactions: (1) oxidation to aqueous cations, (2) oxidation to aqueous anions, and (3) oxidation to Hydroxide or oxide. The reactions are expressed as reactions. (1), (2), and (3), where $M$ is metals, $M^{+n}$ is metals ion, $n$ is valence electrons, $e^-$ is electron, $H_2O$ is water, $MO$ is oxide, $H^+$ is hydrogen ion, and $M(OH)$ is hydrate.

$$M \rightarrow M^{+n} + ne^- \quad \text{.....(1)}$$

$$M + nH_2O \rightarrow (MO_n)^{-n} + 2nH^+ + ne^- \quad \text{.....(2)}$$

$$M + nH_2O \rightarrow M(OH)_n + nH^+ + ne^- \quad \text{.....(3)}$$

When aluminum is immersed in aqueous solution, regions of corrosion ($Al^{+3}$, $AlO_2^-$), passivation ($Al_2O_3$), and immunity (Al) are delineated by various local standard hydrogen voltages (SHE) and pH values; additionally, the axis of the voltage vs. pH plot, or the Pourbaix diagram can be constructed from Nernst' s equation and the standard electrode potential. In plotting the diagram, the cations $Al(OH)^{++}$, $Al(OH)_2^+$ and $AlO^+$ , which all seem to relate only to chloride complexes, are neglected. Possible reactions that may occur during the immersion of aluminum in aqueous solution include:

$$Al_{(s)} \rightarrow Al^{+3} + 3e^- \quad \text{.....(4)}$$

$$2Al_{(s)} + 3H_2O_{(l)} \rightarrow Al_2O_{3(s)} + 6H^+ + 6e^- \quad \text{.....(5)}$$

$$2Al^{+3} + 3H_2O_{(l)} \rightarrow Al_2O_{3(s)} + 6H^+ \quad \text{.....(6)}$$

$$Al_{(s)} + 2H_2O_{(l)} \rightarrow AlO_2^- + 4H^+ + 3e^- \quad \text{.....(7)}$$

$$Al_2O_3 + H_2O \rightarrow 2AlO_2^- + 2H^+ \quad \text{.....(8)}$$

**Table 4.1** The chemical reactions and Nernst's law when aluminum is immersed in aqueous solution.

| **No.** | **Reactions** | $E^{Mix}$ , $pH$ | **Line types** |
|---|---|---|---|
| 1 | $Al \rightarrow Al^{+3} + 3e^-$ | $E^{Mix} = -1.66 + \frac{RT}{3F} \times \ln[Al^{+3}]$ | Straight horizontal |
| 2 | $2Al + 3H_2O \rightarrow Al_2O_3 + 6H^+ + 6e^-$ | $E^{Mix} = -1.55 + \frac{RT}{6F} \times \ln[H^+]^6$ | Oblique |
| 3 | $2Al^{+3} + 3H_2O \rightarrow Al_2O_3 + 6H^+$ | $\log K = 6\log[H^+] - 2\log[Al^{+3}]$ | Straight Vertical |
| 4 | $Al + 2H_2O \rightarrow AlO_2^- + 4H^+ + 3e^-$ | $E^{Mix} = -1.382 + \frac{RT}{3F} \times \ln([H^+]^4 \cdot [AlO_2^-])$ | Oblique |
| 5 | $Al_2O_3 + H_2O \rightarrow 2AlO_2^- + 2H^+$ | $\log K = 2\log[H^+] + \log[AlO_2^-]$ | Straight Vertical |

The Nernst's law as Equ. 9 which can be used for Pourbaix drawing, where $\Delta E$ is the over-potential; $(\Delta E_2^o - \Delta E_1^o)$ is the standard electrode potential, R is the gas constant; n is the number of electrons that participate in either half-cell reaction, and F is the Faraday constant, 96500 C/mol, which is the magnitude of charge per mole $(6.023 \times 10^{23})$ of electrons.

$$\Delta E = (\Delta E_2^o - \Delta E_1^o) - \frac{RT}{nF} \ln \frac{[M_1^{n+}]}{[M_2^{n+}]} \quad \text{.....(9)}$$

Table 4.1 lists the Nernst's law used in reactions 4, 5, 6, 7, and 8. Additioaly, the concentration of $Al^{+3}, AlO_2^-$ in reactions 4, 5, 6, 7, and 8 are assumed to dilute with ion concentration of $10^{-6}$. The Tab. 4.1 can be expressed as Tab. 4.2.

**Table 4.2** The Nernst's reactions of Al in aqueous solution when $Al^{+3}, AlO_2^-$ ions concentration are $10^{-6}$.

| No. | Reactions | $E^{Mix}$ , $pH$ |
|---|---|---|
| 1 | $Al \rightarrow Al^{+3} + 3e^-$ | $E^{Mix} = -1.66 + 0.0197 \log[Al^{+3}]$ |
| 2 | $2Al + 3H_2O \rightarrow Al_2O_3 + 6H^+ + 6e^-$ | $E^{Mix} = -1.55 + 0.059 \log[H^+]$ |
| 3 | $2Al^{+3} + 3H_2O \rightarrow Al_2O_3 + 6H^+$ | $\log[Al^{+3}] = 7.98 - 3pH$ |
| 4 | $Al + 2H_2O \rightarrow AlO_2^- + 4H^+ + 3e^-$ | $E^{Mix} = -1.382 + 0.0781 \log[H^+] + 0.0197 \log[AlO_2^-]$ |
| 5 | $Al_2O_3 + H_2O \rightarrow 2AlO_2^- + 2H^+$ | $\log[AlO_2^-] = -12.32 + pH$ |

The Pourbaix diagram of aluminum in aqueous solution can be constructed from the data in Tab. 4.2, as shown in Fig. 4.9. The diagram includes regions that correspond to $Al^{+3}$, $Al_2O_3$ and $AlO_2^-$. During anodization, the applied voltage and the pH of the solution in the ions regions of $Al^{+3}$ or $AlO_2^-$ can be controlled, according to the diagram. However, in the $AlO_2^-$ regions (alkaline), the rate of dissolution of alumina exceeds its growth rate, so the oxide is difficult to form. Hence, the anodizing conditions of must always be controlled in the $Al^{+3}$ region (pH<4).

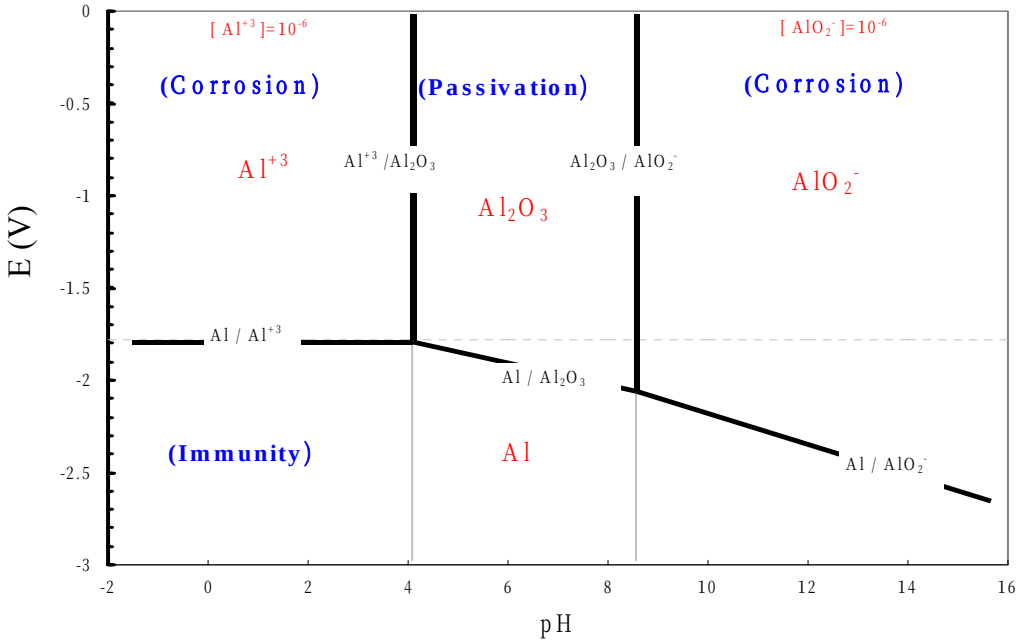


**Fig. 4.9** The Pourbaix diagram of Al in electrolytes.

### 4.1.3 Anodization of Al

When aluminum is immersed in the 10% $H_2SO_4$ or 3% $H_3PO_4$ electrolyte, $H_2SO_4$ is ionized to $SO_4^{2-}$ and $2H^+$ (reaction 10), or $H_3PO_4$ is ionized to $PO_4^{3-}$ and $3H^+$ (reaction 11), causing the electrolyte to become increasingly acidic. Based on the Al Pourbaix diagram, applying a voltage to the aluminum ionizes Al to $Al^{+3}$ (reaction 12), establishing the basic conditions ($Al^{+3}$, acid region) for anodizing aluminum. In aqueous solution, water ionizes to $H^+$, and $OH^-$, so $Al^{+3}$ can associate with $OH^-$ to form alumina. A pair of $H^+$ ions combined to form $H_2$, escaping from the bottom of the alumina, according to reaction 10. During anodization, hydrogen gas escapes through the alumina tube, and $Al^{+3}$ can be extracted from the bottom of the alumina. Therefore, $Al^{+3}$ associates with $OH^-$ (reaction 13) or $O^{2-}$ (reaction 14) to form a precipitate of $Al_2O_3$.

$$H_2SO_{4(l)} \rightarrow SO_4^{2-} + 2H^+ \quad \text{.....(10)}$$

$$H_3PO_{4(l)} \rightarrow PO_4^{3-} + 3H^+ \quad \text{.....(11)}$$

$$Al_{(s)} \rightarrow Al^{+3} + 3e^- \quad \text{.....(12)}$$

$$2Al^{+3} + 3OH^- \rightarrow Al_2O_{3(s)} + 1.5H_{2(g)} \quad \text{.....(13)}$$

$$2Al^{+3} + 3O^{2-} \rightarrow Al_2O_3 \quad \text{.....(14)}$$

## 4.2 Comparison of AAO forming by two-step and one-step anodization

### 4.2.1 two-step anodization

The arrayed nano-pores cannot be easily obtained unless highly pure (above 99.999%) aluminum foils are used. A single crystal or high purity (99.999%) aluminum substrate can be used to fabricate an ordered array of nanochannels on AAO. The typical of 15 nm and 60 nm pore diameter AAO were fabricated using two-step anodization in the 10% $H_2SO_4$ and 3% $C_2H_2O_4$ solution [75-78]. In the Fig. 4.10, The SEM images show 15 nm pore diameter of AAO fabricated by 10% $H_2SO_4$ and applied at 18V. Then the pores were expanded by 5% $H_3PO_4$ solution with various pores widening time. Before pore widening AAO with random pores and various pore size (Fig. 4.10 (a)). But, after pore widening the pore size get to uniform (Fig. 4.10 (b) - (f)). Then after long time pore widening such as 30 to 40 min, it would over pore widening on the AAO and pores broken (Fig. 4.10 (g) -(i)). As well as, for the 60 nm pore diameter of AAO fabricated by 3% $H_2SO_4$ and applied at 40V. The small and various pore size on the AAO before pore widening (Fig. 4.11 (a)). Then the ordering pores were getting formed after pore widening in the 25 min (Fig. 4.11 (b) - (f)). But, over pore widening (Fig. 4.11 (g) - (i)) were happened when pore widening was over than 30 min. However, the use of an expensive high purity aluminum substrate will restrict AAO in the future. Therefore, the use of common or commercial aluminum for AAO is helpful in nano-technological development. On the nanometer scale, the thickness of a film is determined by the rate of growth of the film and the rate of its

dissolution. Film growth is favored under conditions of a high anodizing current density and a slightly acidic concentration of electrolytes at low temperatures. Opposite conditions favor the dissolution of the film. In Fig. 4.12, the SEM images

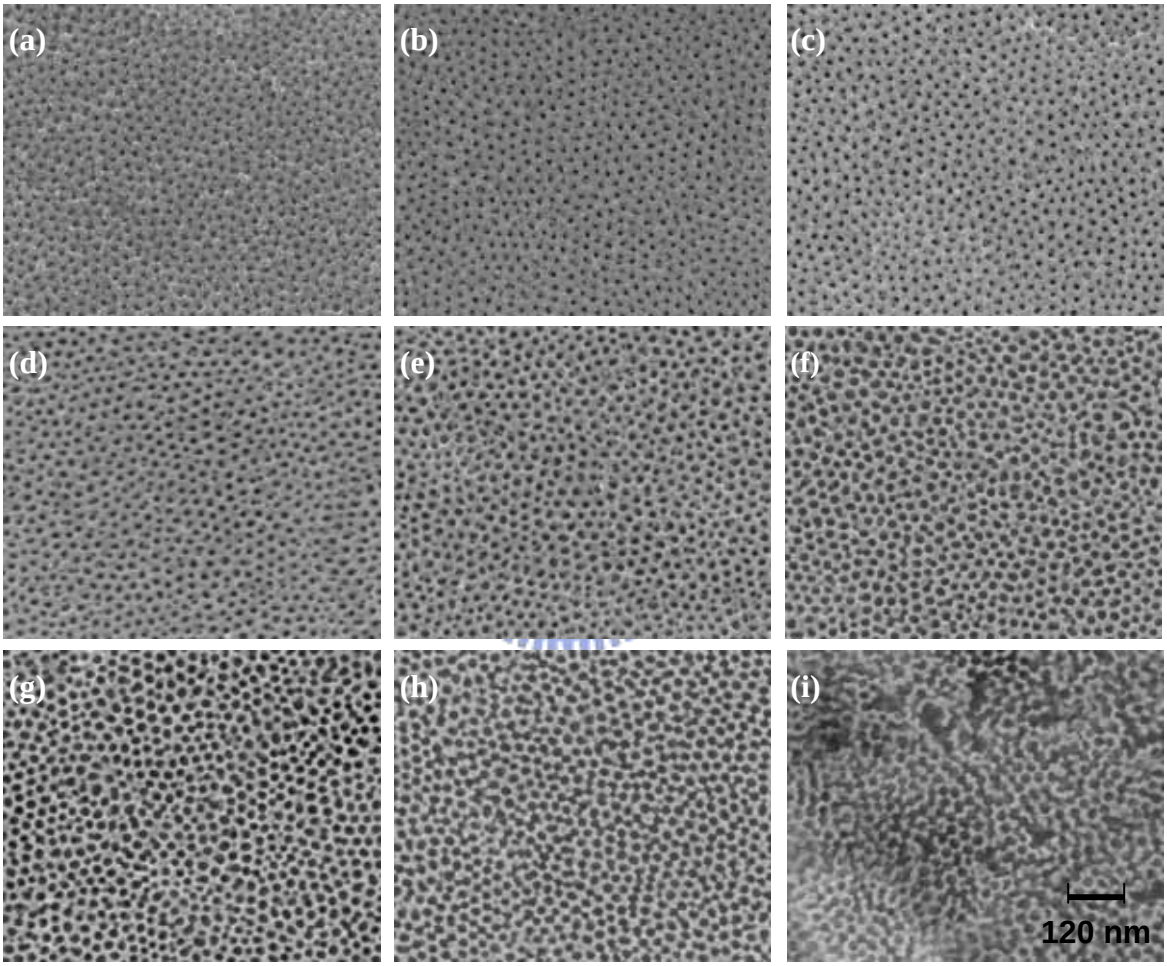


**Fig. 4.10** Two steps anodization to fabricate AAO using high purity (99.999%) Al foil as substrate in 10% $H_2SO_4$ solution at 18V, then AAO through pore widening using 5 vol. % $H_3PO_4$ solution for 0 min (a), 5 min (b), 10 min (c), 15 min (d), 20 min (e), 25 min (f), 30 min (g), 35 min (h), 40 min (i).

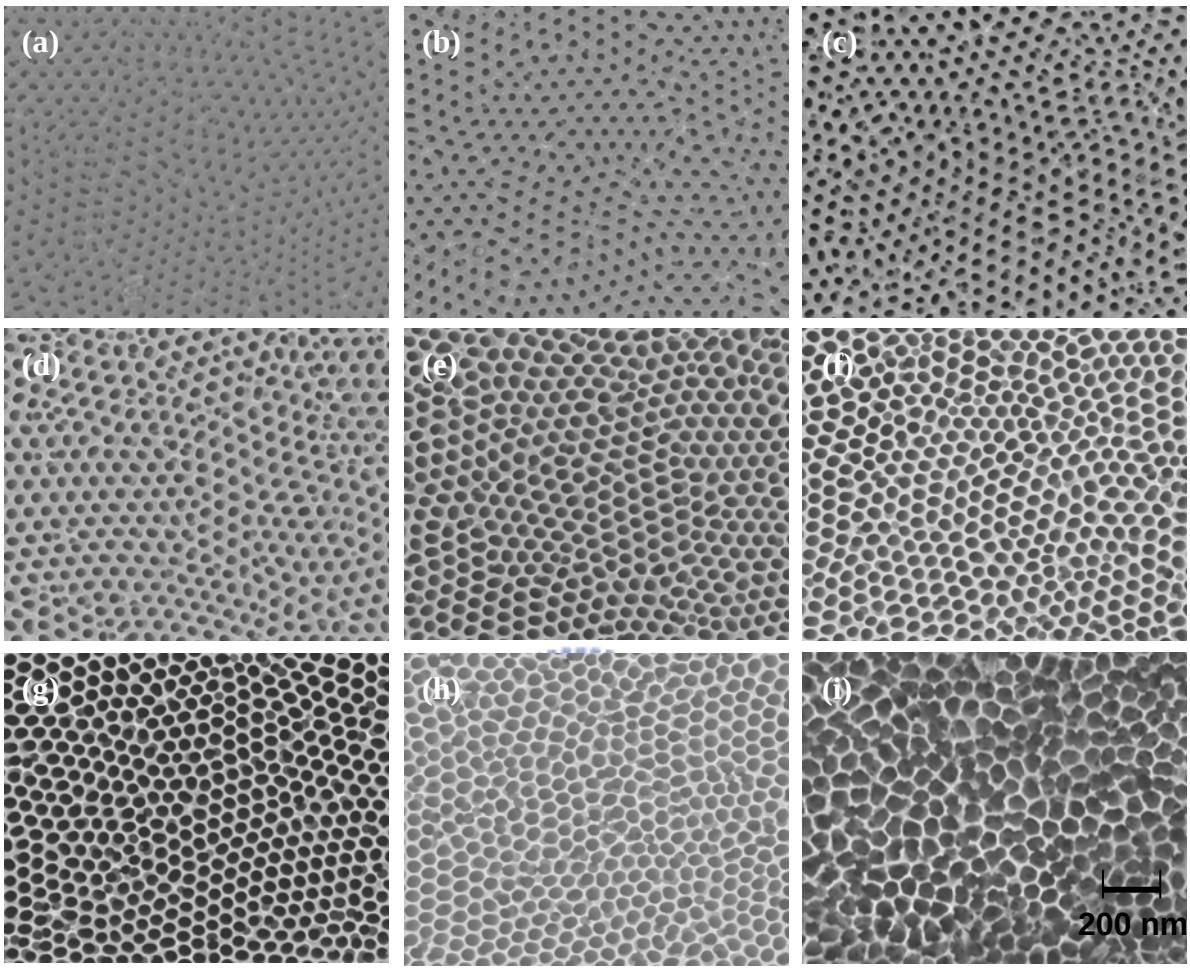


**Fig. 4.11** Two steps anodization to fabricate AAO using high purity (99.999%) Al foil as substrate in 3% $CH_2O_4$ solution at 40V, then AAO through pore widening using 5% $H_3PO_4$ solution for 0 min (a), 5 min (b), 10 min (c), 15 min (d), 20 min (e), 25 min (f), 30 min (g), 35 min (h), 40 min (i).

of a 99.7 % pure aluminum substrate anodized in 3 wt% oxalic acid solution at 40 V for 1 hour is shown. The disordered pores of AAO and the dense barrier layer are shown in Fig. 4.12(a). The nanopores on AAO were disordered with a pore diameter of 15 nm after anodization, as shown in

Fig. 4.12(b), although the pore diameter increased to 60 nm through pore widening for 30 min as shown in Fig. 4.12(c). Additionally, the pore size and the thickness of pore walls were not uniform, and many sub-holes appeared adjacent to the main holes. Since 99.7% pure aluminum contains 0.3% impurity, impurities including Fe, Si, and P are easy to dissolve in the electrolyte during the anodization of Al. Therefore, a few sub-holes remain in AAO. Additionally, by increasing the time of pore widening to 50 min, the nano-structure of AAO was destroyed, as shown in Fig. 4.12(d).

AAO bottom view of barrier layer image can be observed when Al substrate was dissolved by etching solution ($CuCl_{2(sat)}$ + 8 vol. % HCl) at 25°C. The morphology of barrier layer is close to hexagonal structure, showed as Fig. 4.13(a). Furthermore, barrier layer can be dissolved or pore widening by etching solution (5 wt. % $H_3PO_4$) at 30°C. Barrier layer was dissolved beginning on the center of hexagonal structure after 30 min etching, showed as Fig. 4.13(b). Then barrier layer be removed fully after 40 min. etching, showed as Fig. 4.13(c). Continues etching AAO, The AAO pore wall become thinner with increases etching time, this step may call pore widening, showed as Fig. 4.13(d) and (e), which etching time is 50 min, and 60 min. Increases etching time to 70 min, each pores connect together, this step may call over etching showed as Fig. 4.13(f).

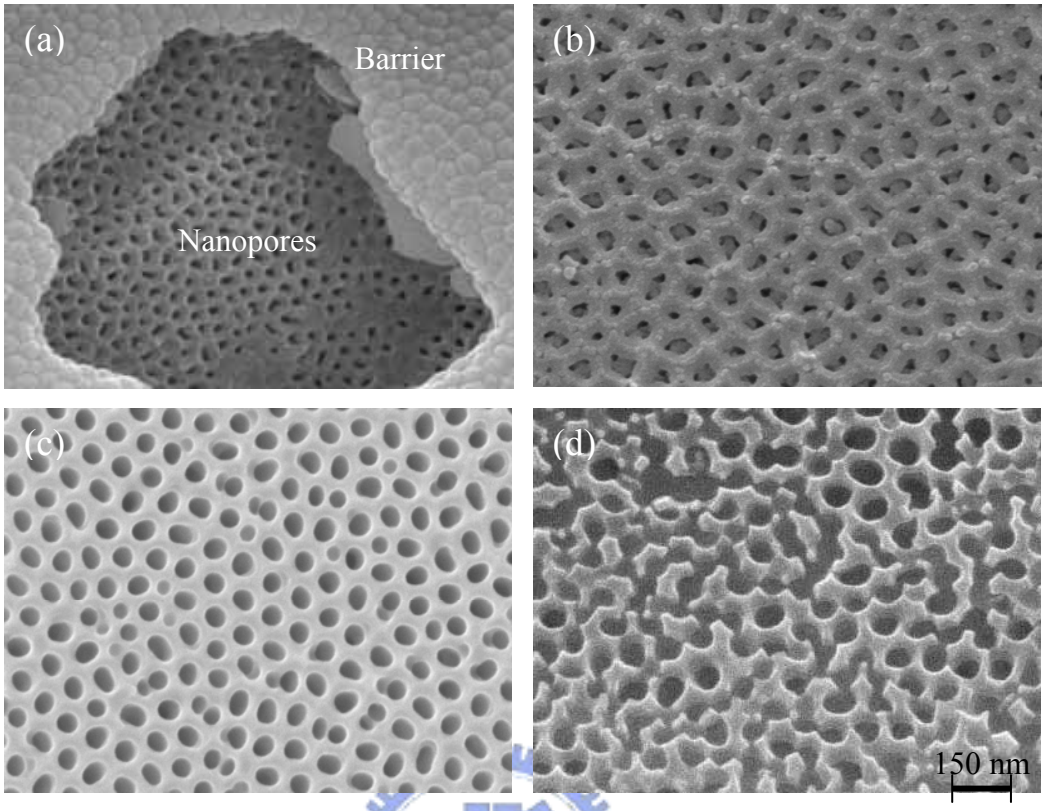


**Fig. 4.12** SEM images of AAO made from aluminum foil (99.7% purity). The anodized alumina layers were prepared by anodization in 3% oxalic acid at 25°C at 40 V. Bottom view of nanopores with barrier layer before pore widening (a). Non-ordered nanopores appear on top view (b). Top view of AAO with subholes after pore widening (c). The pore structure was destroyed easily without heat treatment, even when the pore widening time was only 50 min. (d).

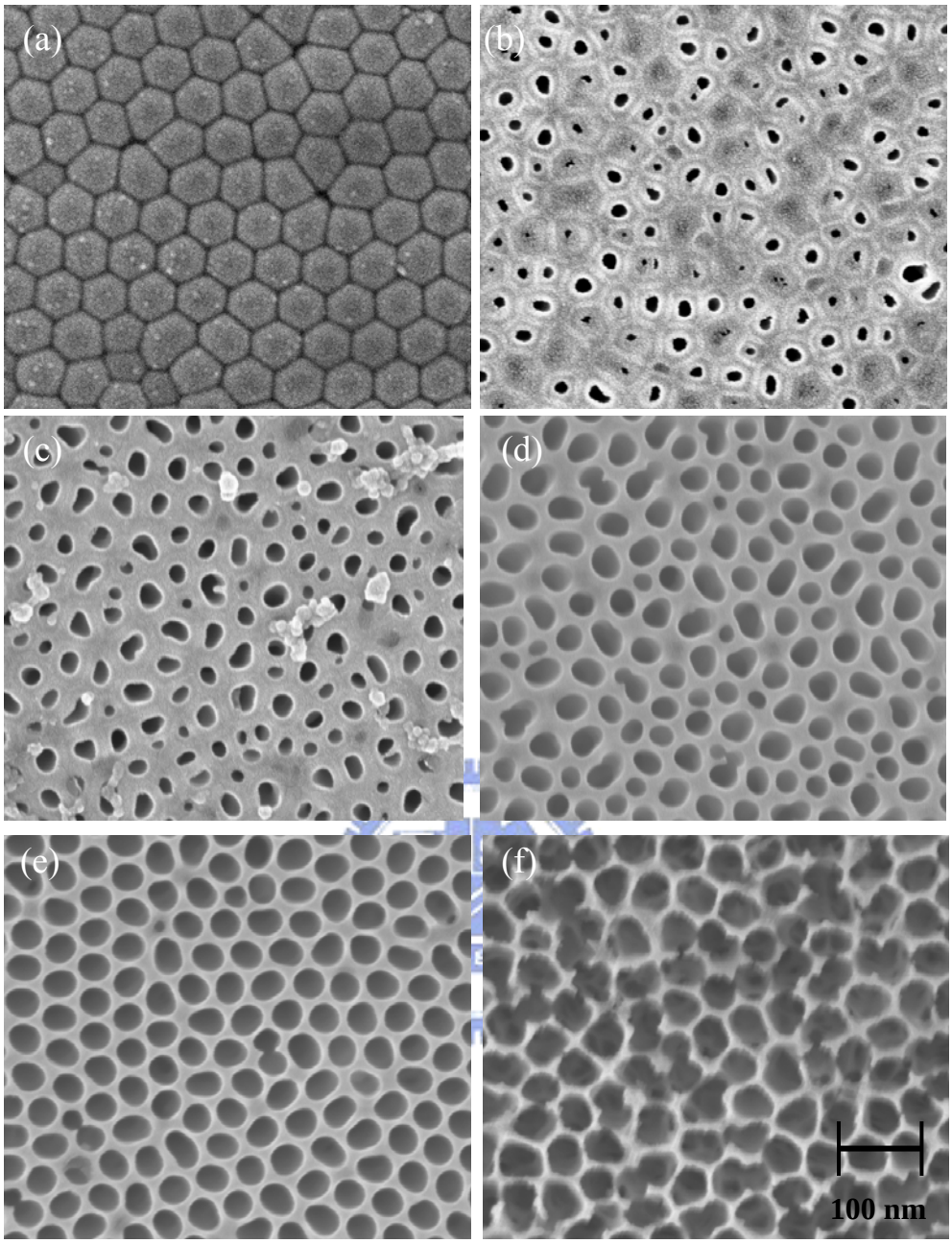


**Fig. 4.13** SEM images of AAO bottom views. Barrier layer image (a), barrier layer was etched by 5 wt. % $H_3PO_4$ solution at 30$^{o}$C for 30 min (b), for 40 min (c), for 50 min (d), for 60 mim (e), and for 70 mim (f).

### 4.2.2 one-step anodization

The anodized oxide film includes two layers; the outer layer is thicker and more porous than the inner layer. The inner layer is also named the barrier, active or dielectric layer and usually represents 0.1 to 2% of the thickness of the entire film [73]. Akahori [85] has demonstrated that the melting point of this inner oxide layer is 1000 $^{o}$C, also the AAO template is stable around 800 $^{o}$C [86], which is lower than that of bulk alumina (2017$^{o}$C for $Al_2O_3$). Because the stable of AAO is approximately 800 $^{o}$C the self-diffusion of AAO occurs in the nanochannel at a temperature up to 600 $^{o}$C. In our experiment, to remove the sub-holes adjacent to the main holes, AAO on an Al substrate was heat treated at 600 $^{o}$C for 4 hr. Consequently, the pore wall distance became uniform, the sub-holes disappeared, and the main holes decreased to approximately 10 nm in diameter owing to the self-diffusion of alumina, as shown in Fig. 4.14(a). When the sub-holes disappeared and the pore walls became thick after the heat treatment, it is suitable for long-lasting pore widening. Therefore, the pores increased to a uniform size during pore widening, as shown in Figs. 4.14(b), (c), and (d). The pore wall decreased to approximately 16 nm when pore widening reached 85 min. Consequently, the array of nanopores with a uniform pore size was 75 nm arranged on the AAO and 9 μm thick on AAO, as shown in Figs. 4.14(e), (f), (g).

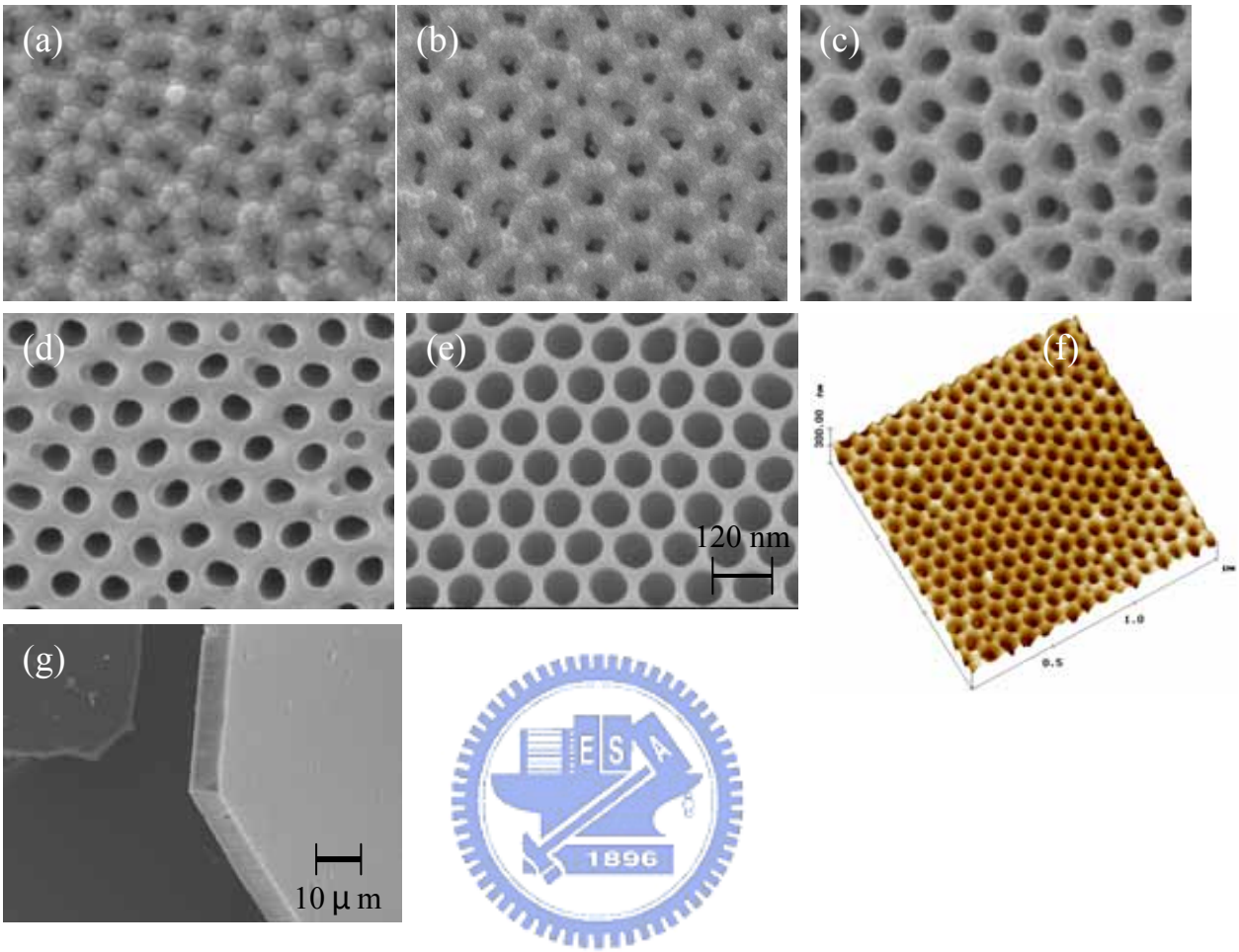


**Fig. 4.14** SEM images of AAO after heat treatment at 600°C; the pores were sintered, then through pore widening, the pores became ordered. (a) The pores in the AAO were sintered and sub-holes was disappeared after 4 hours heat treatment; (b) the pores of AAO expanded after pore widening for 5 min., (c) the pores of AAO expanded and pores became to ordered after pore widening for 50 min., (d) after pore widening for 70 min. (e) the pores of hexagonally packed structure on AAO after pore widening for 85 min. (f) AFM image of close-packed ordered nanostructure after self-repair, (g) AAO with a thickness of 9 um.

More detailed micrographs of AAO after heat treatment are shown in Fig. 4.15. Nano-pores with a high depth-to-width ratio (120/1) are generated over a large area on the order of square millimeters, as shown in Fig 4.15(a). The bottom view of AAO with a barrier layer presented a hexagonal structure, as shown in Fig. 4.15(b), and the cross-sectional view depicted the channels in AAO; each channel grows straight with the barrier layer, as shown in Fig. 4.15(c). Additionally, the hexagonal pattern appeared on the aluminum surface when AAO was removed from the substrate, as shown in Fig. 4.15(d).

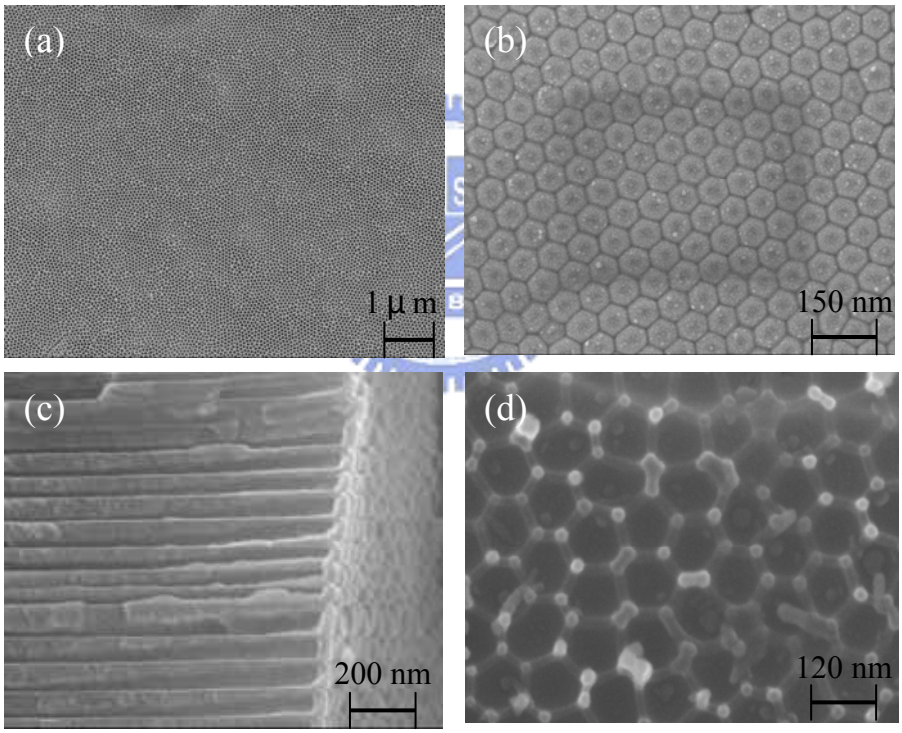


**Fig. 4.15** The top view, cross-section view, and bottom view of AAO, and hexagonal pattern on aluminum surface. (a) Top view of low magnification image of long-range ordered channel array with dimensions of the order of millimeters, (b) bottom view of barrier layer with hexagonally packed structure, (c) cross-sectional view with base of straight tube on the bottom barrier layer, (d) hexagonal pattern on aluminum surface when AAO was removed from substrate.

The property of the hexagonal pattern on the high purity aluminum (99.999%) substrate is always used to grow an array of nanopores, the growth process is called the two-step anodization. However, in our new experiment process, using commercial aluminum (99.7%) as substrate through self-repair, we obtained the same result as that of two-step anodization. the process, which involves long-term heat treatment and pore widening, is called the self-repair for AAO.

### 4.2.3 Self-diffusion of AAO

AAO is a porous structure on the Al substrate. Therefore, Al and an atmosphere of O easily diffuse into AAO from the bottom and top, respectively. The diffusions in AAO can be explained in detail as follows Al and O that diffused into AAO react with $Al_2O_3$. Then the self-diffusion of $Al_2O_3$ decreases the diameter of main pores, and makes the sub-holes disappear from AAO during heat treatment. The schematic diagram of diffusions of Al and O in AAO, and the self-diffusion of $Al_2O_3$ are shown in Fig. 4.16. Diffusion coefficient as a function of temperature is usually expressed by [122]

$$D = D_0 \exp(-Q/RT) \qquad (15)$$

$D_o$ is the diffusion coefficient, and D is the self-diffusion coefficient usually expressed in $cm^2/s$; Q is the activation energy for diffusion; R and T are the gas constant and the absolute temperature in K, respectively. If Q is expressed in cal/mole, R= 1.987 cal/ mole K. For $Al_2O_3$, $D_o$= 430 $cm^2/s$, Q=80 Kcal/mole [123] at 600°C, and D= $4\times10^{-18}$ $cm^2/s$ = $4\times10^{-4}$ $nm^2/s$, or 2500 $s/nm^2$.

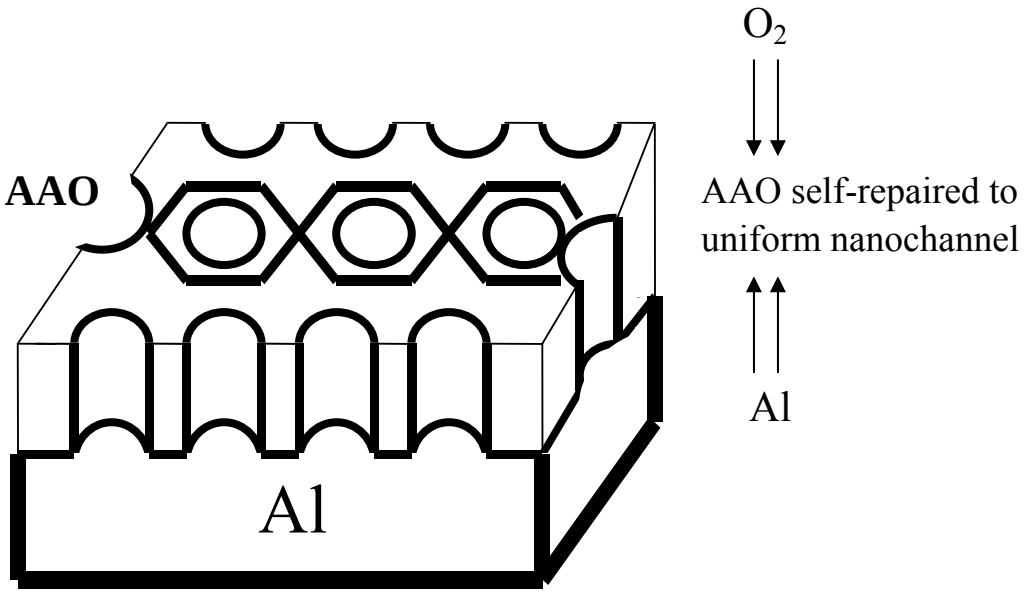


**Fig. 4.16** Schematic diagram showing array nanochannel in AAO is through O and Al diffuse into the AAO.

Figure 4.17 shows the curve of $Al_2O_3$ self-diffusion with diffusion time at 600 °C. The self-diffusion curve increases with heat treatment time at a constant temperature. In Christiant's [124] research, the diffusion coefficient of Al in alumina is $5.8\times10^{-19}$ $cm^2/s$ at 277 °C; also, the diffusion coefficient of O in alumina is $5.7\times10^{5}$ $cm^2/s$ at 600 °C [125]. Therefore the diffusivities of Al and O in $Al_2O_3$ are faster than that of $Al_2O_3$ at 600 °C; moreover, the time of self-repair on AAO depends on the self-diffusion rate of $Al_2O_3$. As shown in Fig. 4.17, when the heat treatment time reached 4 hours, the self-diffusion area of $Al_2O_3$ is 5.76 $nm^2$. In our experiment results, the pore size of AAO before heat-treatment was approximately 15 nm in diameters (Fig. 4.12(b)) then the pore size decreased to 7.5 nm (Fig.

4.14(a)) after heat treatment for 4 hours.

In the heat treatment of AAO, the Al substrate was important for AAO. On the contrary, on AAO without the Al substrate, AAO without a new $Al_2O_3$ formation, the array of nanopores did not appear but pores connected to each other after the heat treatment, as shown in Fig. 4.18.

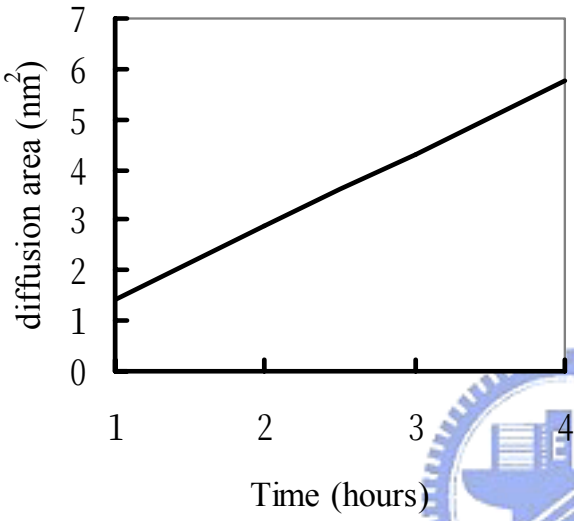


**Fig. 4.17** Self-diffusion distance of $Al_2O_3$ with diffusion time at 600°C.

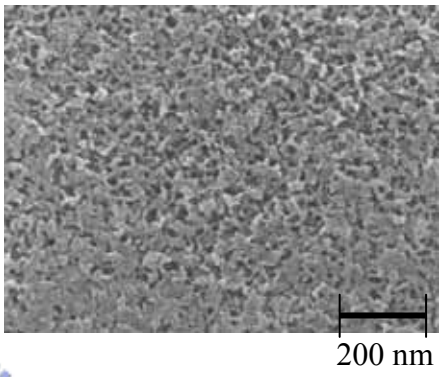


**Fig. 4.18** On AAO without an Al substrate, the AAO structure was destroyed after heat treatment at 600°C for 4 hours.

### 4.2.4 XRD characterization of Al and AAO

In addition, AAO crystallizes from amorphous to face center cubic (FCC) of the γ-phase which may cause defect decrease and pore rearrangement on AAO. Heat treatment and the electrochemical method with a voltage higher than 100 V can cause crystallization on AAO. However, the films formed in acid solutions at less than approximately 100 V are usually considered to be completely amorphous. When the voltage applied is higher than 100 V, crystalline forms of γ-alumina (FCC structure) are considered to occur as local islands within the amorphous film. However, the film cannot be stabilized electrochemically with the nanostructure at a high voltage. Heat treatment is a method that induces AAO crystallization and the stabilization of the nanostructure. Figure 4.19 presents the X-ray diffraction spectrum of AAO before heat treatment. The structure of AAO is amorphous after being anodized (curve (a)) during pore widening using phosphoric acid, the reflection peaks (300), (321), and (054) of that $AlPO_4$ appeared in amorphous AAO (curve (b)). Figure 4.20 presents the reflection peaks (311), (400), (222), and (440) of γ-$Al_2O_3$ that appeared after AAO was annealed at 600°C for 4 hours. Therefore, amorphous AAO is transformed into crystalline γ-$Al_2O_3$ through annealing.

In the schematic diagram shown in Fig. 4.21(a), $Al_2O_3$ is amorphous and the pore morphology is random in AAO after the initial anodization, but AAO crystallizes after long-term heat treatment. The self-diffusion of

$Al_2O_3$ causes pore size or sub-holes decrease on AAO, as shown in Fig. 4.21(b). Figure 4.21(b), shows that the pore wall is getting thicker after heat treatment. Therefore, AAO can be widened for long-term. Hence, an array and a straight tube appear in AAO, as shown in Figs. 4.21(c) -(d).

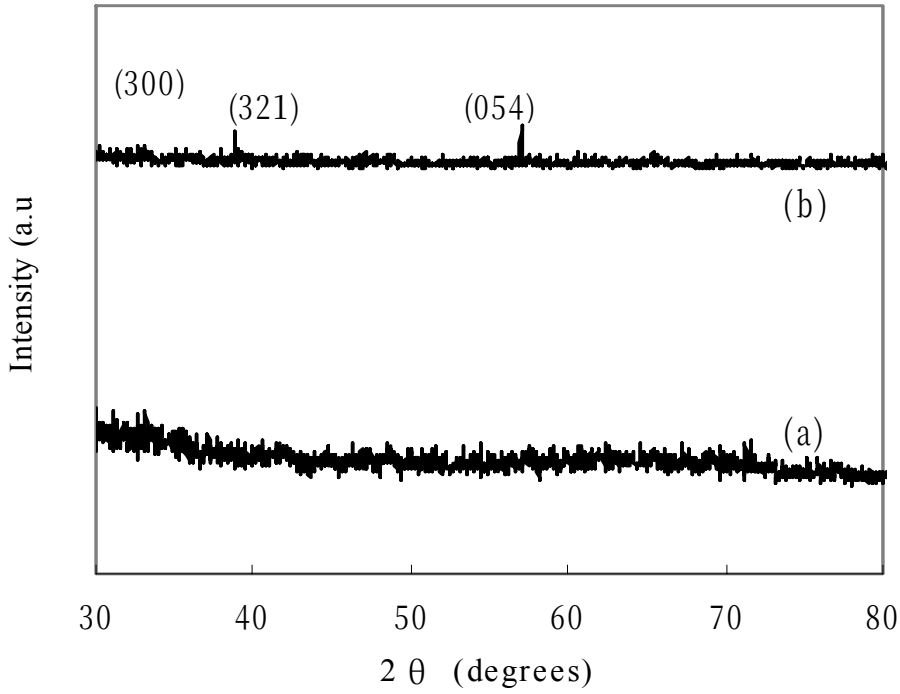


Fig. 4.19 X-ray diffraction spectrum of AAO before annealing: (a) amorphous AAO, (b) $AlPO_4$ peaks in the amorphous AAO, after pore widening.

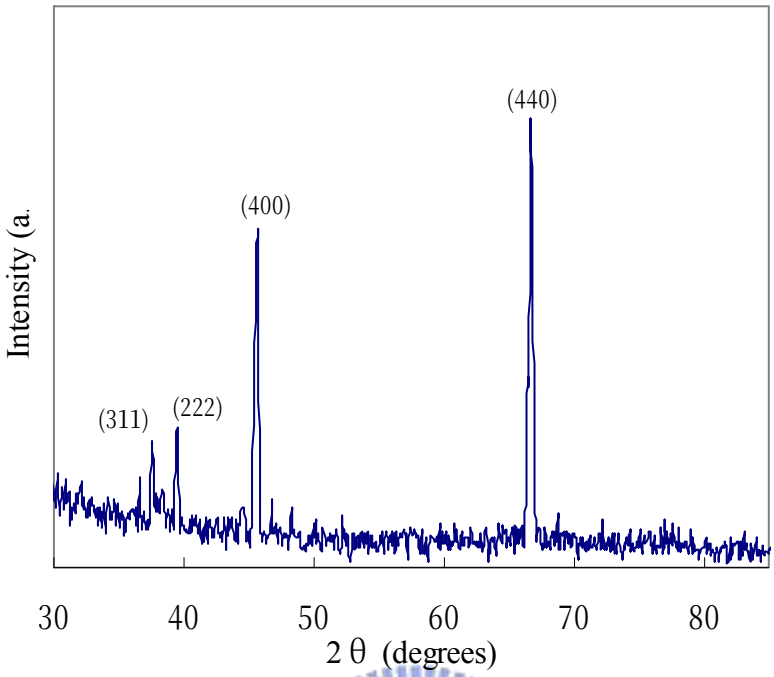


**Fig. 4.20** X-ray diffraction spectrum of AAO crystallized to γ -phase of $Al_2O_3$ after annealing.

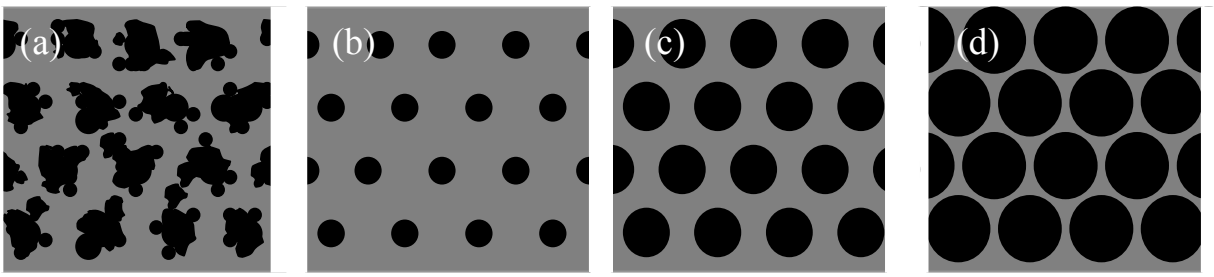


**Fig. 4.21** Schematic diagram of self-repair. (a) The holes in AAO were random when Al with a purity of 99.7% was used after anodization, (b) the pores decrease in size towards the center of pore after heat treatment, (c) the pores were expanded by upon pore widening, (d) after long-term pore widening, uniform-sized close-packed ordered nanopore on AAO.

## 4.3 AAO growth on the silicon wafer and glass substrate

Most electronic and optolelctronic devices are based on high-quality semiconductors process. It will be highly if the self-assembly nanofabrication techniques can be combined with traditional microfabrication technologies in the pursuit of next generation high performance nanoscale devices. Based on the technique of AAO forming on Al foil, AAO on Si wafer and glass substrate can be achieved in our experiment. However, the process unsuitable includes the lasting heat treatment step because Si would solve in Al film. The maximum solubility of Si in Al is 1.5 at% at the eutectic temperature (577$^{o}$C), and it decreases to 0.05 at% at 300 $^{o}$C, the Al-Si binary phase diagram showed as Fig. 4.22. When the second phase of Si solved in Al, it will make sub-holds in AAO. As well as, the coefficient of linear thermal expansion between Si (22 × $10^{-6}$/$^{o}$K) and ceramic AAO (very low) is very different at high temperature it makes AAO falling off Si wafer easily.

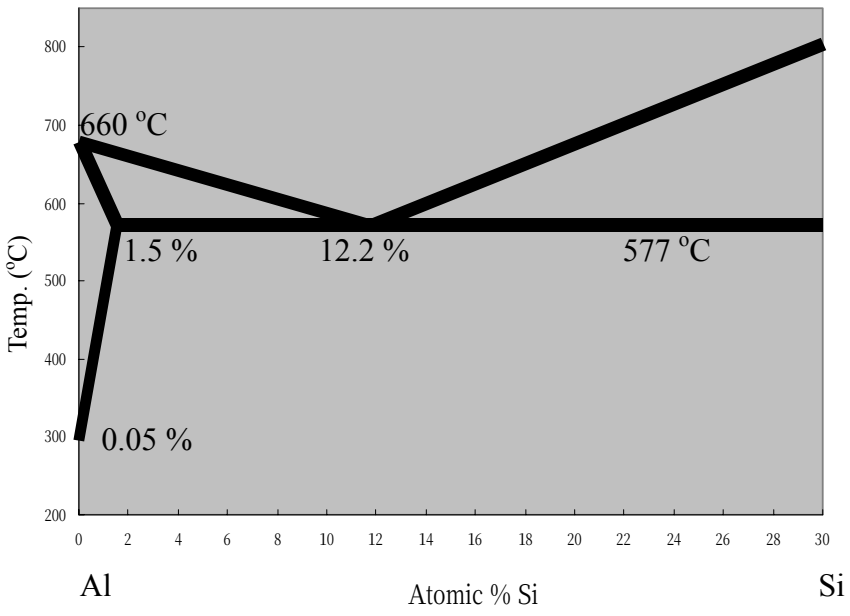


**Fig. 4.22** Al-Si binary phase diagram

For the above reasons, the one-step anodization was replaced by the two-steps anodization when made AAO on Si and glass substrate. Figure 4.23 showed the macro OM image of AAO on the 6 inch Si wafer (a), and 4 inch glass substrate (b). Because the interface between AAO and Si/glass the AAO morphology is poorer then AAO on the foil Al substrate. The SEM images of AAO on the 6 inch Si wafer, and 4 inch glass substrate, showed as Fig. 4.24(a) and (b). The AAO bottom of barrier layer on the Si, glass/AAO interface always decreases the electron conductivity transparency. For this reason, the barrier was removed by the process of applied 10 V pulse voltage (30 Hz) on AAO for 3 seconds using 5 % $H_3PO_4$ as electrolyte. Figure 4.25 compared the cross-section SEM images of AAO on Si wafer with barrier layer (a) and without barrier layer (b). Figure 4.26 showed the transparency is about 56 % when 1 μm thickness of AAO without barrier layer on the glass substrate.

The thickness of barrier layer is mainly determined by the anodizing voltage although there is a slight deviation depending on the anodization electrolyte and temperature. Early experimental studies on the morphology and mechanism of pore formation on aluminum films showed that the barrier layer thickness is proportional to the anodization voltage [66]. Accordingly, the thicknesses of the barrier layer of the templates used in this study are estimated to be ~18 nm and ~40 nm [80] for AAO (ϕ15 nm) and AAO (ϕ60 nm) templates respectively and hence the significant difference in etching time. A thin film of barrier layer has similar chemical

composition with AAO. Also, the thickness of barrier layer is similar to AAO pore wall. The isotropic etching would be happen during wet etching. It is difficult to keep AAO well but remove or dissolve barrier layer by just chemical etching method. However, when applied pulse voltage to the specimen the barrier layer is closer to electrode (anodic) than AAO pore wall. Therefore, the short time electrochemical etching by pulse voltage method can remove barrier layer but retains AAO.

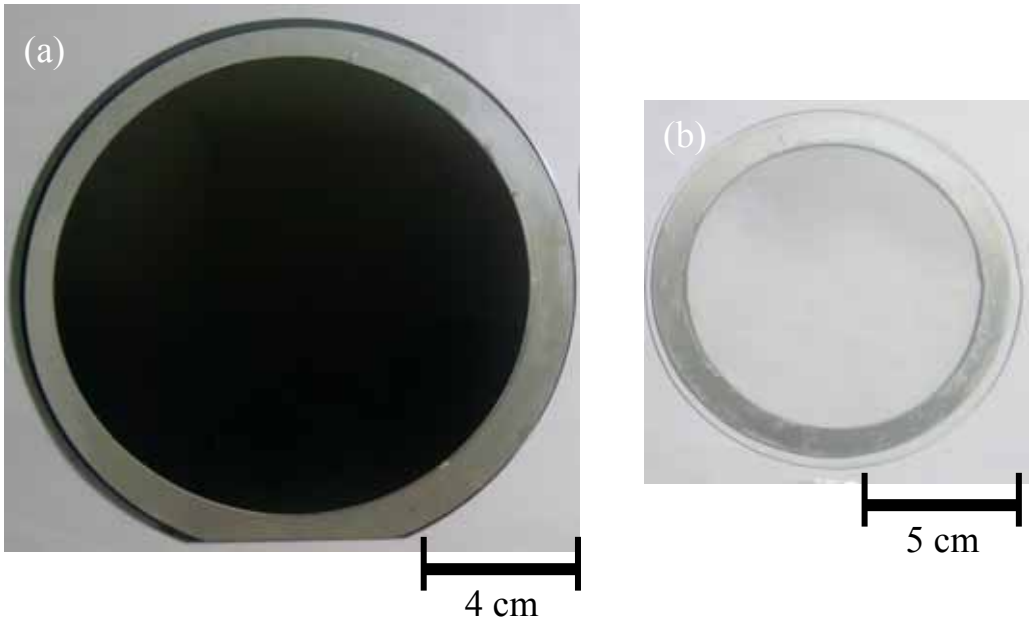


**Fig. 4.23** Marco OM image of AAO on the 6 inch Si wafer (a), and 4 inch glass substrate (b).

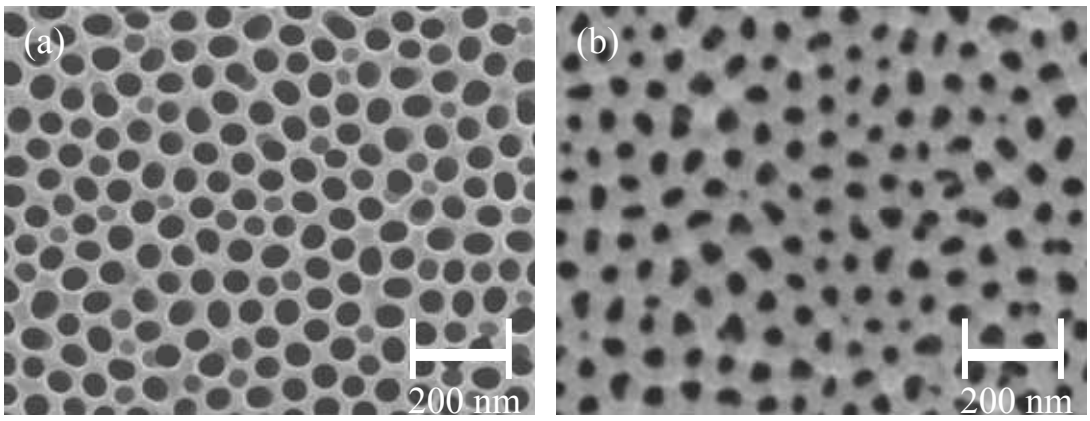


**Fig. 4.24** SEM images of AAO on the 6 inch Si wafer (a), and 4 inch glass substrate (b).

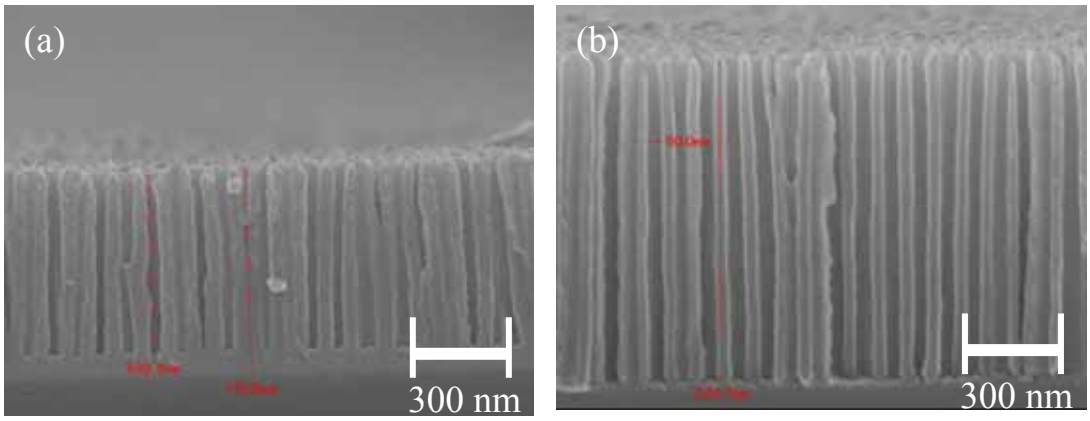


**Fig. 4.25** the cross-section SEM images of AAO on Si wafer with barrier layer (a), and without barrier (b).

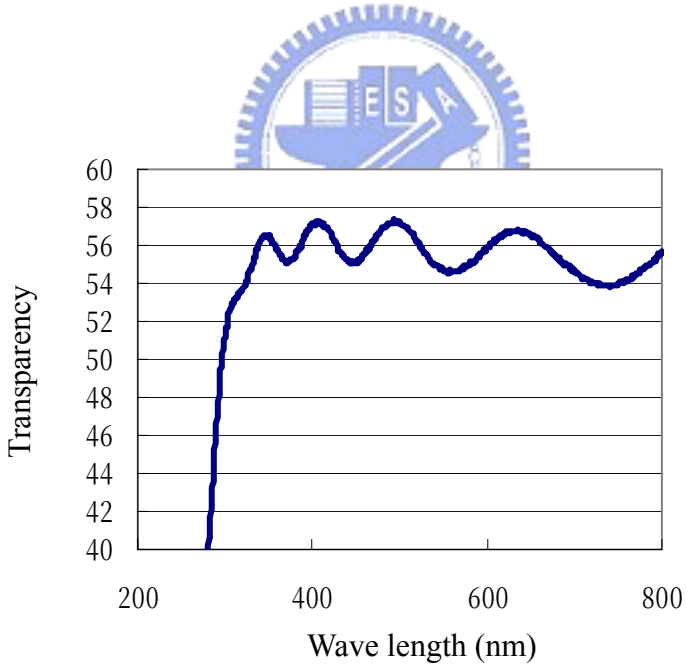


**Fig. 4.26** The transparency of 1 μm thickness of AAO on the glass substrate.

### 4.4 Defects on the AAO

The breakdown of passive/oxide film means a spontaneous local increase of conductivity. Amount of large electrons or aggressive ions can run though the film. Since AAO process is sensitive to the operation conditions, defects would appear on AAO when an unsuitable condition was used. The conditions include electrolyte temperature, surrounding temperature while AAO process is finished, applied voltage, electrolyte composition, chemical etching, and stable current density. The AAO electrolyte is always keeps in the low or room temperature when doing the process. It is always exothermic ($\Delta H < 0$) reaction when metals or components ionize. In the experiment, the metals or components ionization may include of Eqns. 16~20, there are all endothermic reaction [126], where $\Delta H_f^0$ is standard enthalpy.

$$H_2SO_4 \rightarrow 2H^+ + SO_4^{-2},\ \Delta H_f^0 = -909.3\ \text{kJ} \quad \text{.....(16)}$$

$$H_3PO_4 \rightarrow 3H^+ + PO_4^{-3},\ \Delta H_f^0 = -1277.4\ \text{kJ} \quad \text{.....(17)}$$

$$C_2H_2O_4 \rightarrow 2H^+ + C_2O_4^{-2},\ \Delta H_f^0 = -818.3\ \text{kJ} \quad \text{.....(18)}$$

$$Al \rightarrow Al^{+3},\ \Delta H_f^0 = -531.4\ \text{kJ} \quad \text{.....(19)}$$

$$H_2O \rightarrow H^+ + OH^-,\ \Delta H_f^0 = -230.1\ \text{kJ} \quad \text{.....(20)}$$

In above equations, the heat of exothermic in Eqns. 16~18 can be removed before anodization when cooled down the solution in the isothermal tank. However, the exothermic reaction of Eqn. 19 and Eqn. 20 appear during anodizing, those called local heat. The local heat should

quickly be removed by cycling or agitating electrolyte, otherwise the local cracking presents on the AAO surface, showed as Fig. 4.27 (a). The ceramic properties of AAO are sensitive to the temperature difference. When the temperature difference higher than 8 $^{o}$C between the inside and outside of the electrolyte in our experiment, the AAO presents uniform cracking, showed as Fig. 4.27 (b). Anodic voltage controls the anode sample in the anodizing or pitting region. The higher the voltage, the higher electrochemistry reaction; therefore, at first, the oxide film breaks down due to mechanical stress of gas evolves from AAO. Then, aggressive ions of $Cl^{-}$, $SO_4^{-2}$, or $PO_4^{-3}$ are adsorbed at the bare metal and enhances active dissolution. The AAO pitting images showed as Fig. 4.27 (c) and (d). The grain boundaries that appear on AAO always reduce the ordering of nanopores on the AAO. The high concentration of attacking ions ($SO_4^{-2}$, $F^{-}$, $PO_4^{-3}$…) causing grain boundaries appears easily, showed as Fig. 4.27 (e). An unstable current density caused sub-holds appearing, showed as Fig. 4.27 (f). Furthermore, the post treatment of pore widening is used for modifying nanopores. When the pore widening time of the AAO is insufficiend, the random pores appear. On the contrary, over pore widening causes the breaking pores to appear, showed as, Fig. 4.27 (g) and (h).

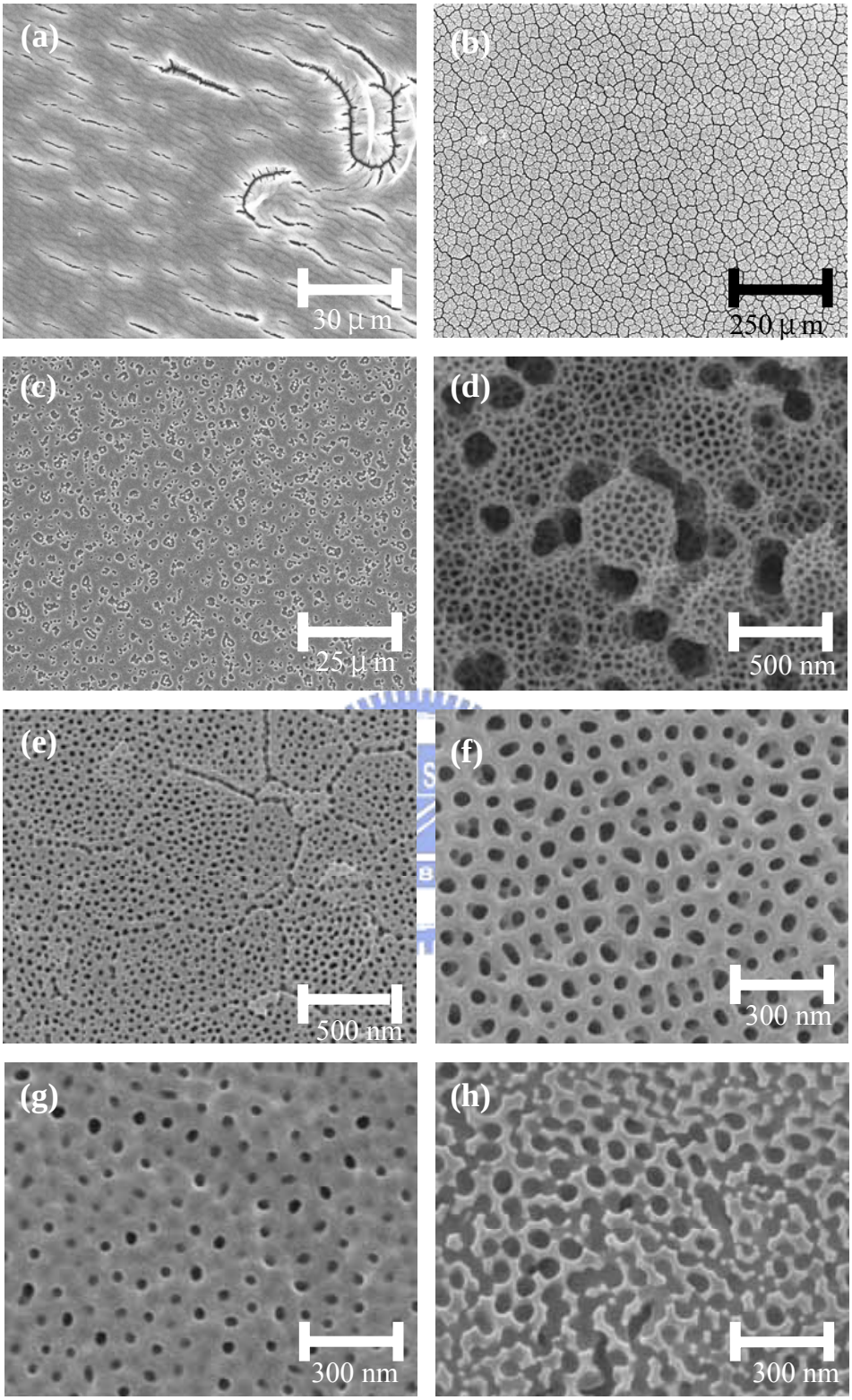


**Fig. 4.27** The SEM images showed the failed AAO when the unsuitable conditions used in anodization; local heat (a), thermo cracking (b), defects (c), pitting (d), grain boundary (e), sub-holds (f), random (f), and breaking (g).

## 4.5 Sn nanocrystals, whiskers, nanowires, particles and nanospheres forming inside (on) AAO

Tin (Sn) is a low melting temperature and electrically conductive metal. Because Sn provides attractive properties, such as excellent solderability, ductility, electrical conductivity, and corrosion resistance, it has been greatly used in the integrated circuit (IC) package industry. One-dimensional nanostructures such as nanowires and nanospheres have been explored for a wide range of applications that take advantage of their unique electric, magnetic, optical, and mechanical properties and their wide range of potential applications in nanodevices. With the continued demand for miniaturization of electronic and optical devices, nanowires are expected to play a major role as devices as well as interconnect in future integrated circuit.

The insulating and ceramic characteristics of AAO are beneficial to forming nanomaterials inside or on its surface. Based on the AAO template, Sn nanocrystals, whiskers, nanowires, particles, and nanospheres were formed inside/on AAO by various processes. Temperature variations always changed some physical phenomenon in the changed on materials: for example, atoms diffusion, thermal expansion, and self-surface tension physical effects. In the bulk materials, the physical phenomenon changed are not obvious when temperature change was minimal; however, in the nanomaterials, it can be clearly observed with little change in temperature.

### 4.5.1 Injection of Sn into AAO forming nanowires

The schematic diagram of metal/ceramic composite in the experimental sample after injection Sn into AAO is shown in Fig. 4.28. It includes 100 μ m thickness of Sn metal, 10 μ m thickness of AAO, 0.04 μ m thickness of barrier layer, and 100 μ m thickness of Al substrate. Furthermore, keeps Sn metal as the substrate, but remove Al foil, barrier layer, and partial of AAO,

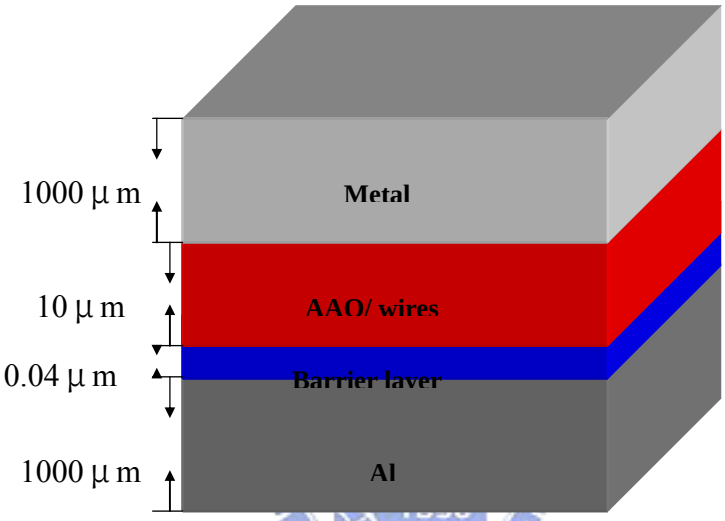


**Fig. 4.28** The schematic diagram of metal/ceramic composite of experimental sample.

so the ordered and short Sn nanowires can expose on the AAO. High density, ordering, and uniform nanowires stands on the AAO would be useful for the device that require high current density or the high surface area application. In order to obtain the ordering nanowires on the AAO surface the partial of bottom AAO was removed by wet-chemical etching. The schematic diagram of Fig. 4.29 shows the AAO structure (a), to inject melt into the AAO (b), nanowires formed in the AAO (c), removed Al

substrate (d), removed barrier layer(e), and removed partial of AAO (f) let partial of Sn nanowires expose and stand on the AAO surface.

The basic characteristics of Sn bulk material of micro-morphology, composition, and melting point were detected by optical microscopy (OM), X-ray diffraction (XRD), and Differential Scanning Calorimetry (DSC). The OM image showed single phase of Sn with grains size about 150 to 500 μ m, as Fig. 30 (a), the XRD also showed pure Sn peaks, as Fig. 30 (b). Also, the DSC showed the melting point of pure Sn is 231.9°C and re-crystallization temperature is 204.2 °C, as Fig. 30(c).

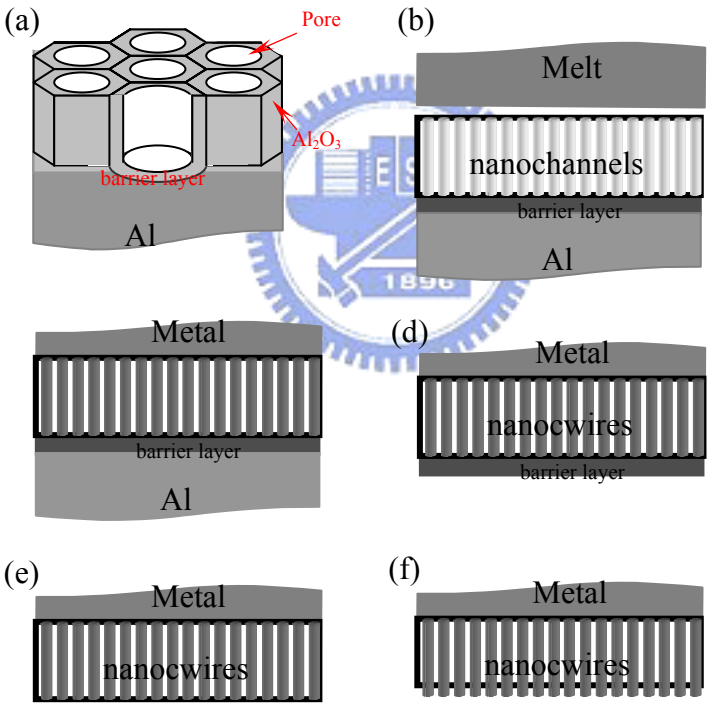


**Fig. 4.29** The schematic diagram of AAO structure (a), to inject melt into the AAO (b), nanowires formed in the AAO (c), removed Al substrate (d), removed barrier layer(e), and removed partial of AAO (f).

Since AAO is electrically insulating, it has served as an excellent medium for embedding such metallic nanostructures. The dimensions of nanostructures are defined by the AAO. The extra force for melts into nanochanel is proportional to the channel diameter and surface tension of melts. The critical pressure (P) needed for melt to permeate into the AAO can be calculated by the formula of $P=F/A=4\gamma\cos\theta/d$ [102], where F is the normal force, A is the area of the specimen, $\gamma$ is the surface tension of the melt, $\theta$ is the contact angle between AAO and the melt, and d is the diameter of the nanochannel. In our experiment, the AAO pore sizes are 60 nm and 1 5 nm, the specimen area is 3.8 $cm^2$, $\gamma$ of Sn is 0.544 N/m (Newton/meter) [113], and $\theta$ is estimated to be $158^o$~$173^o$ [114]. Using the above equation. The critical force for melt injected to the 60 nm and 15 nm nanochannels, therefore, will be around 2017~2161 kg and 8069~8643 kg. Using the equation, the plot of applied force versus channel diameter in nanometers is shown as Fig. 4.31. The plot shows that the required applied

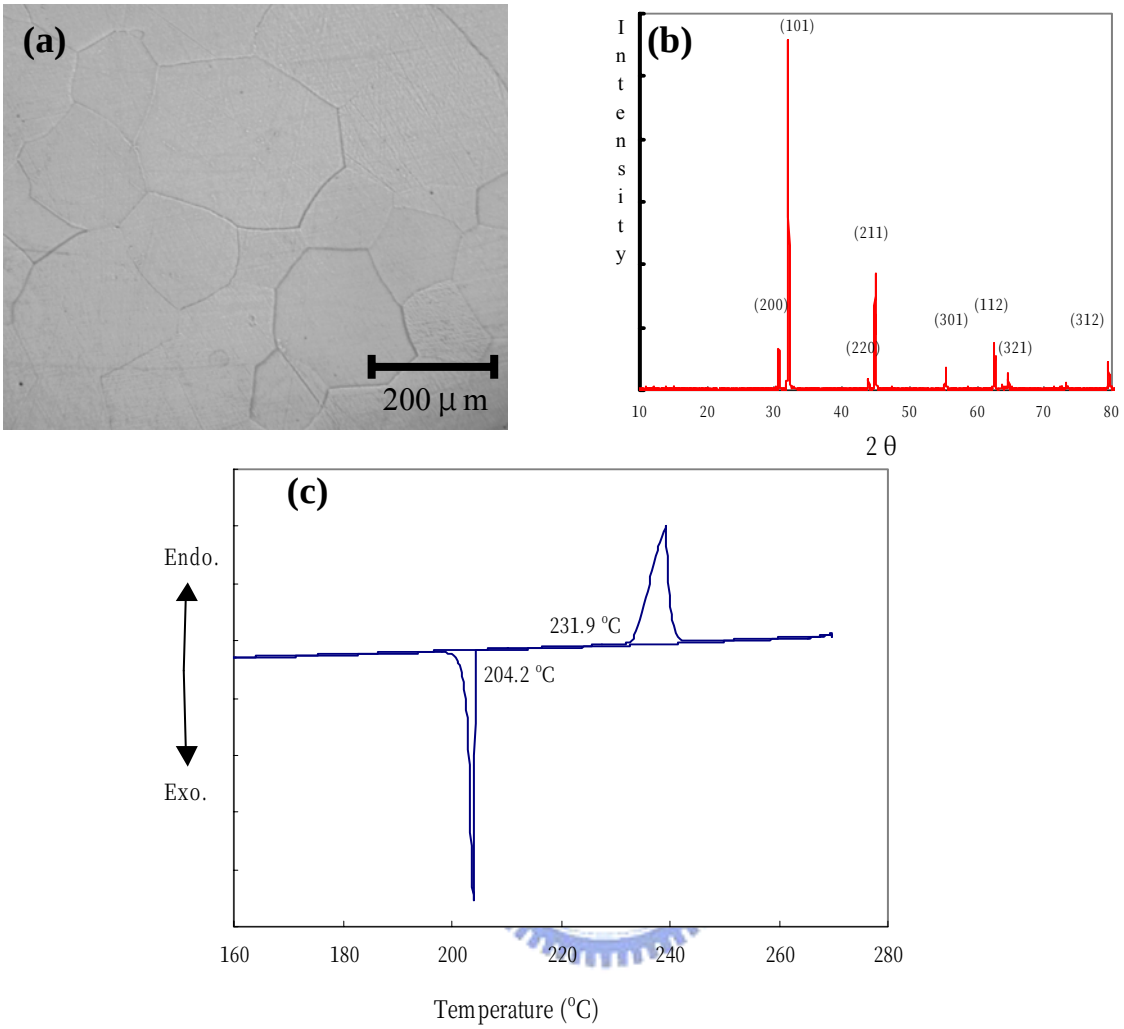


**Fig. 4.30** The basic Sn bulk material characteristics of micro morphology (a), composition (b), and melting point (c) were detected by OM, XRD, and DSC.

pressure increased when pore size decreased. In Fig. 4.31, when the pore diameter is 10 nm and the specimen area is 3.8 $cm^2$, the applied pressure should be 1344.8~2160.8 bar (7.8~12.6 ton). It is difficult to obtain a high pressure such as 1300 bar from gas pressure in a general Lab., However, a highly force can be easily obtained by using hydraulic force. Therefore, such an approach was used to fabricate the Sn nanowires using AAO.

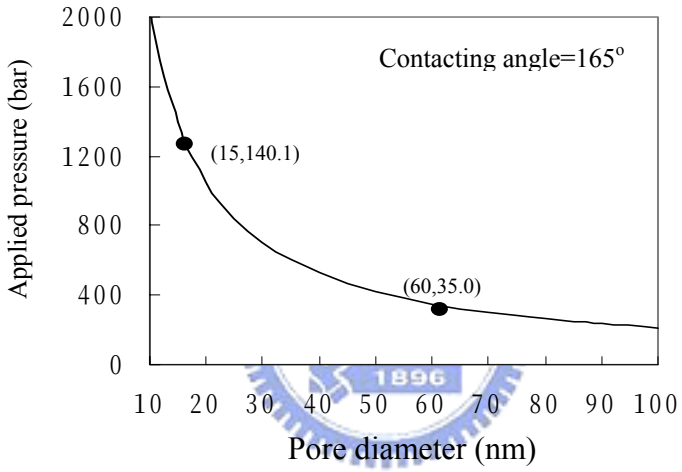


**Fig. 4.31** The curve of critical pressure for melt injected in nanochannel; applied pressure increasing with pore size decreasing.

Because the Sn melt has high surface tension (0.544 N/m), it is difficult to be injected into the nanochannel under the critical force. From the theoretical calculation, when the applied pressure from hydraulic press exceeds 35.1bar (2042 Kg) on the melt, the melt can be injected into the AAO ($\phi$=60 nm); as well as, 140.11bar (8175 kg) for AAO ($\phi$=15 nm). As expected, when the applied pressure was 30 bar (1750 kg) (i.e., less than the critical force), the melt could not be injected into AAO ($\phi$=60 nm)

and it was fully spread to form a fully spread thin film on the AAO surface. Figures 4.32(a) illustrate the formed thin film on AAO surface. However, it was expectedly to learn that even after the applied pressure was increased close to critical pressure of 35bar (2042 Kg), the filling ratio of melt inside AAO was low (Fig. 4.32 (b)). In order to obtain dense nanowires in AAO, the applied pressure used was found to be higher than the critical pressure. Figure 4.32(c) shows the top–view image of filling ratio of Sn in AAO that when the applied pressure was 50bar (2817 Kg), the filling ratio was high on the top. However, from the bottom view of Fig. 4.32 (c), the filling ratio is poor,

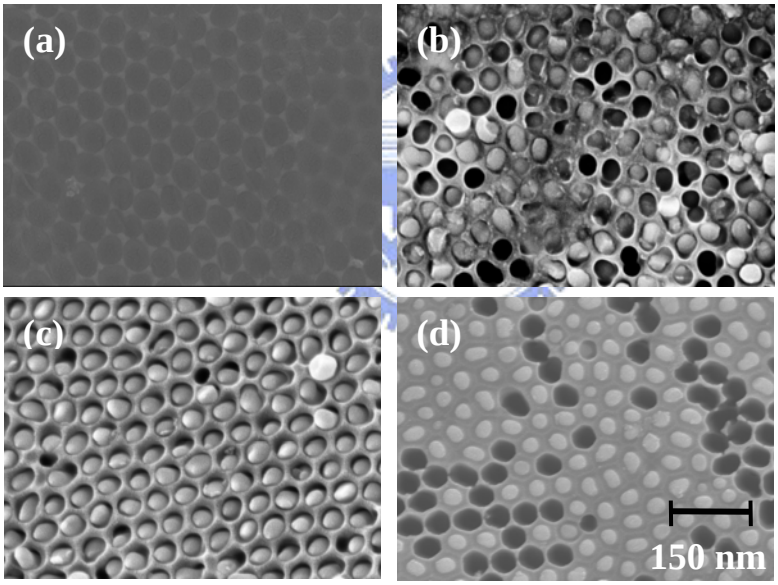


**Fig.4.32** Top and bottom view SEM images of filling ratio of Sn inside AAO (ψ=60nm). Top view images of applied pressure 30bar (1750Kg) (a), 35bar (2042Kg) (b), 50bar (2817Kg) (c), and bottom view of applied pressure 50bar (2817Kg) (d) on the Sn melt.

shows in Fig. 4.32(d). When the AAO pore size was reduced to 15 nm, the various applied pressure in the process was 100bar (5835 kg), 140.1bar (8175 kg), and 20bar (11671 kg), the surface images can be observed as

thin film, poor filling ratio, and high filling, as show in Fig. 4.33 (a)-(c). However, the same issue as above, the bottom filling ratio was poor even the sample has high filling ratio on the top shows in Fig. 4.33(d).

Because a high filling ratio of melt being injected down to the AAO bottom is required to produce sufficient quality Sn nanowires for any physical or chemical characterization test have, it is important to ensure a high filling ratio of Sn produced throughout the work. It was found that moisture and gases retained in the AAO tubes lead to reduce the filling ratio of melt through down to the AAO bottom. The original AAO without any post treatments of drying and degassing had low melt filling ratio inside. From SEM image in Fig. 4.34, it can be seen that when the Sn was pressed

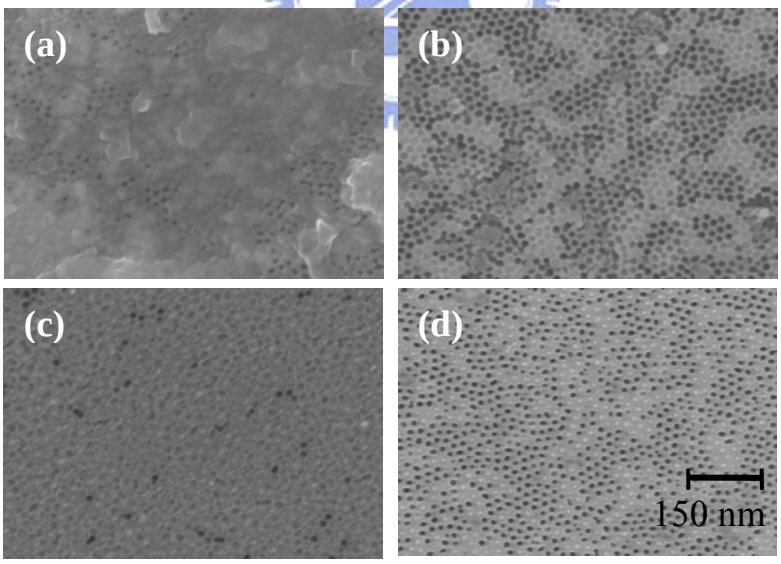


**Fig.4.33** Top and bottom view SEM images of filling ratio of Sn inside AAO (ψ =15nm). Top view images of applied pressure 100 bar (5835 kg) (a), 140.1 bar (8175 kg) (b), 200 bar (11671 kg), and bottom view of applied pressure 200 bar (11671 kg) (d) on the Sn melt.

into the AAO, the channels have address white, otherwise the nanchannels were backed when the tubes are. To ensure proper nanowires were produced, the AAO was placed in a vacuum chamber at high temperature for drying and degassing before melt was injected into the treated AAO. As shown in Fig. 4.35(a), the filling ratio was low in the original AAO before drying and degassing. Even after a 1 hr, 450 ºC high temperature drying, the filling ratio was still low (b). However, after drying (450 ºC) and degassing ($10^{-3}$ torr) for 10 to 25 min, the filling ratios were found to be improved as shown in Fig. 4.35(c)-(f). A cross section view of the SEM image, confirms that the Sn nanowires go down to the AAO bottom, showed as Fig. 4.36.

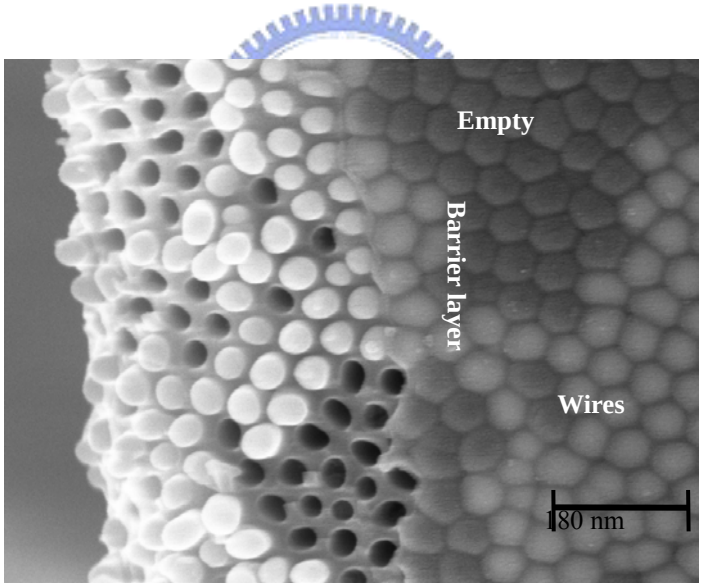


**Fig. 4.34** The SEM images of bottom AAO with partial Sn inside; barrier layer retains on AAO (image right side), Empty holes (black), and Sn nanowires inside the holes (white).

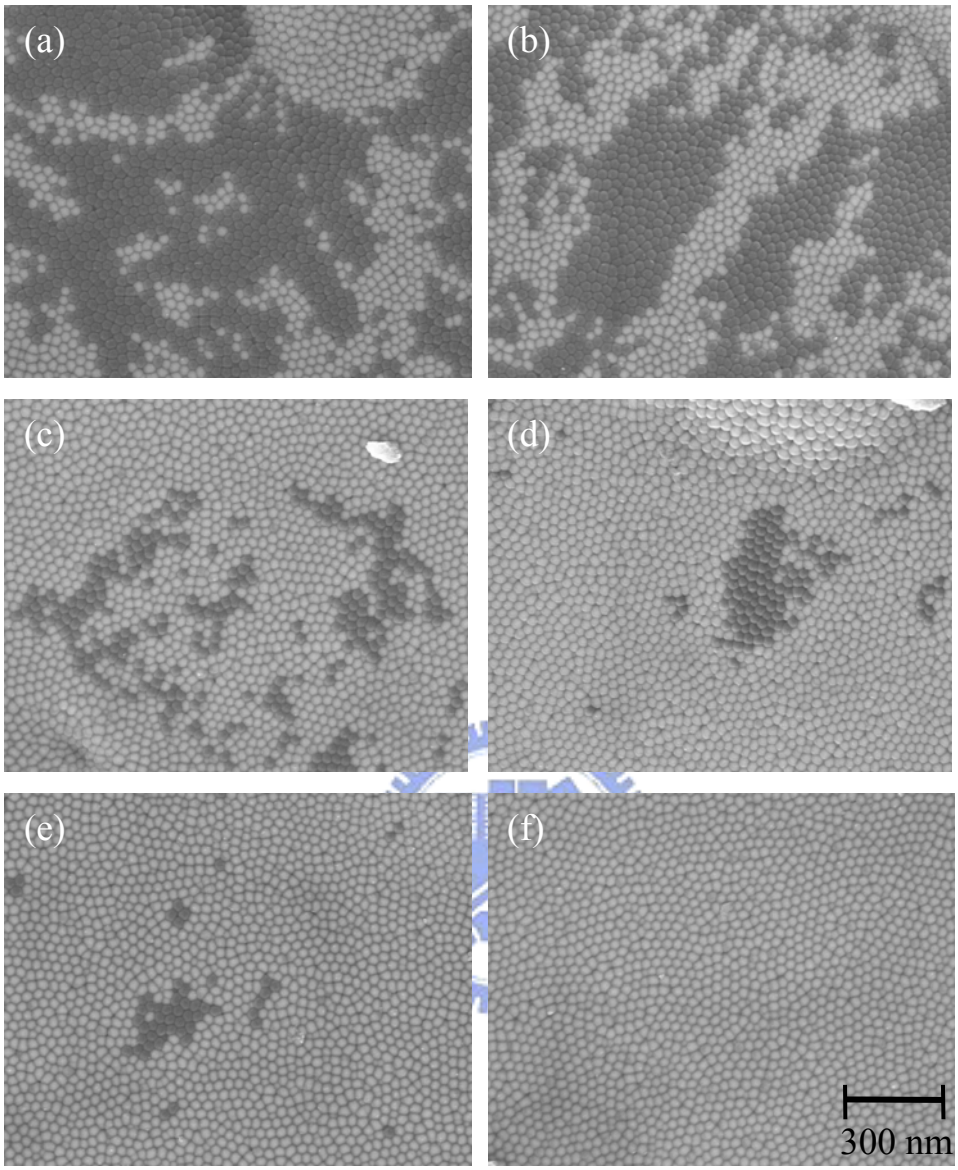


**Fig. 4.35** The SEM images of bottom AAO showed the original (a) AAO with low filling ratio of Sn inside that Sn inside AAO made AAO color from black changed to white. Improved the filling ratios of Sn inside AAO by high temperature (450 $^{o}$C for 1 hr) drying (b) and high temperature (450 $^{o}$C) vacuum ($10^{-3}$ torr) treatments; 10 min (c), 15 min (d), 20 min (e), 25 min (f).

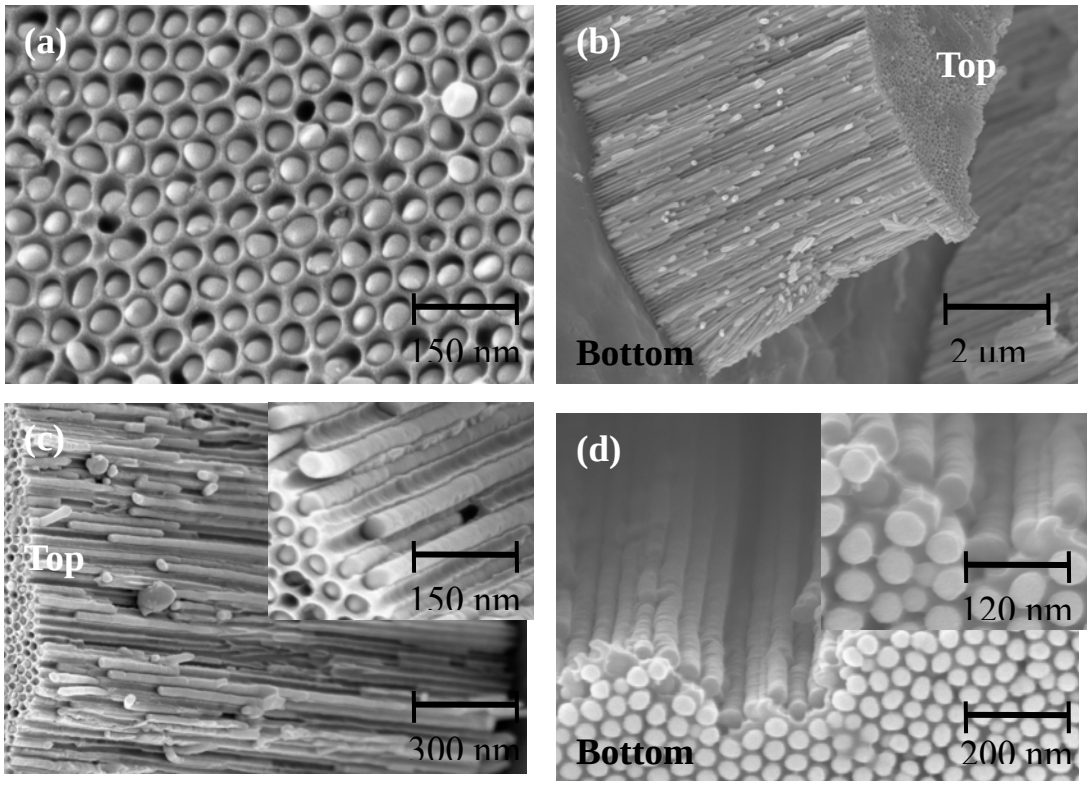


**Fig. 4.36** SEM image of Sn melt inside AAO, which formed Sn nanowires: (a) top view, (b) cross-section view, high magnification of cross-section (top) view, and high magnification of cross-section (bottom) view.

When materials size decrease the surface-to-volume ratio increases. Therefore, atoms on the materials surface increase. This effect may cause materials physical characteristics change, for example, activity increases and melting point decreases. In our experiment, we also found this effect. When the dimension of bulk Sn decreases to nano scale of nanowires, the Sn melting point decreases. Figure 4.37, the melting point bulk Sn is 231.7 $^{o}$C; however, the melting point of 60 nm diameter and 15 nm diameter Sn nanowires decrease to 227.1 $^{o}$C and 224.1 $^{o}$C. Furthermore, the results also can be found on Bi materials, showed as Fig. 4.38. Moreover, To collect free-standing Sn nanowires, the AAO template was dissolved thoroughly

in 0.2% sodium hydroxide (NaOH) solution solution at ~23 $^0$C for 2hr. After sonication and centrifugal sedimentation the solution was carefully removed with syringe and replaced with de-ionized water. This was repeated several times to rinse the nanowires. The residual nanowires were then transferred into 0.5 ml isopropanol and dispersed by sonication. A drop of the isopropanol suspension was dropped onto Cu grid with carbon film for TEM observation, showed as Fig. 4.39.

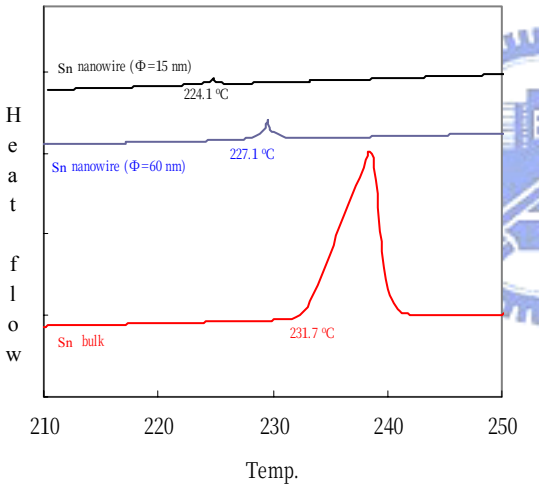


**Fig. 4.37** DSC curves of the melting point on bulk Sn is 231.7 °C, 60 nm diameter and 15 nm diameter Sn nanowires decrease to 227.1 °C and 224.1 °C.

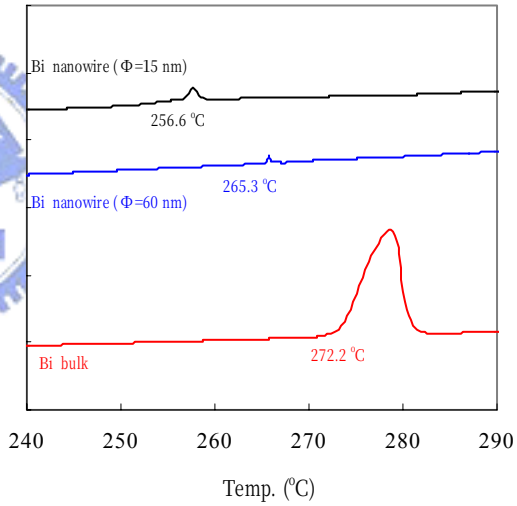


**Fig. 4.38** DSC curves of the melting point on bulk Bi is 272.2°C, 60 nm diameter and 15 nm diameter Bi nanowires decrease to 265.3 °C and 256.6 °C.

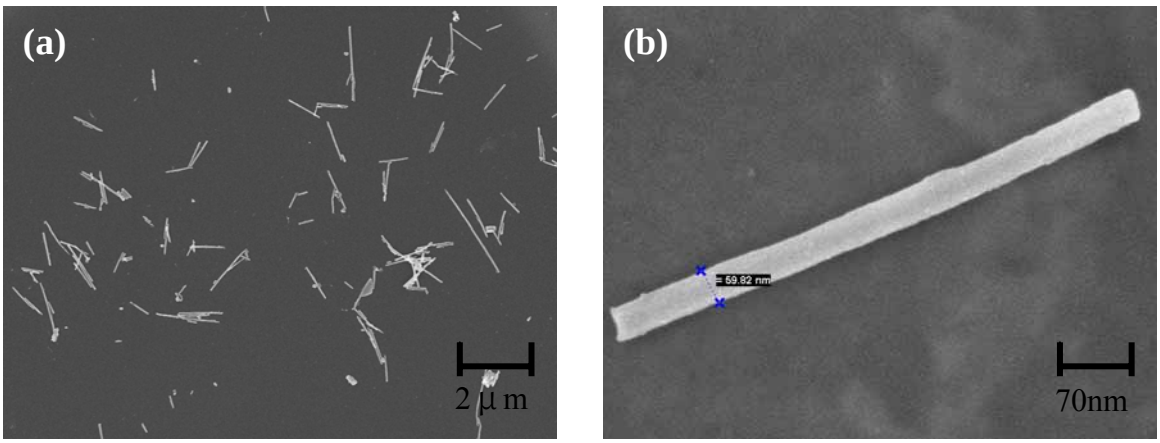


**Fig. 4.39** The SEM images of Sn nanowires were collected on the Cu Cu grid after AAO was dissolved in 0.2% NaOH solution; low magnification image (a), and high magnification image (b).

Figure 4.40 shows a typical TEM image of a randomly selected ~60 nm diameter single Sn nanowire which is dense, continuous, and uniform in diameter throughout the entire length of the nanowire. Although it was clear from Fig. 4.39(b) that the nanowires had the same length as the AAO thickness (10μm), SEM and TEM observation of free standing nanowires revealed that the majority of the wires were in the 1-5μm range. This was due to the sonication and centrifugation steps in the nanowire separation procedure. The selected-area electron diffraction (SAED) pattern along the length of the wire was the same indicating that the wires were single crystals. After indexing several SAED patterns from randomly selected nanowires, it

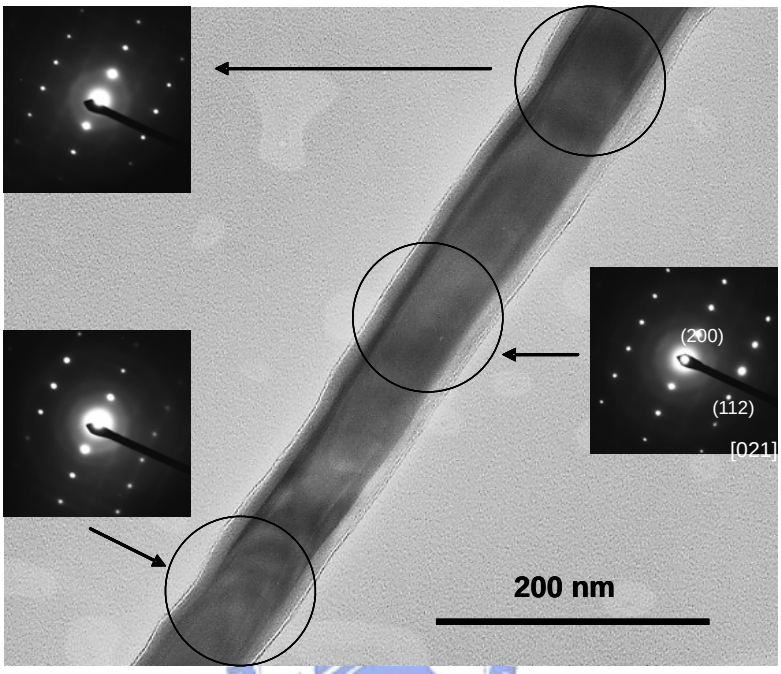


**Fig. 4.40** TEM micrograph of a randomly selected single nanowire (60 nm). The black circles indicate the areas from which the electron diffraction pattern (ED) was taken. Note that the ED patterns remain the wire length. The zone axis in this case was [021] and the growth direction is [100].

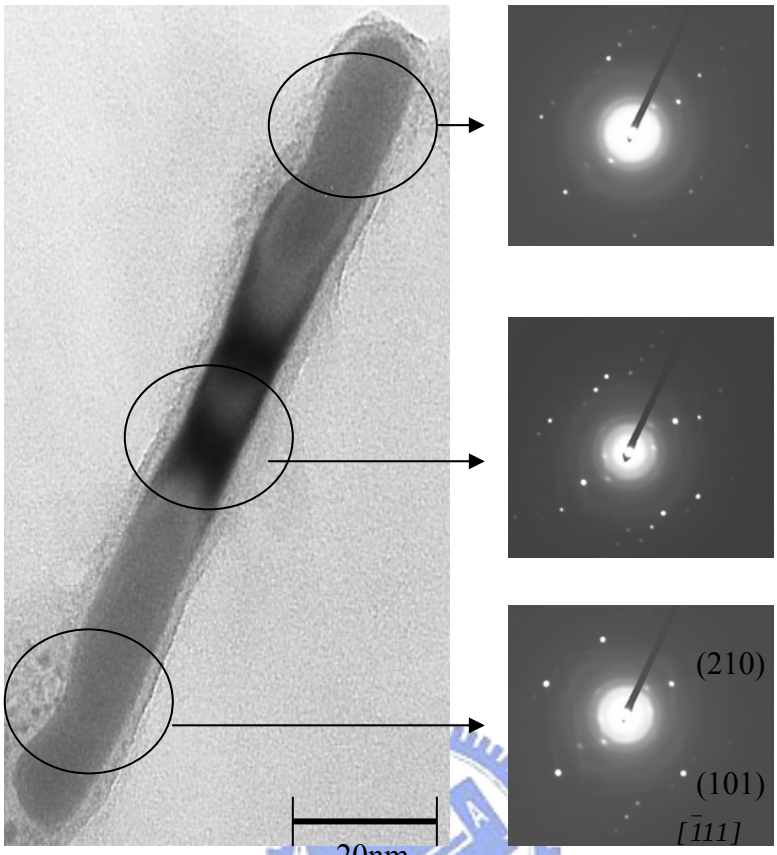


**Fig. 4.41** TEM micrograph of a randomly selected single nanowire (15 nm). The zone axis in this case was [$\bar{1}11$] and the growth direction is [101].

was deduced that the growth direction for some wires was along the [100] and for others along [001] direction. This is in partial agreement with results reported by Tian et al. [127] for single crystal Sn nanowires synthesized by electrochemical deposition. They found that 90% of the wires had preferred [100] growth direction while most of the others grew in the [110] direction. We suggest that the variation in the preferred orientation may have resulted from the different fabrication methods.

Figure 4.41 shows a randomly selected ~15 nm diameter Sn nanowire. The growth direction of wire was along the [101]. From the TEM results of Fig. 40 and 41, there are different prefer growth direction between 60 nm and 15 nm Sn nanowires. Because the 60 nm AAO was made by oxalic acid solution, but 15 nm AAO was made by sulfuric acid solution the various oxalate and sulfate ions retain in the AAO walls after anodization. The various inclusions in the AAO tube may cause different preferred orientation of Sn nanowires growing during Sn melt solidifying in the AAO tubes.

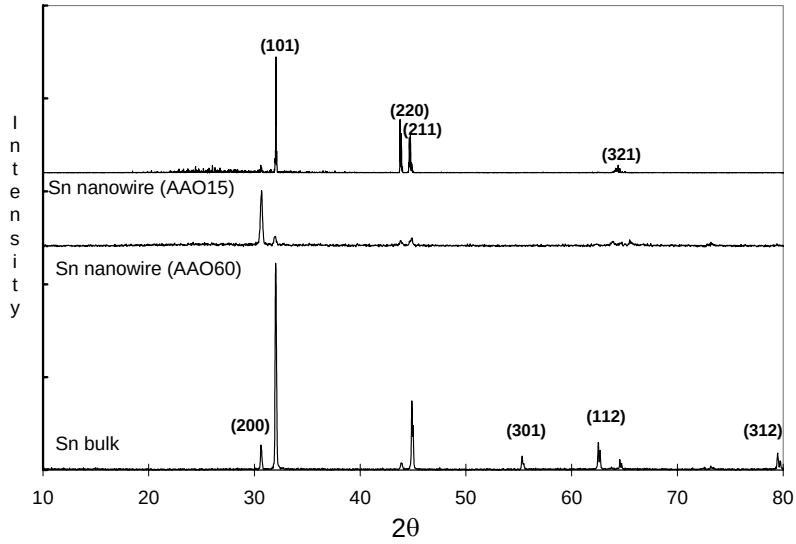


**Fig. 4.42** XRD patterns of large scale AAO/Sn nanowire composite.

XRD was used to study the phase and crystal orientation of the Sn nanowire arrays. The XRD experiment was performed on the bottom face of the AAO–nanowire composite after removing the Al and barrier layer as described above. The XRD patterns, as shown in Fig. 4.42, can be indexed

to the body-centered-tetragonal (bct) β-Sn structure with lattice constants a=b=5.82 Å; c =3.17 Å. All the observed peaks, both for the AAO(ϕ=60 nm) and AAO(ϕ=15 nm), were found to match very closely to the standard polycrystalline β-Sn (JCPDF, 4-673). For AAO(ϕ=60 nm), the intensity for (200) was almost 3.0 times higher than the secondary peak (101). Also, For AAO(ϕ=15 nm), the intensity for (101) was almost 2.0 times higher than the secondary peak (220).This is higher than the expected ratio of the intensities of (200) and (101) for β-Sn powder. From this and TEM observation, it may be concluded that for most of the nanowires in the template, [100] maybe the preferred orientation of 60 nm Sn nanowires growth, and [101] maybe the preferred orientation of 15 nm Sn nanowires growth. In addition, our results and results from Tian et.al [127], it appears that regardless of the fabrication process, [100] may be the preferred growth direction for Sn nanowires in the 40-160 nm diameter ranges.

In order to expose standing nanowires in a controlled manner, further study was carried out to find a suitable condition to partially etch away the Sn-filled template after completely etching away the barrier layer. A schematic side view diagram of Sn inside AAO template is showed as Fig. 4.43(a). A thin film of barrier layer exists on the bottom will always be a problem for devices testing conductivity. For this reason, we subject to retain Sn bulk as substrate but remove aluminum substrate and barrier layer, the schematic diagram showed as Fig. 4.43(b).

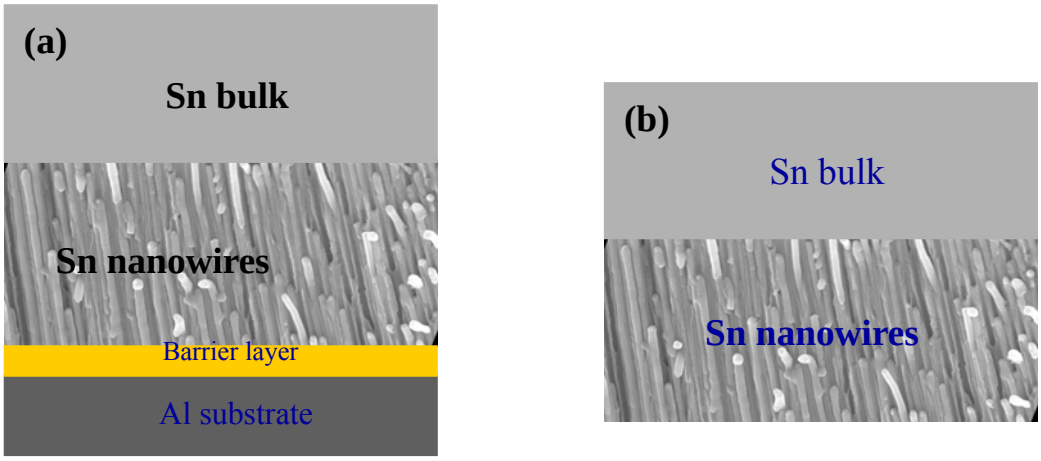


**Fig. 4.43** A schematic side view diagram of Sn inside AAO template; with Al substrate and alumina barrier layer (a), without Al substrate and alumina barrier layer (b).

Aluminum substrate could be dissolved in a mixture 10 wt% $CuCl_2$+ 5 vol% HCl solution. When the sample was immersed in the solution at 23 $^oC$ for 3 min, the barrier layer instead of the aluminum was on the sample surface, showed as Fig. 4.44(a). The solution of 5 vol% $H_3PO_4$ was common used for dissolving or pore widening on AAO. When the AAO bottom was etched in 5 vol% $H_3PO_4$ solution at 23 $^oC$ for 20 min, the partial barrier layer dissolved beginning from the grain boundary, show as Fig. 4.44(b). The barrier layer can be dissolved by 5 vol% $H_3PO_4$; however, the solution reacted to the metal Sn too, at 23 $^oC$ for 30 min etching, showed as Fig. 4.44(c).

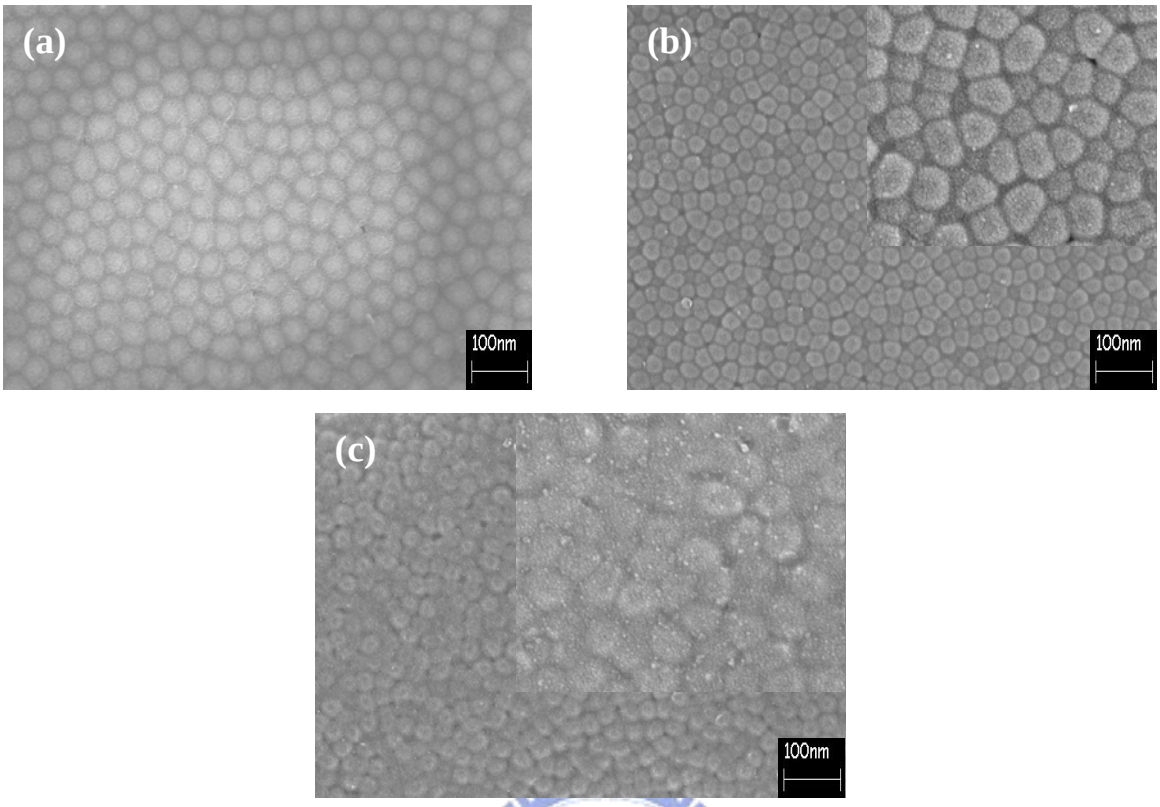


**Fig. 4.44** SEM images of sample bottom view; after aluminum substrate was removed, the barrier layer presents (a); furthermore, grain boundary of barrier layer etched by 6% $H_3PO_4$ solution for 20min at 23°C (b); the solution reacted to the metal Sn for20min at 23°C (c)

In order to dissolve barrier layer but not the metal Sn we used sodium hydroxide (NaOH) solution as a removing solution for the barrier layer. A series of SEM images of 180 nm, 60 nm, and 15 nm samples barrier layer and partial AAO dissolving in NaOH solution with various etching time are showed in Fig. 4.45, Fig.4.46, and Fig.4.47. For 180 nm AAO sample, barrier layer can be fully removed by 0.2 wt% NAOH at 23°C for 4hr, showed as Fig. 4.45 (a). Then partial AAO can be removed and short nanowires

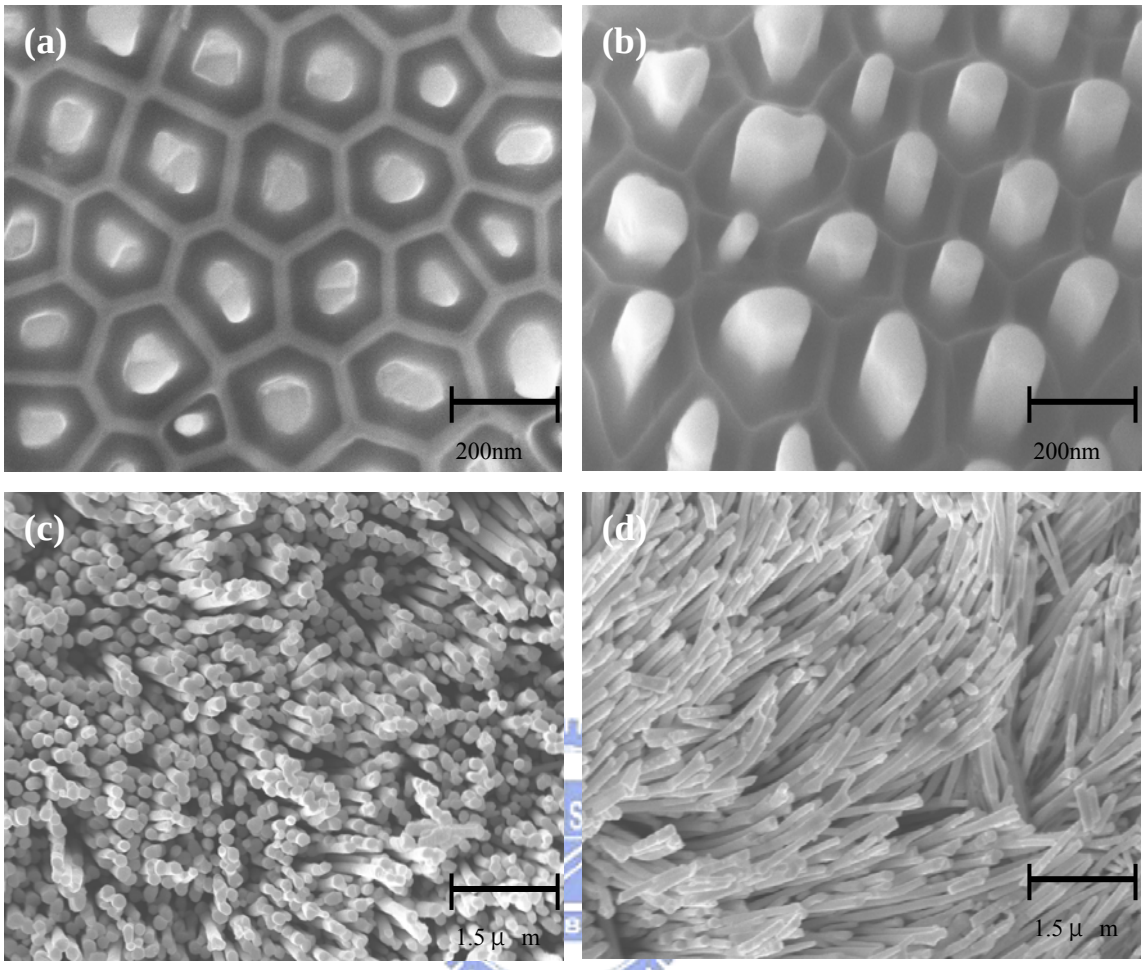


**Fig. 4.45** SEM images of AAO (ψ=180nm) sample bottom view; barrier layer was removed by 0.2 wt% NAOH at 23°C for 4hr (a), 4hr 30min (b), 5hr (c), 5hr 30min (d).

exposed on the AAO bottom when etching time increases to 4hr 30 min, showed as Fig. 4.45 (b). After barrier and partial AAO were removed, the solving rate of AAO in the solution increase in the short time, showed as Fig. 4.45 (c), and 4.45 (d). During anodization to aluminum, the applied voltage determines the barrier layer thickness, AAO pore size and pore distance; as well as, two experience formulas can estimate the pore size and the pore distance of AAO. The pore size with voltage is: C=mV, where C is cell size (nm), V is anodizing voltage (V), and m is a constant (2~2.5); the pore distance with voltage is V=(2R-10)/2, where 2R is Spacing distance (5~1000 nm). [16] The AAO with a pore size of 15 nm (applied volt. =18V) had a barrier layer thickness thinner than the AAO with pore size 60 nm (applied volt. =40V). Therefore, the barrier layer removing time of the 60 nm, and 15 nm AAO samples are less than 180 nm AAO.

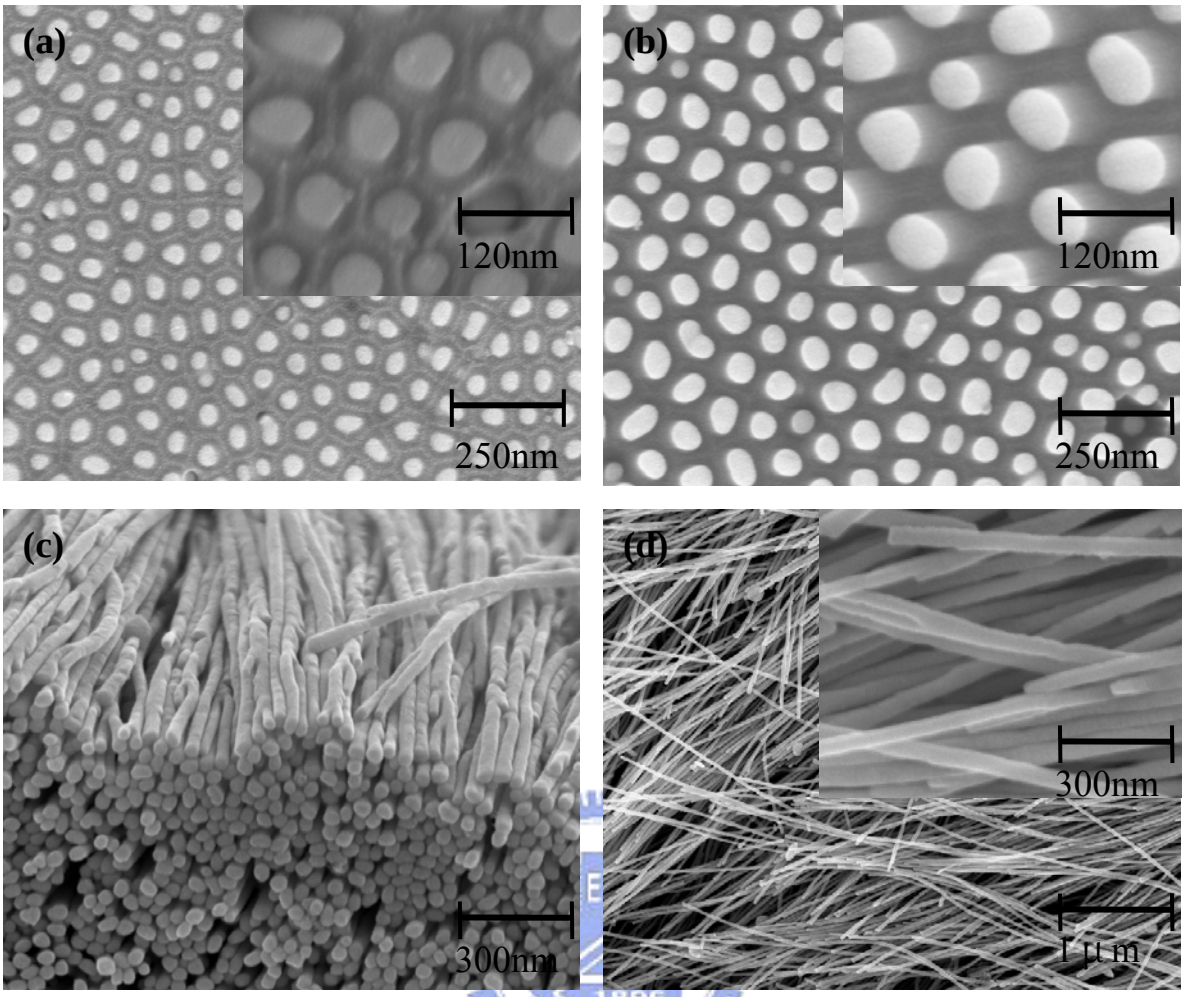


**Fig. 4.46** SEM images of AAO (ψ=60nm) sample bottom view; barrier layer was removed by 0.2 wt% NAOH at 23°C for 2hr (a), 2hr 30min (b), 3hr (c), 3hr 30min (d).

For AAO (ψ=60 nm),when the barrier layer was removed by 0.2 wt% NaOH solution at 23°C for 2hr pore walls still exist, but pores were open on the center of the barrier layer (Fig. 4.46(a)). Pore walls dissolved (Fig. 4.46(b)) after 2hr 30min of etching. Also, insufficient AAO can keep Sn nanowires up in the AAO when deep pore walls were dissolved, and the wires touch to each other after 3hr of etching (Fig. 4.46(c)). Both the barrier layer and AAO were dissolved in the solution after 4hr etching such that the nanowires are at random level on the substrate (Fig. 4.46(d)).

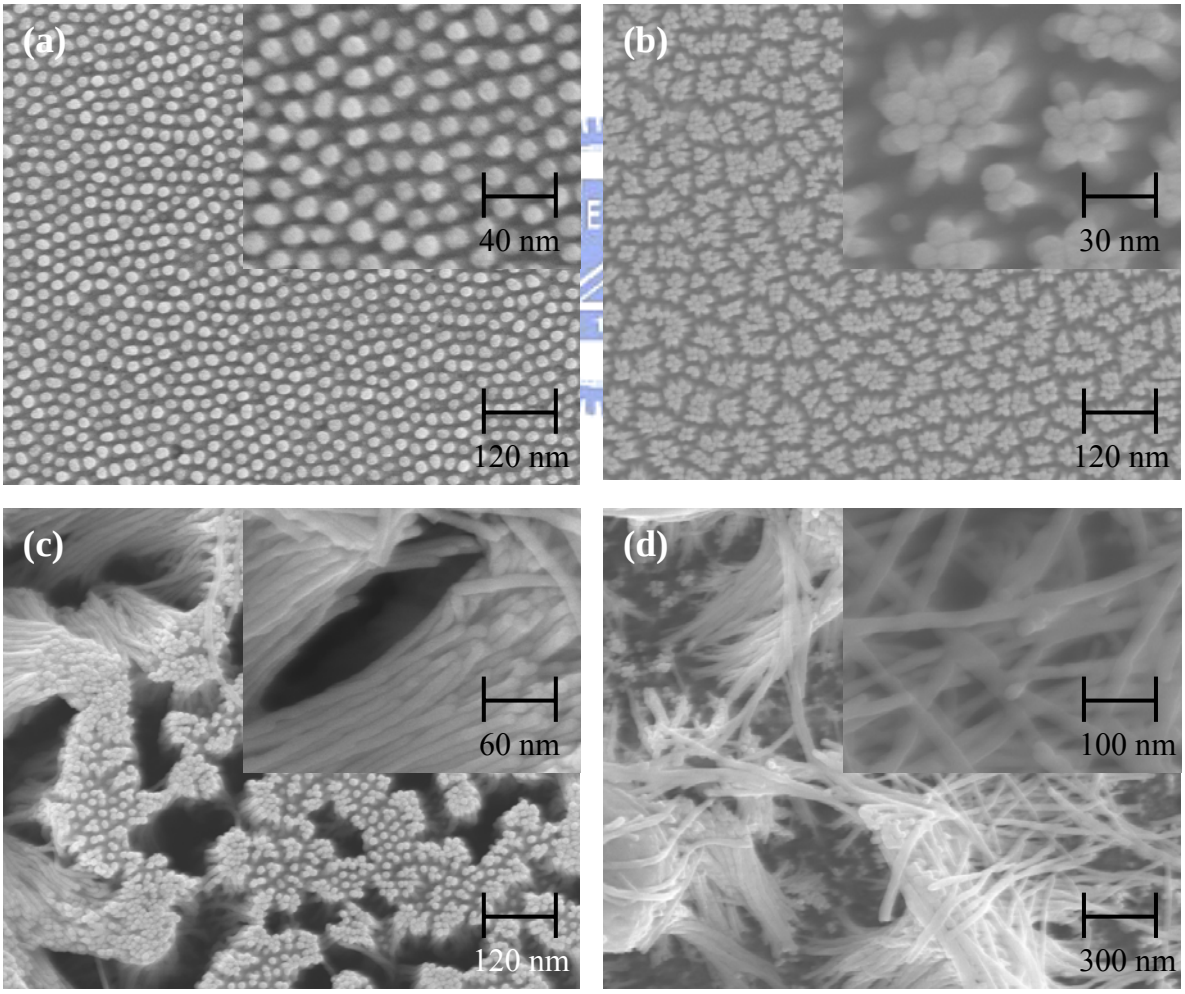


**Fig. 4.47** SEM images of AAO (ψ=15nm) sample bottom view; barrier layer was removed by 0.2 wt% NAOH at 23°C for 30min (a), 40min (b), 50min (c), 60min (d).

For AAO (ψ=15 nm) sample, barrier layer can be removed after 30 min, showed as Fig. 4.47(a). When etching time is more than 30min. the over etching happened on the sample. Consequentially, the nanowires, tops touch to each other after 40min of etching (Fig. 4.47(b)). Most of the AAO dissolved in the solution and the wires could not stand on the substrate vertically after 50min of etching (Fig. 4.47(c)), and wires were flat on the substrate after 60min etching (Fig. 4.47(d). Furthermore, the order nanopattern retains on the Sn bulk can be observed after barrier layer, AAO, and nanowires were removed from the bulk surface, showed as Fig. 4.48.

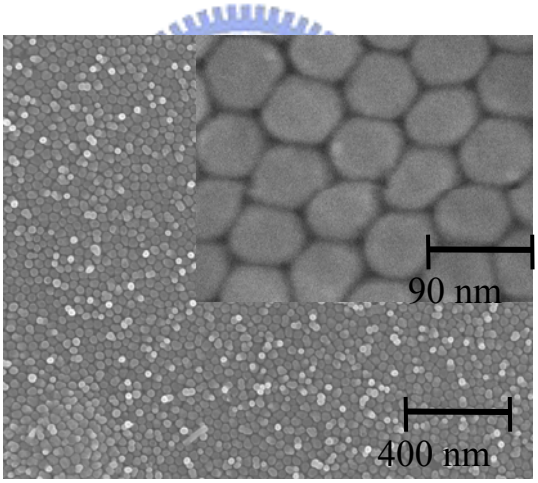


**Fig. 4.48** SEM image of the order nanopattern retains on the Sn bulk surface.

### 4.5.2 Formation of Sn whisker and particles on AAO

The spontaneous room temperature growth of low melting point metal whiskers, such as Sn (231.9 $^{o}$C), Cd (321.1 $^{o}$C), Bi (271.3 $^{o}$C), In (156.6 $^{o}$C), and Zn (419.5 $^{o}$C) was discoveries in the industries. The possible growth mechanism have been pointed out, including residual stresses released, intermetallic formation, recrystallization, externally applied compressive stresses, bending or stretching, scratches or nicks, coefficient of thermal expansion mismatches [128-130].Tin whiskers are electrically conductive, crystalline structures of tin that sometimes grow from surfaces where tin (especially electroplated tin) is used as a final finish. Numerous electronic system failures have been attributed to short circuits caused by tin whiskers that bridge closely-spaced circuit elements maintained at different electrical potentials. Tin whiskers have dimension with 1 to 10 mm lengths and 1 um to 10 um diameters that growth rate is between 0.03 to 0.9 mm/yr. As well as, various shapes of tin whiskers has been observed, such as straight, kinked, hooked, nodules, pyramidal or forked [131-132].

For the Sn whisker sample, Sn melt was injected into AAO template with 60 nm diameter. After melt solidify to Sn nanowires that a high residual stress retains in the AAO. A residual stress releases from AAO would be a driving force for Sn whisker growth. Especially, when the surrounding temperature is below and close to the Sn nanowires melting point (m.p.) the whiskers will grow soon in a few minutes. In order to obtain a temperature in correctly range, the differential scanning calorimetry (DSC, Perkin Elmer Pyris 1) equipment was used for control

various temperature. So, the Sn nanocrystalls, whiskers, and nanospheres following form with temperature increasing on the AAO.

Since materials size reduces to the nanoscale the melting point (m.p.) is always following reduce. The m.p. of 60 nm diameter Sn nanowire is 227.1$^{o}$C that is lower than bulk Sn of 231.7$^{o}$C. The bulk Sn and 60 nm diameter Sn nanowire endothermal curves of DSC curves as shows in Fig. 4.37. Based on the 60 nm Sn nanowires m.p., when the temperature was controlled below m.p. the Sn crystals grow on the AAO. As well as, when the temperature closes to the m.p. Sn prefers to form whiskers. However, when the temperature was high than the m.p. Sn whiskers trend to agglomeration and forming Sn particle. The detail SEM images of Fig. 4.49 show Sn whiskers and particles growth on 60 nm diameter pores of AAO (with Sn inside) surface with various temperature during the heating and cooling rate(50$^{o}$C/min) were controlled by DSC. The SEM image shows a clean surface of AAO with Sn inside at 25$^{o}$C (a). When increases temperature to 220$^{o}$C the nanocrystals form (b). Furthermore, whiskers form on the AAO when the temperature is 226$^{o}$C (c), whiskers agglomeration at 228$^{o}$C (d), whiskers agglomeration and forming a sphere at 229$^{o}$C (e), few whiskers connect to sphere at 230$^{o}$C (f), micron sphere forming at 231$^{o}$C (g), most spheres and few whiskers on the AAO at 231$^{o}$C (h), micron and sub-micron spheres on the AAO at 240$^{o}$C (i). On the other hand, when reduced the heating and cooling rate as 5$^{o}$C/min controlling by the DSC, the Sn trend to form nanowhiskers on the AAO, show as Fig. 4.50.

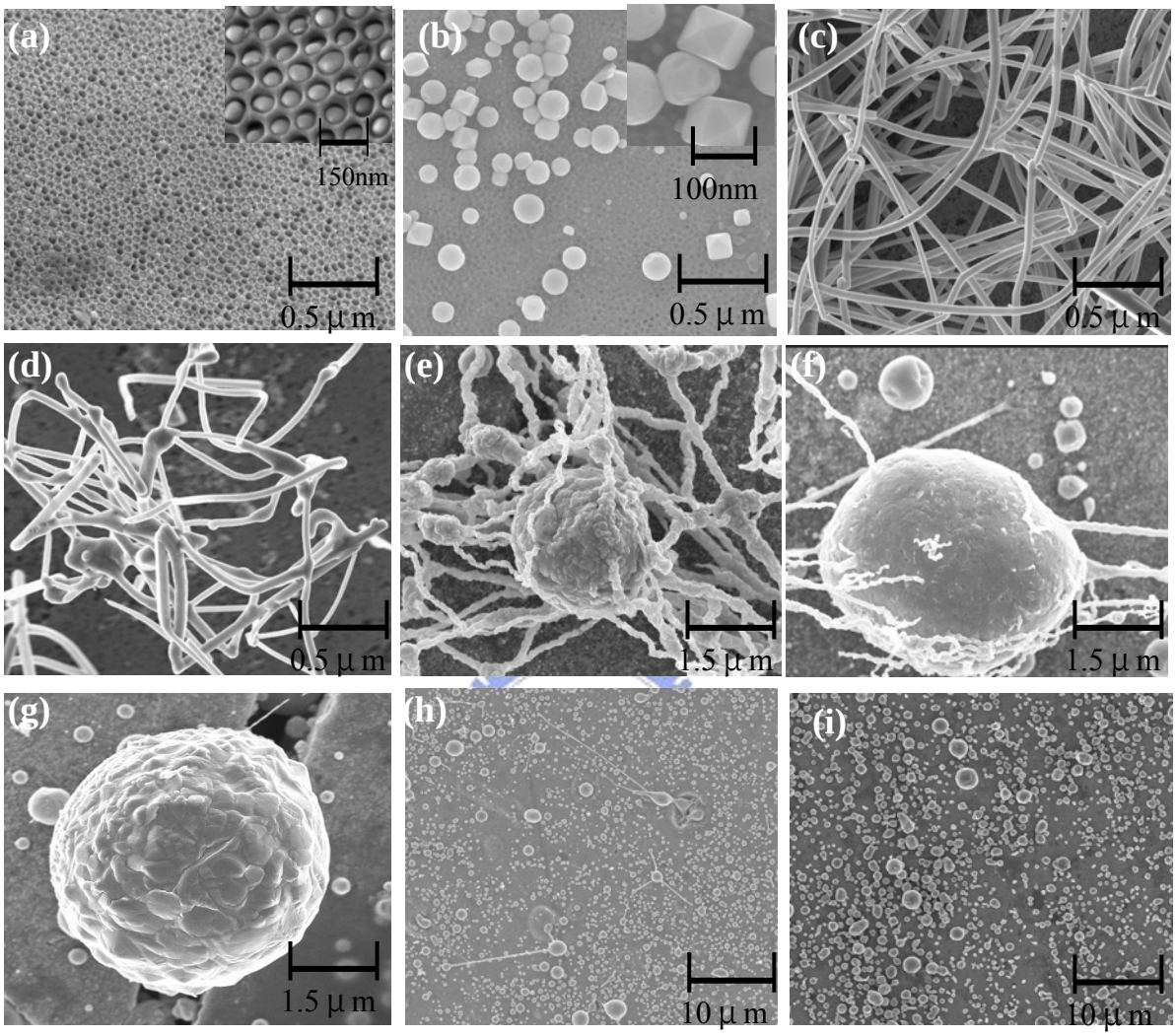


**Fig. 4.49** Sn whiskers and particle growth on 60nm diameter pore of AAO (with Sn inside) surface, heating up and cooling down by Differential Scanning Calorimetry (DSC); clean surface of AAO at 25$^{o}$C (a), nanocrystals forming at 220$^{o}$C (b), whiskers forming at 226$^{o}$C (c), whiskers agglomeration at 228$^{o}$C (d), whiskers agglomeration and forming a sphere at 229$^{o}$C (e), few whiskers connect to sphere at 230$^{o}$C (f), micro scale sphere forming at 231$^{o}$C (g), most spheres and few whiskers on the AAO (h), micron and sub-micro spheres on the AAO at 240$^{o}$C (i).

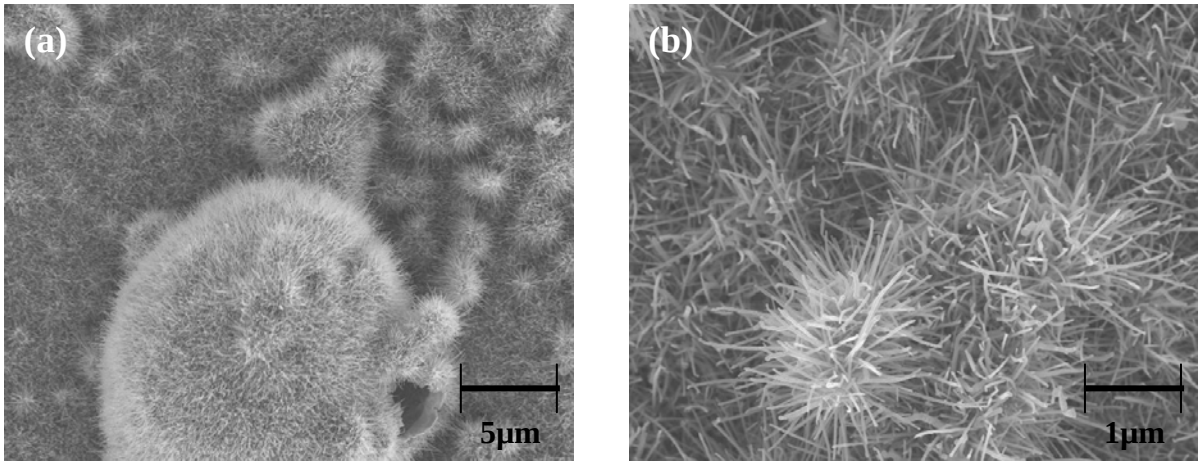


**Fig. 4.50** The SEM images of Sn nanowhiskers form on the AAO (a), and the high magnification image (b).

In Fig. 4.50, when the temperature is controlled at 226$^{o}$C a dense of Sn nanowhiskers form on the AAO (a). Also, from the high magnification image the whiskers have a uniform diameter in the nanoscale (b). Figure 4.51 shows when the temperature (227 $^{o}$C) was very close to the m.p. the nanowhisker tip start to form a nanosphere (a), the high magnification image shows as Fig. 4.51 (b). In the experimental process, when Sn melt was injected into AAO and solidify to Sn nanowires a high residual stress was kept in the template. As well as, thermal expansion is an others driving force for whiskers growth when the sample below and closes to Sn melting temperature. Sn has a high surface tension which is 0.544 N/m [113]. Also, the ultra-hydrophobic happen between Sn and AAO that the contacting angle between Sn and alumina (AAO) is $158^{0}$-$173^{0}$ [114]. Therefore, when the temperature is higher then the Sn melting point the Sn forms sphere on the whisker tip or on the AAO. In the above results, a driving force of residual stress and thermal expansion effect offer Sn whisker growth soon from inside of AAO. In summary, the driving force of a residue stress releases from the template during high temperature that make uniform size of Sn whiskers growth on the AAO in a few minutes. High heating and cooling rate, Sn trends to form a coarse whisker on the AAO. Nevertheless, low heating and cooling rate, Sn prefers to form a fine nanowhisker on the AAO. The high surface tension on Sn melt and high contacting angle between Sn melt and AAO that make Sn whisker easily forming sphere. When the temperature is higher than the m.p. of Sn nanowhisker the Sn

nanowhisker tip trend to forming nanosphere or agglomerate whiskers together and form sub-micron particle on the AAO.

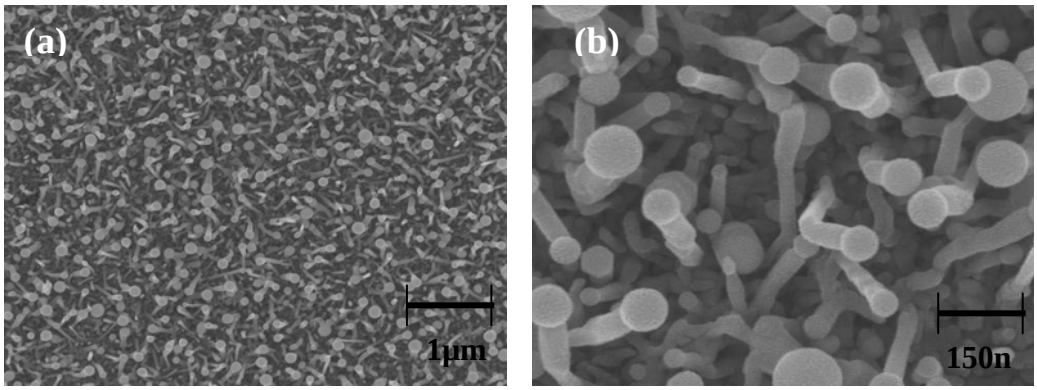


**Fig. 4.51** The SEM images of Sn nanosphere on the nanowhiskers (a), and the the high magnification image (b).

The experiment results from Choi [135], whisker growth the surface cannot be oxide free. Hence, only those metals that grow a protective oxide, such as Sn, are know to have hillock or whisker growth. Tin is an active metal which can easily reacts with oxygen to form oxides of SnO and $SnO_2$. The equilibrium partial pressure of oxygen between Sn and SnO can be estimated from thermodynamics calculation. The equilibrium equation of Sn to SnO can be written as,

$$Sn_{(s)} + \frac{1}{2}O_{2(g)} \rightarrow SnO_{(s)} \quad \text{.....(29)}$$

with a Gibbs free energy [136] of

$$\Delta G = -287.6 + 102T \ \ (kJ) \quad \text{.....(30)}$$

Furthermore, the relationship between $\Delta G_f$ and K is

$$\Delta G = -RT \ln K \quad \text{.....(31)}$$

in reaction (29), K can be expressed as:

$$K_{eq.} = \frac{a_{SnO_{(s)}}}{a_{Sn_{(s)}} \times (P_{O_{2(g)}})^{\frac{1}{2}}} \quad \text{.....(31)}$$

Accordingly, the partial pressure of oxygen can be expressed as,

$$\log P_{O_2} = -2 \log K \quad \text{.....(33)}$$

Therefore, $P_{O_2}$ in reaction (29) can be expressed as:

$$P_{O_2} = \exp(10.64 - \frac{30059}{T}) \quad \text{.....(34)}$$

As same calculation from SnO, the equilibrium equation of Sn to $SnO_2$ can be written as,

$$Sn_{(s)} + O_{2(g)} \rightarrow SnO_{2(s)} \quad \text{.....(35)}$$

$$\Delta G = -583.85 + 0.211T \ \ (kJ) \quad \text{.....(36)}$$

$$P'_{O_2} = \exp(11.04 - \frac{30493}{T}) \quad \text{.....(37)}$$

where $\Delta G$ is the Gibbs free energy (J/mole); K is the equilibrium constant; a is activity, R is the gas constant (8.314 J/mole); T is the temperature ($^oK$), $P_{O_2}$ is equilibrium partial oxygen pressure between Sn and SnO, $P'_{O_2}$ is equilibrium partial oxygen pressure between Sn and $SnO_2$. From Eqns. (34) and (37), The curves of equilibrium partial oxigen pressure in Sn-SnO and Sn-$SnO_2$ can be drawn as Fig. 4.52(a); as well as, the Gibbs free energy curve of $SnO_2$ is lower than SnO, showed as Fig. 4.52(b). In above calculation, SnO and $SnO_2$ film can form in a low partial

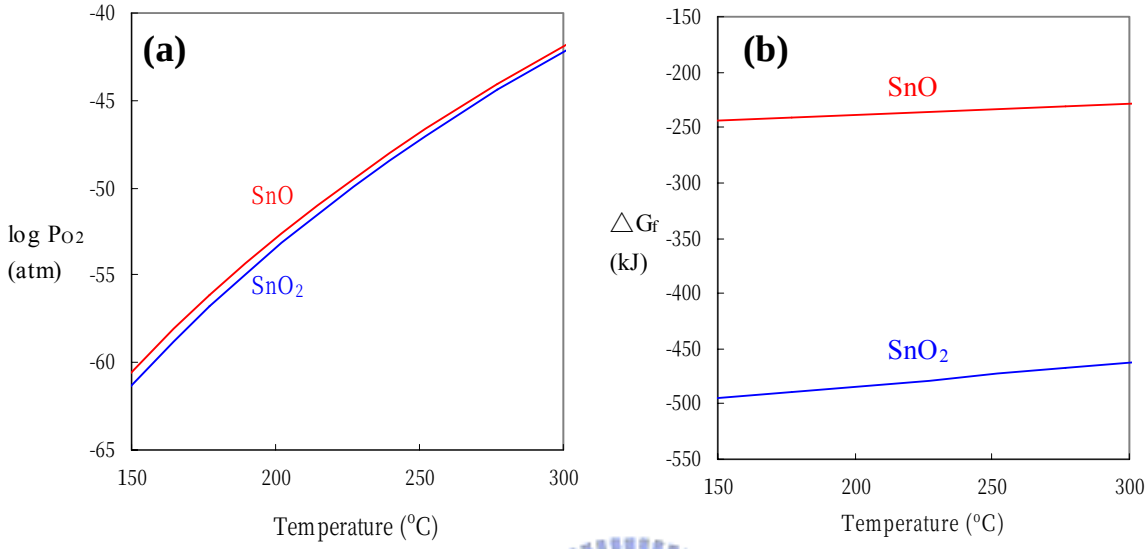


**Fig. 4.52** The Equilibrium curves of partial oxygen pressure (a) and Gibbs free energy (b) between 150 °C to 300°C in Sn-SnO and Sn-$SnO_2$ system.

oxigen pressure; as well as, $SnO_2$ is stable than SnO film. This results may explain a thin $SnO_2$ film covers on the Sn whiskers even when the whisker forms from the ultra-high vacuum chamber.

### 4.5.3 Formation of Sn nanospheres on AAO

Since Sn has high surface tension and AAO has nanoscale roughness (pillars and pores; as show in Fig. 453) on its surface, Sn nanospheres are easily formed on the AAO surface. When the partial Sn melted out from the AAO channels, the melt particles solidified on the AAO surface. In our experiment, AAO with Sn was reheated to 3°C (235°C) above the Sn melting point for 30 seconds in a vacuum ($10^{-3}$ Torr) chamber. We then quenched the chamber to a low temperature (8°C). The rapid solidification of melt on the AAO surface caused a real sphere to form quickly; furthermore, the contact angle between a sphere and AAO was larger than 120°, as shown in Fig. 4.54. The linear thermal expansion of a metal can be estimated by $l_t = l_0(1 + \alpha \times t)$ [116], where $l_0$ is the length at 273 K (0 °C), α is the coefficient of linear thermal expansion, and the length at temperature t is $l_t$; in this experiment, $\alpha = 22 \times 10^{-6}$/K [117].

In our work, we obtained a Sn wire of 10μm length and 60 nm diameter in the AAO. After reheating to 235 °C, the thermal expansion ratio is 11.176%, which can be estimated by the thermal expansion equation, and the expansion volume of the melt coming out is 315833 $nm^3$. The melt would form an 84.5 nm diameter ball during solidification. However, since the distance of cell wall of the AAO is shorter (15 nm) than the pore diameter (60 nm), two or more balls can easily agglomerate. Figure 4.55 shows that the ball diameters varied between 90 to 300 nm on the AAO surface. The quantitative size distribution of nanospheres is shown in Fig. 4.56. The melting point of Sn nanowires and nanospheres

were detected using a differential scanning calorimeter (DSC). The melting point of bulk Sn was found to be 231.91°C. However, for the Sn nanowire and the AAO composite, two endothermic peaks can be detected, as shown in Fig. 4.57. It is believed that the first peak at 227.15 °C (60nm diameter nanowire) represents the outflux Sn from the AAO to form Sn nanospheres. The second peak noted at 231.91°C (bulk) is believed to be the melting temperature of the remaining Sn nanowires in the AAO.

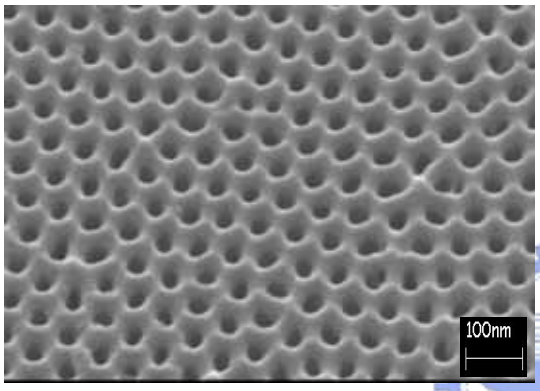


**Fig. 4.53** SEM image of AAO template with nanoscale roughness of nanopillars and nanopores.

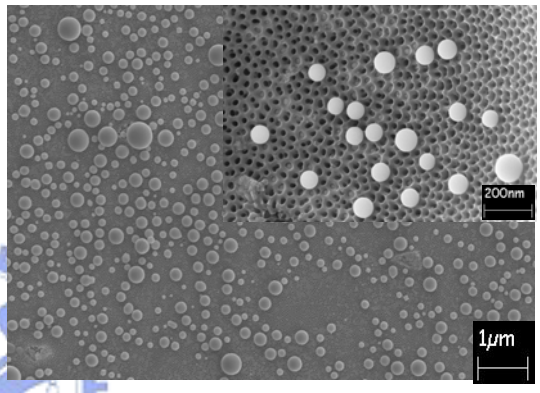


**Fig. 4.54** The SEM images of rapid solidification of Sn nanospheres on the AAO surface.

The contact angle of less than 90° between a liquid and solid surface is called hydrophilic, that equal to 120° is called hydrophobic, and that larger than 120° is called ultra-hydrophobic. Since Sn has high surface tension and rapidly solidifies on the nanostructure surface of AAO, contact angle between a sphere and AAO is larger than 120°. It is easy to the remove spheres from the AAO surface by vibration while AAO with spheres is submerged in liquid, as shown in Fig. 4.58. The crystal structure of Sn nanosphere is single crystal with tetragonal of [101] zone axis, the

TEM image and diffraction pattern showed as Fig. 4.59(a) and Fig. 4.59(b). Figure 4.60 shows that the surface of the AAO specimen was clean and without any nanospheres after AAO with Sn nanosphere was vibrated in alcohol. The high-magnification image in Fig. 4.60 also shows how the melt flowed out left spaces empty on the AAO surface.

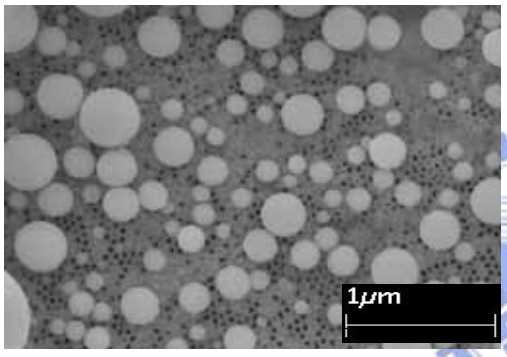


**Fig. 4.55** The SEM image of Sn nanospheres with diameter between 90 and 300 nm.

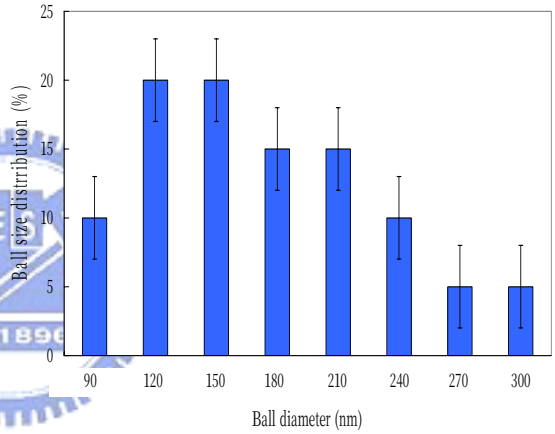


**Fig. 4.56** Histogram showing the quantitative size distribution of nanospheres.

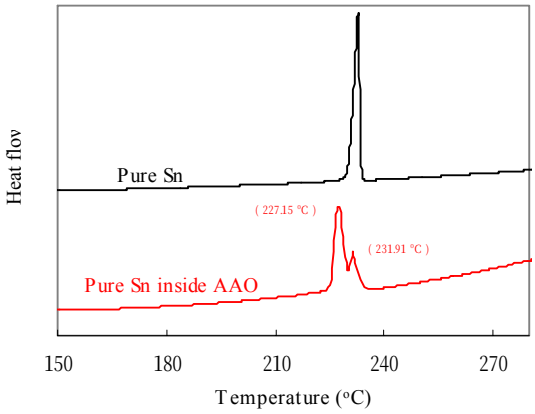


**Fig. 4.57** DSC curves showing the melting points of pure Sn and the Sn nanosphere to be 231.91°C and 227.15°C, respectively.

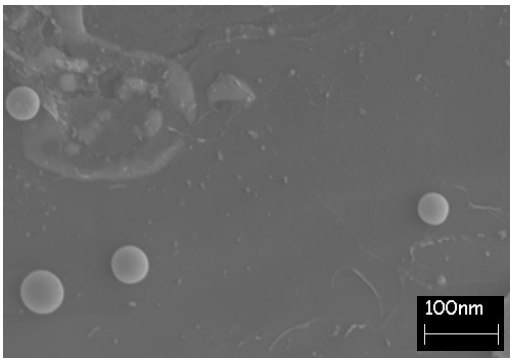


**Fig. 4.58** SEM image of Sn nanospheres collected by vibrate in alcohol.

### 4.5.4 Effect of superheating and cooling rate on nanosphere formation

Since particle size is dependent on the temperature and cooling rate, low superheating and high quenching rates tend to result in small particles; on the contrary, high superheating and low quenching rates and long heat treatment promotes make particle growth and sintering. Figure 4.61 shows the case of a high superheating temperature (300°C) and a low quenching temperature (0°C) of the specimen. The diameter of the ball (450 nm) is much larger than the AAO pore size. Additionally, this is not enough time for the particle to form a ball due to thermal creaking. Therefore a defect-free nanosphere could not be formed, but instead a creaked and a large particle forming. Figure 4.62 shows that the balls tend to form idea spheres, but are sintered together; this is a case of suitable quenching temperature (5°C), and high superheating temperature (300 °C).

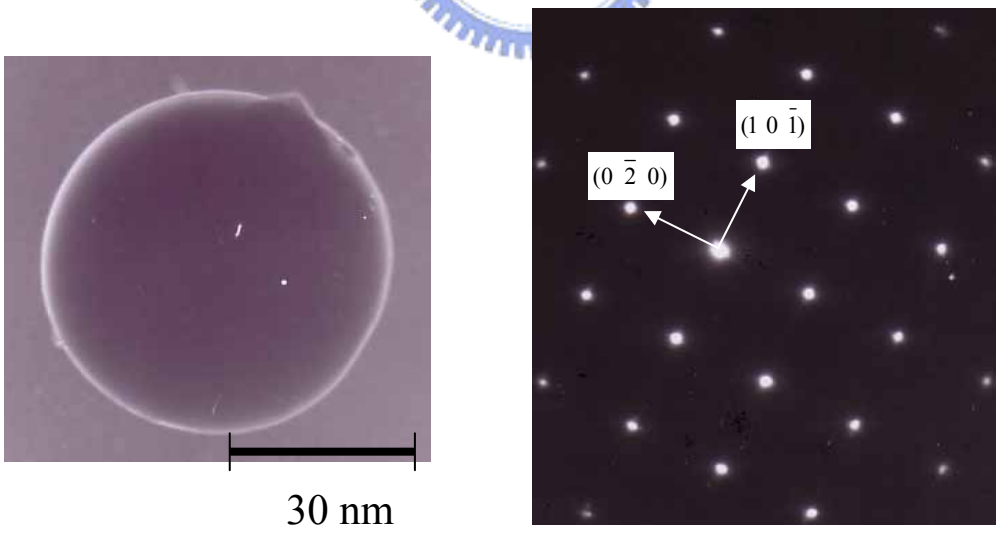


**Fig. 4.59** TEM image of Sn nanosphere (a), and diffraction pattern with tetragonal crystal structure of [101] zone axis (b).

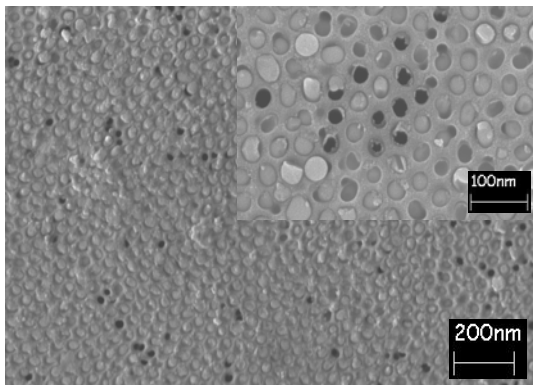


**Fig. 4.60** SEM images showing the AAO surface without any Sn sphere after Sn nanospheres were collected by vibrate, as well as remaining shallow concave wells on the AAO surface.

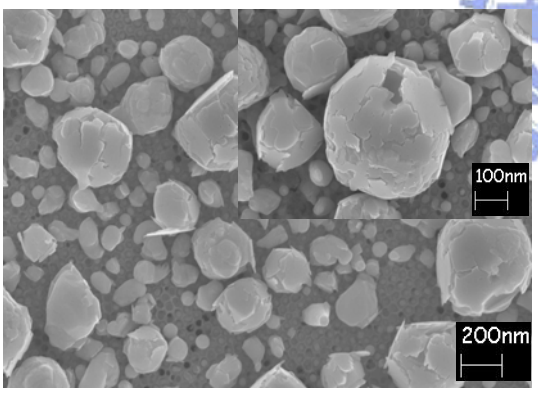


**Fig.4.61** SEM images showing Sn balls cracked under a fast quenching rate (235$^{o}$C to 0$^{o}$C).

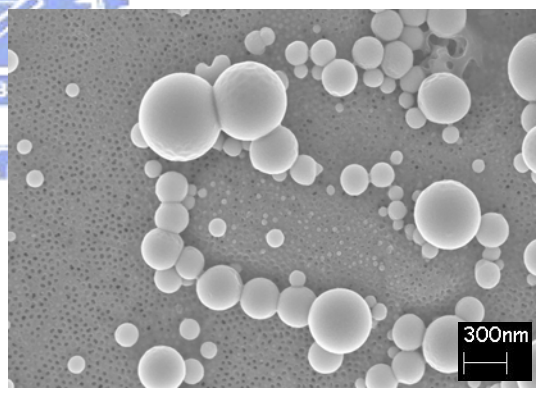


**Fig. 4.62** SEM images showing Sn balls sintered together under the high temperature (300$^{o}$C).

## 4.6 Alloy nanowires and nanoparticles

### 4.6.1 Nanoparticles forming by thermal immersing method

AAO with large surface and uniform pore size was used as a template for nucleating and growing metal nanoparticles. The diameter and interval of the uniform nanochannels on the AAO were typically 60 and 40 nm, respectively. Both the template and bulk alloy (Pb-Bi) were vacuumed to $10^{-6}$ torr and sealed in the glass tube. When the sample was heated up to the alloy melting temperature (398K) at 473K for 10 min, the molten alloy did not fill the pores of the AAO, but formed a drop of melt on the AAO surface (see Fig. 4.63 Since Pb-Bi is an active metal which reacts with oxygen easily, the equilibrium partial pressure of oxygen between Bi and $Bi_2O_3$ is $10^{-38.7}$ atm, and that between Pb and $Pb_3O_4$ is $10^{-33.9}$ atm at 473K under $10^{-6}$ torr [120].

This is because some oxygen remained in the vacuum tube even after argon purging and turbo pump vacuuming. Hence, a thin oxide film forms between the interface of the Pb-Bi melt and AAO. Therefore, nanoparticles can not be formed when the oxide film exists at the melt-AAO interface, as shown in the schematic diagram in Fig. 64(a), and restricts Pb-Bi nucleation on AAO, as shown in Fig. 4.64(b). However, the density of Pb-Bi oxide is less than Pb-Bi eutectic (10.45 g/cm$^3$). The oxide film at the melt-AAO interface floats to the top of the melt after heat treatment (2 hr), and the Pb-Bi melt nucleated in the pores of AAO when the melt solidifies, as shown in the schematic diagrams in Fig. 4.65(a) and Fig. 65(b). Figure 74 shows an SEM image of the specimen after heat treatment for 2 hr at

473K, in which nanoparticles can be observed.

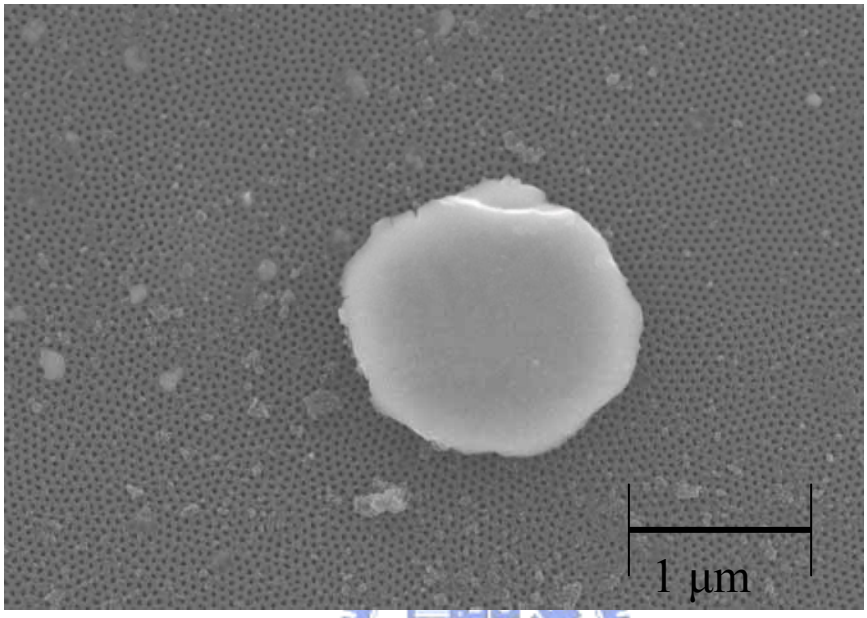


**Fig. 4.63** Molten metal became cohered and covered AAO when heat treatment time was insufficient, so that nanoparticles had difficulty forming on AAO.

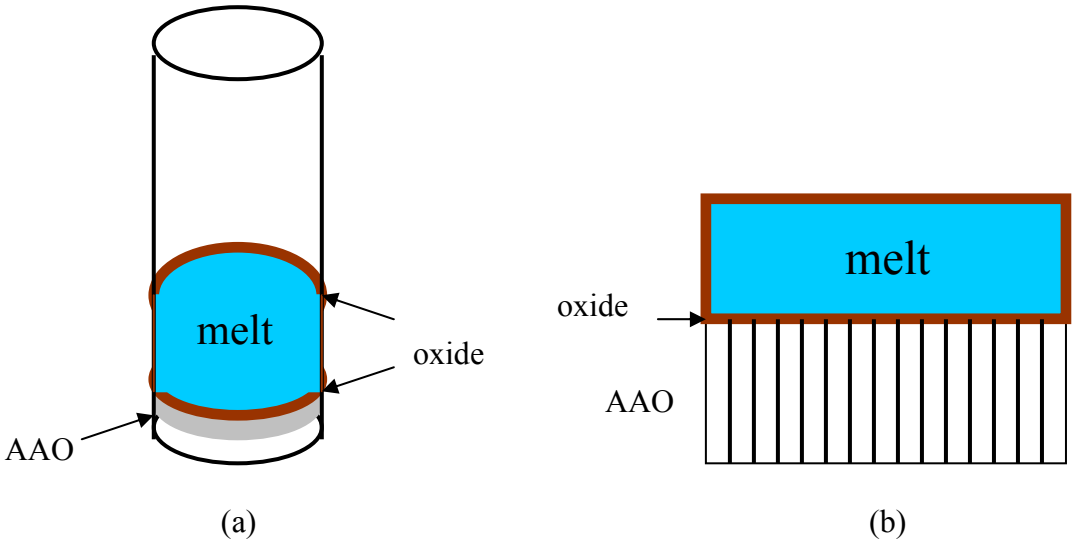


**Fig. 4.64** Schematic diagrams show oxide film existence between melt and AAO, which difficully in nanoparticle formation on AAO; (a) that macro schematic of oxide film covered on surface of melt, (b) micro schematic of oxide film that prevented melt nucleation on the AAO.

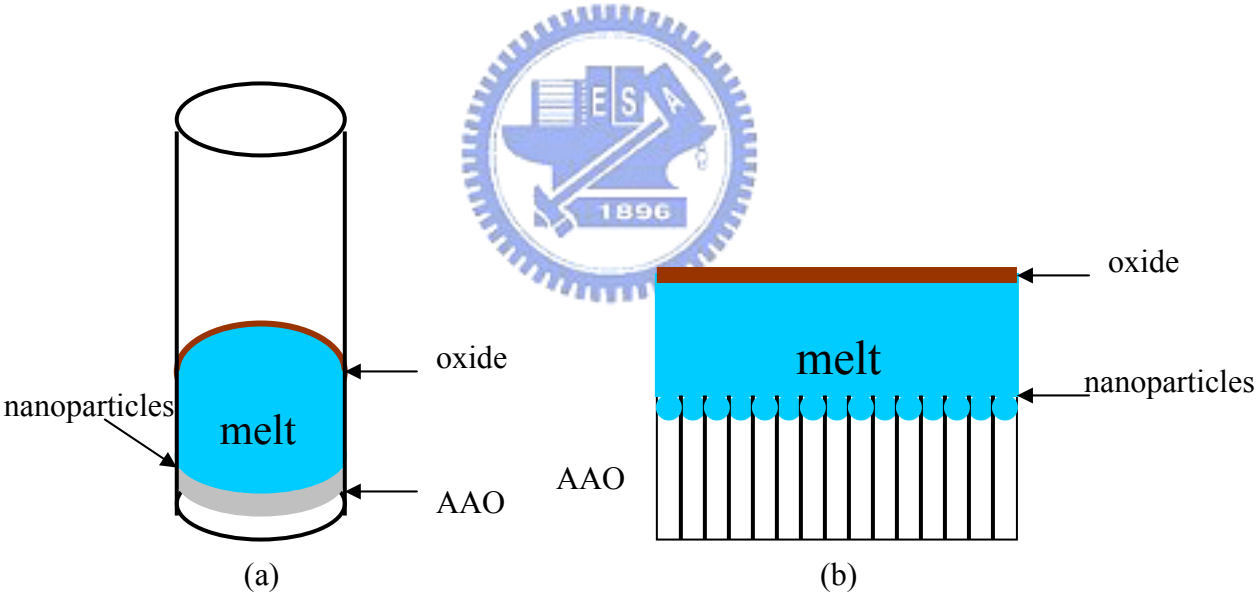


**Fig. 4.65** Schematic diagrams showing free oxide on interface of melt-AAO, the nanoparticles formed on AAO; (a) macro schematic of free oxide film on interface of AAO-melt, (b) micro schematic of melt nucleated on AAO.

### 4.6.2 Critical radius and free energy of alloy nucleation on the AAO

The solid begins to form in very small regions throughout the bulk of the liquid. These small regions are called nuclei and are considered to be

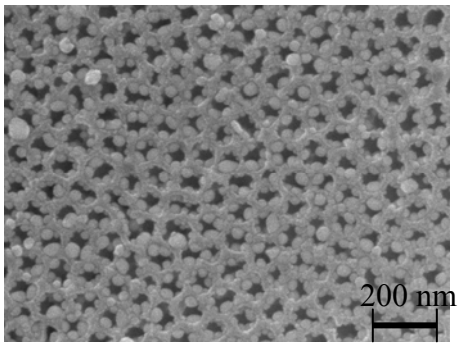


**Fig. 4.66** SEM image showing that melt solidified and nucleated to form nanoparticles on AAO.

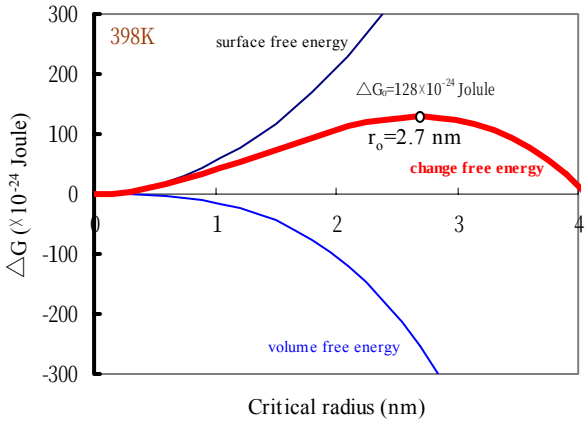


**Fig. 4.67** Homogeneous nucleation of critical radius and Gibbs free energy of Pb-Bi eutectic are 2.7 nm and 128× $10^{-24}$ joule at 398 K.

very small spherical in shape. Consequently, their surface-to-volume ratio is very high. Since there will be a positive free energy associated with the formation of the surface area of the nuclei, this surface energy will act as a barrier to the formation of small nuclei. The free-energy change to form a nucleus [119] is given by:

$$\Delta G_{(hom)} = 4\pi r^3 \Delta G_v/3V_l + 4\pi r^2 \gamma \quad \ldots(38)$$

Here, $\Delta G_{(hom)}$ is homogeneous sphericity formation energy change, ($4\pi r^3$

$\Delta G_v/3V_l$) is molar volume free energy, ($4\pi r^2 \gamma$) is surface free energy, r is radius, $\Delta G_v$ is change volume free-energy, $V_l$ is molar volume, and $\gamma$ is surface tension. In the Eqn. (38), the curve of $\Delta G_{(hom)}$ with r is a parabolic curve, and the saddle point of the curve is $\partial \Delta G_{(hom)} / \partial r = 0$, therefore, at the saddle point the Eqn. (38) can be written as:

$$\frac{\partial \Delta G_{(hom)}}{\partial r} = 0 = 4\pi r_o^2 \frac{\Delta G_v}{V_l} + 8\pi r_o \gamma \quad \ldots(39)$$

The critical radius of the solid nucleus of $r_o$, and the free energy $\Delta G_{o,(hom)}$ are:

$$r_o = -2\gamma \frac{v_l}{\Delta G_l} \quad \ldots\ldots\ldots\ldots\ldots\ldots\ldots\ldots(40)$$

$$\Delta G_{o,(hom)} = 16\pi \gamma^3 . \ V_l / \Delta G_v \ldots\ldots\ldots (41)$$

Since the melting point of Pb-Bi is 125 $^oC$, the molar volume of Pb-Bi eutectic can be calculated by $V_{l,Pb\text{-}Bi} = V_{l,Pb} . \ X_{Pb} + V_{l,Bi} . \ X_{Bi}$, surface tension can be calculated by $\gamma_{Pb\text{-}Bi} = \gamma_{Pb} . \ X_{Pb} + \gamma_{Bi} . \ X_{Bi}$ as well as, volume free energy $\Delta G_{v,Pb\text{-}Bi} = \Delta G_{v,Pb} . \ X_{Pb} + \Delta G_{v,Bi} . \ X_{Bi}$, where $X_{Pb}$ and $X_{Bi}$ are the molar fractions, $V_{Pb}$ and $V_{Bi}$ are the molar volumes, $\gamma_{Pb}$ and $\gamma_{Bi}$ are the surface tensions, and $\Delta G_{v,Pb}$ and $\Delta G_{v,Bi}$ are the volume free energies of Pb and Bi, respectively. Here, $X_{Pb}$=0.442, $X_{Bi}$=0.558, $\gamma_{Pb}$= 468(dyne/cm), $\gamma_{Bi}$= 378(dyne/cm), $V_{l,Pb}$=18.26($cm^3$/mole) ,$V_{l,Bi}$=21.31($cm^3$/mole), $\Delta G_{v,Bi}$=-9.94(kJ/mole), and $\Delta G_{v,Pb}$ =-15.83(kJ/mole) [120]. Therefore, the

surface tensions, molar volumes, and volume free energies of Pb-Bi eutectic at the melting point can be calculated as: $\gamma_{Pb\text{-}Bi}$=417.78 (dyne/cm), $V_{l,Pb\text{-}Bi}$=19.96($cm^3$/mole), and $\Delta G_{v,\ Pb\text{-}Bi}$=-12.54(kJ/mole), respectively. On the basis of the thermodynamic data, the critical radius and change free-energy can be calculated as 2.7 nm, and 128×$10^{-24}$ joule, respectively, as shown in Fig. 4.67.

When the surface has a bulge that resembles a spherical cap, atoms easily to nucleate on the bulge. Therefore, heterogeneous nucleation is easier than homogeneous nucleation. Eqn. 42 show the relationship between $\Delta G_{(het)}$ and $\Delta G_{(hom)}$, where $\Delta G_{(het)}$ is the heterogeneous sphericity formation energy change [121], and $\delta$ is the angle between the bulge and molten metal.

$$\Delta G_{(het)} = \Delta G_{(hom)} [(2-3\cos\delta + (\cos\delta)^3)/4] \quad \ldots (42)$$

$\Delta G_{(het)} < \Delta G_{(hom)}$, which shows that less energy is required for heterogeneous nucleation and consequently its critical radius of nucleolus is smaller than that for homogeneous nucleation. Since there were a lot of bulges on the AAO surface when aluminum was anodized, the Pb-Bi eutectic nucleation on AAO is considered heterogeneous sphericity formation. Therefore, the critical radius of Pb-Bi eutectic on AAO was smaller than the homogenous critical radius of 2.7 nm.

### 4.6.3 Nanoparticle in concave

There are few concave defects on the AAO surface that occurred after electro-polishing but before anodizing of Al. Heat flow into a concave is convergent, and heat transmission is lower in a concave than on the surface. A concave on the AAO surface offers a suitable surrounding for nanoparticle growing. Therefore, the diameter of nanoparticles in a concave was much larger thanthat of nanoparticles on the surface, as shown in Fig 4.68. The different concave morphologies also cause the various quantities and sizes of nanoparticles. Figure 4.69(a) shows that the diameters of nanoparticles on the pore walls of a concave were bigger than on the surface of AAO. The

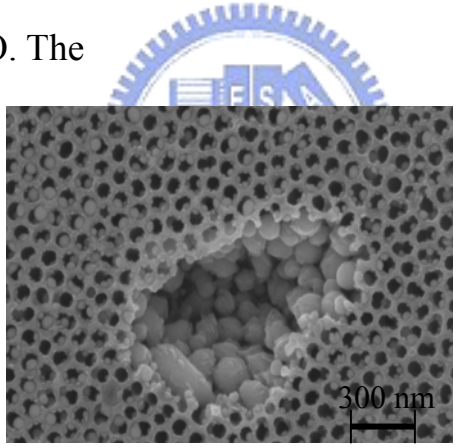


**Fig. 4.68** Nanoparticle size in a concave was much larger than that on surface of AAO.

figure also shows a few big nanoparticles forming on the bottom of the concave where is AAO free, but shallow of pattern pores on the aluminum substrate. Figure 4.69(b) shows a smooth and shallow indent, the number and the size of nanoparticles inside were similar to those on the surface of AAO. The relationship between the number and diameter of nanoparticles

was dependent on nanoparticle nucleation and growth. When the rate of nucleation was faster than that of growth, a large number of small nanoparticles formed; on the contrary, when nucleation was slower than grow a small number of large nanoparticles formed. Figure 4.69(c), shows a large number of nanoparticles formed in a deep and rough concave. Figure 4.69(d) shows a small number of large nanoparticles formed in a deeper concave than that of Fig. 4.69(c). Because of a high contact angle between the Pb-Bi nanoparticles and AAO surface (near 106$^{o}$) [104], it is easy to remove particles from the AAO surface by ultrasound during AAO with particles in liquid as showed in Fig. 4.70.

### 4.6.4 Nanoparticles growth and sintering

AAO has a honeycomb structure whose pore wall area is W×L, and pore radius is R, as shown in Fig. 4.71. Each of hexagonal pore offers six suitable positions for nanoparticle nucleation. Therefore, a semi-cup concave with the radius $R_1$ on AAO offers Q positions for nanoparticle nucleation and isolation on the corners of AAO.

$$Q=6\times(2\pi R_1^2/(\pi R^2+0.5LW)\ldots(43)$$

Assume the maximum radius $R_2$ of the initially isolated nanoparticle is (2/3)R, so the volume $V_2$ of each initially isolated nanoparticle is $4\pi R^3/3$. The surface energy of small particle is higher than large particle. So, when the melt solidifies, the driving force of latent heat can sinter the six isolated small nanoparticles into a large ball on the pore of AAO. Therefore, the radius $R_3$ of the large ball is

$$R_3=(9V_2/2\pi)^{(1/3)}\ \ldots\ (44)$$

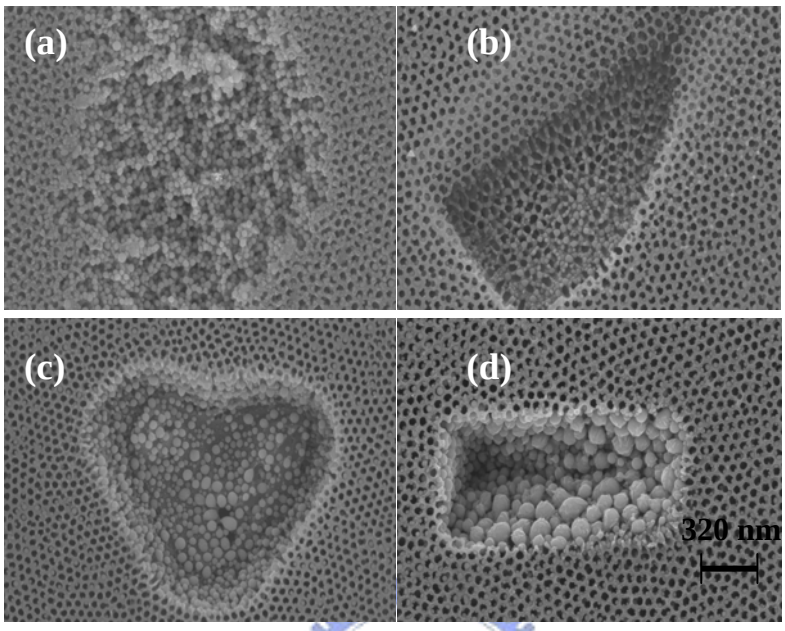


**Fig. 4.69** Various numbers and sizes of nanoparticles in concaves; (a) diameters of nanoparticles on pore wall of concave were larger than those on surface of AAO, (b) a smooth and shallow indent, numbers and the size of nanoparticles inside were similar to those on surface of AAO, (c) large number of nanoparticles formed in deep and rough concave, (d) small number of large nanoparticles formed in deep concave.

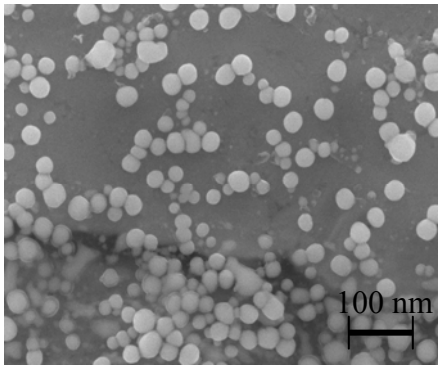


**Fig. 4.70** SEM image of nanoparticles subjected to ultrasound.

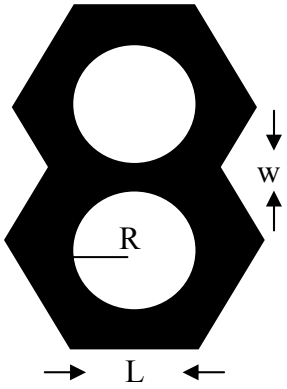


**Fig. 4.71** Schematic diagrams of AAO with pore radius and pore wall width denoted R, W, and L, respectively.

Figure 4.72(a) shows the radius of the semi-cup concave to be 2.5 μm, and W, L, R to be 16 nm, 70 nm, 30 nm, respectively. Therefore, from Eqn. (43), Q= 69440 pore positions for nanoparticle nucleation. Figure 4.80(b) is a high magnification image of Fig. 4.72(a), the image shows the initially isolated nanoparticle, and the parts of the large sintered ball formed on AAO. $R_2$ was 40 nm, and $R_3$ was 72.5 nm, calculated using Eqn. (44). Figure 73 shows nanoparticles in a deeper concave than that of Fig. 4.72, where, the diameters of the nanoparticles exceed the pore size of AAO due to sintering.

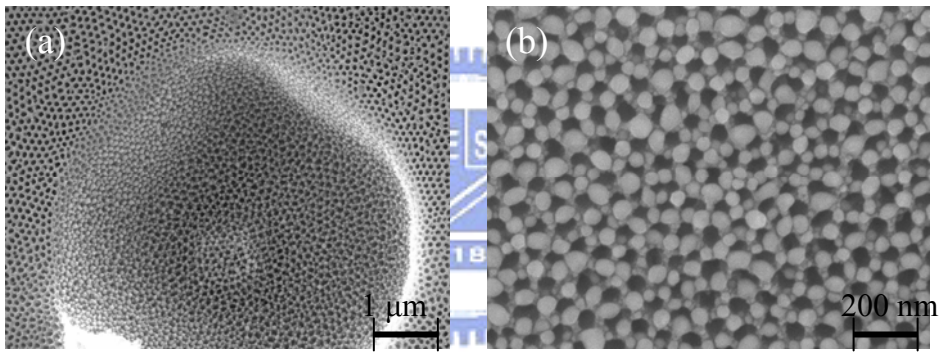


**Fig. 4.72** Nanoparticles in smooth concave; (a) diameter and number of nanoparticles in concave were similar to those of nanoparticles on AAO surface, (b) high magnification image, initially isolated nanoparticle, and parts of large sintered ball formed.

If the diameter of a concave is constant, a deeper concave has a larger surface area of positions for nanoparticles nucleation and a more latent heat than a shallow concave when the nanoparticles solidify. A schematic diagram of the surface area with concaves of various depths was shown in Fig. 4.74.

The depth and surface area can be expressed using Eqns. (42), and (45).

$$h = R(1-\cos\theta) \quad \ldots\ldots (45)$$

$$A = 4 \times \pi \theta h^2 / 180 \quad \ldots (46)$$

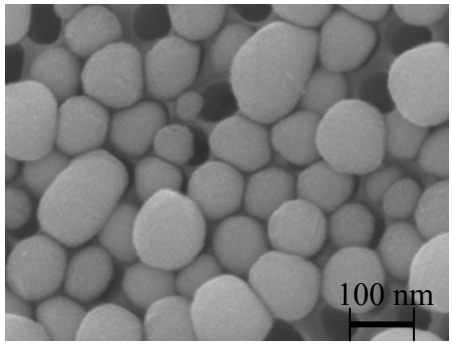


**Fig. 4.73** SEM image of sintered nanoparticles in deep concave.

Here, h is the depth, θ the angle of a half curvature of a concave, and A the surface area. Assuming a concave with a 5 μm diameter, the latent heat at various depths can be calculated using Eqns. (43), (45), and (46), shown in Fig. 4.75. A depth concave has a larger surface area for nanoparticle formation and a lower heat transmission of latent heat loss than a plane surface. Therefore, nanoparticles were bigger in a concave than on a plane surface. In the above results, the AAO pore diameter was 60 nm, the critical radius of Pb-Bi eutectic heterogeneous nucleation on AAO as estimated using the Eqn. (41) was less than 2.7 nm (Fig. 4.76 (a)). When the nucleus grows, the maximum diameter of the isolated nanoparticles is 40 nm (Fig. 4.76 (b)), and the six isolated nanoparticles assemble to form a large nanoparticle whose diameter is 72.5 nm (Fig. 4.76(c)).

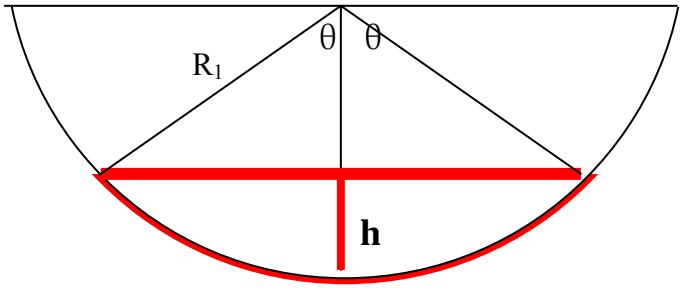


**Fig. 4.74** Schematic diagram of surface area with various dept of concave.

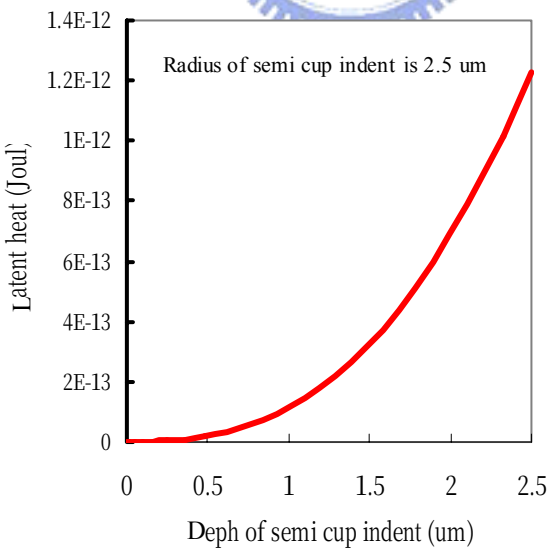


**Fig. 4.75** Latent heat in the concave of AAO increased with depth of semi-cup indent.

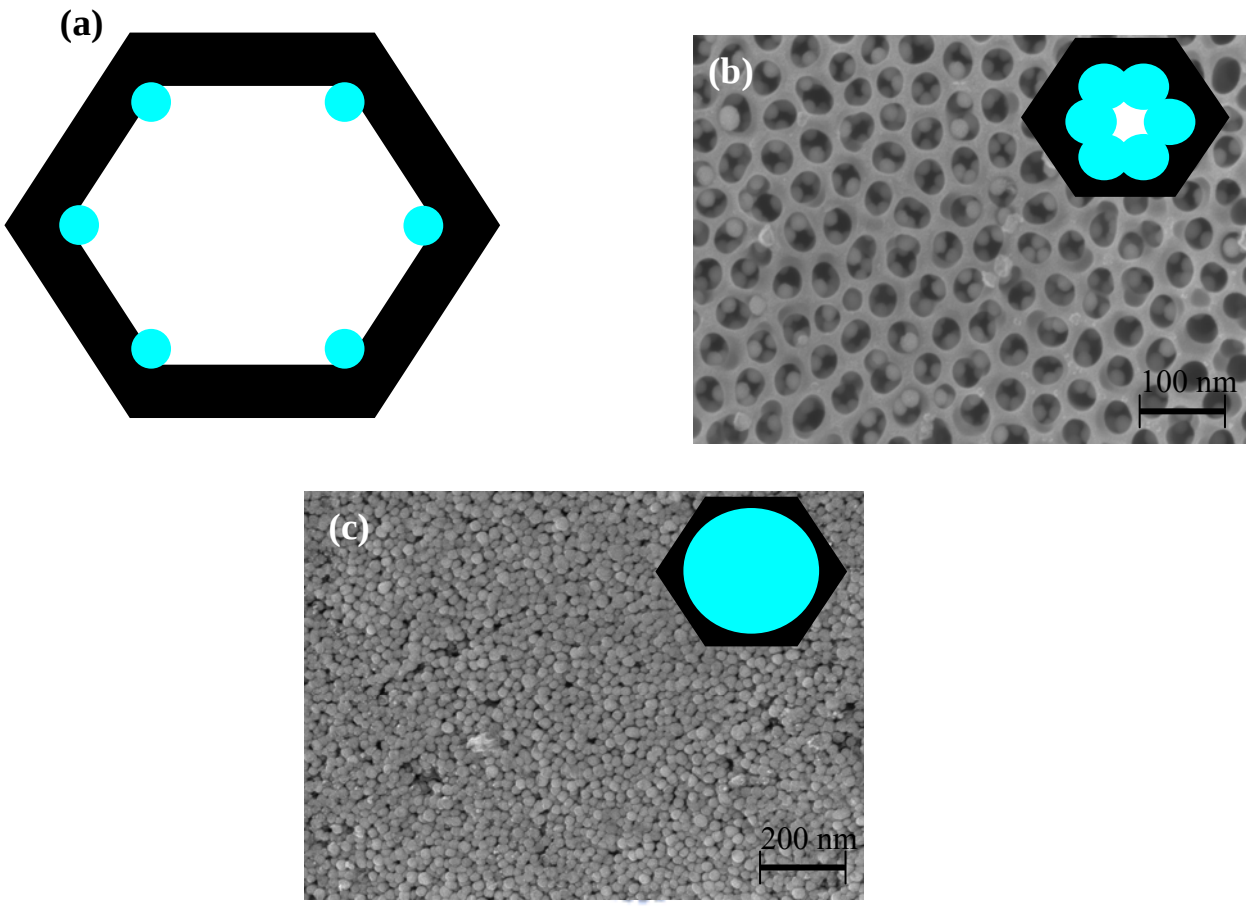


**Fig. 4.76** SEM and schematic diagrams of nanoparticles nucleated on the corners of AAO and grown on pore of AAO; (a) nanoparticles nucleated on six nooks of AAO, (b) six isolated nanoparticles grew, (c) six nanoparticles assemble to form a large nanoparticle.

# Chapter 5 Conclusions

The template of AAO was fabricated used anodization but follows a route different from the commonly known 1- or 2-step anodization. General- purity (99.7%) commercial aluminum was used instead of the high-purity (99.999%) aluminum required in conventional anodization. The current hydraulic pressure injection process is a simple, quick, high yield and cost-effective nanowire fabrication process compared to the gas pressure injection process as well as any of the ion-deposition methods mentioned above. The resulting nanowires are also good quality with good control of diameter uniformity and length. Based on the sample of the nanowires inside the AAO, the nanospheres form when the heating temperature was little higher than the nanowires melting. Otherwise, the nanocrystals and nanowhiskers form when the heating temperature is below the nanowires melting temperature. The brief results of our study can be concluded as:

1. The template of AAO was fabricated used General- purity (99.7%) commercial aluminum foil by 1- step anodization.

2. The pore diameter of AAO can be controlled from 8nm to 180nm in our process.

3. 15nm, 60nm, and 180nm diameter of Sn nanowires were fabricated in the AAO template.

4. The filling ratio of nanowires in AAO was improved to more than 98%.

5. A single Sn nanowire was collected and its crystal structure which is single crystal structure was observed by TEM.

6. Through the various heat treatment the nanowires could change to nanospheres and nanowhiskers

# Chapter 6 Future works

1. Study the critical diameter of Sn nanowire from single- crystal to poly-crystal when Sn melt solidified in the AAO tube.

2. To test the electronic characteristic of single Sn nanowire.

3. Fabrication of high temperature ( >600$^{o}$C ) nanowires in AAO by the hydraulic force injection process.

4. Study the crystal structure of alloy nanowires by TEM.

5. Using nanowires to make a device.

# References


[1] C. P. Collier, R. J. Saykally, Science, 277 (1997) 26.

[2] I. Okur, P. D. Townsend, Nucl. Instr and Meth in Phys Res. B, 148 (1999) 1069.

[3] J. G. Lee, H. Mori, Phys Rev. B, 65 (2002) 1.

[4] S. Sun, C. B. Murray, Science, 287 (2000) 198.

[5] A. Moroz, Phys. Rev. Lett., 83 (1999) 5274.

[6] A. M. Morals and C. M.Lieber, Science, 279 (1998) 208.

[7] D. M. Hartmann and M. Heller, J. Mater. Res., 17 (2000) 473.

[8] S. Iijima, Nature, 354 (1991) 56.

[9] A. M. Morales, C. M. Leiber, Science, 279 (1998) 208.

[10] F. Burmeister, C. Schaffe, Adv. Mater., 10 (1998) 495.

[11] R. Notzel, Semicond. Sci. Technol., 11 (1996) 1365.

[12] O. Jessensky, F. Muller, Applied Physics Letters, 72, (1998) 1173.

[13] G. E. Thompson, G. C. Wood, Nature, 290 (1981) 230.

[14] H. Masuda, Masata Yotsuya, Appl. Phys. Letts., 78 (2001) 826.

[15] D. Routkevitch, T. Bigioni, J. Phys Chem., 100 (1996) 4037.

[16] Ying, United States Patent, Patent No. : 6231744 (2001).

[17] Y. Wu, Hannes Kid, Science, 292 (2001) 1897.

[18] C. A. Huber, T. E. Huber, Science, 263 (1994) 800.

[19] T. M. Whitney, J. S. Jiang, Science, 261 (1993) 1316.

[20] Y. Lei, L. D. Zhang, Appl. Phys. Letts., 78 (2001) 1125.

[21] K. Nielsch, R. B. Wehrspohn, Appl. Phys. Letts., 79 (2001) 1360.

[22] K. Kevin, Rueckes, United States Patent, Patent No.: WO0103208,

(2001).

[23] Y. Yang, Huilan Chen, Solid State Communications, 123 (2002) 279.

[24] S. W. Lu, U Sohling, M. Mennig, H. Schmidt, Nanotechnology, 13 (2002) 669.

[25] M. J. Fernee, J. Warner, A. Watt, Nanotechnology, 15 (2004) 16.

[26] M. Nath, A. Choudhury, Adv. Mater., 15 (2003) 2098.

[27] R. Ozao, M. Ochiai, Thermochemica Acta, 352 (2000) 91.

[28] Z. Zhang, Xiangzhong Sun, Phys. Rev. B, 61 (2000) 4850.

[29] Baolin Wang, Shuangye Yin, Phys. Rev. Letts., 86 (2001) 2046.

[30] D. N. Davydov, P. A. Sattari, J. Appl. Phys., 86 (1999) 3983.

[31] G. J. Strijkers, J. H. J. Dalderop, J. Appl. Phys., 86 (1999) 5141.

[32] D. Routkevitch, A. A. Tager, IEEE Transactions on Elecron Devices, 43 (1996) 1646.

[33] S. M. York, F. M. Leibsle, Appl. Phys. Letts., 78 (2001) 2763.

[34] T. Kyotani, Weihua Xu, Journal of Membrane Science, 196 (2002) 231.

[35] K. Shimizu, H. Habazaki, Electrochemica Acta, 47 (2002) 1225.

[36] G. S. Cheng, S. H. Chen, Materials Science and Engineering, A286 (2000) 165.

[37] K. Shimizu, H. Habazaki, Electrochemica Acta, 46 (2001) 4379.

[38] Vadim V. Yuzhakov, Hsueh Chia Chang, Phys. Rev. B, 56 (1997) 12608.

[39] Y. Peng, Dong Huan Qin, Materials Science and Engineering, B77 (2000) 249.

[40] Z. Zhang, Jackie Y. Ying, J. Maters. Res., 13 (1998) 1745.

[41] F. Burmeister, C. Schafle: Adv., Mater., 10 (1998) 495.

[42] S. Y. Chou, P. R. Krauess: J. Appl. Phys., 79 (1996) 6101.

[43] S. Y. Chou, P. R. Krauess: Scr. Metall. Mater., 33 (1995) 1537.

[44] G. E. Thompson, R. C. Furneaux: Corrosion Sci., **10** (1978) 481.

[45] G. E. Thompson, G. C. Wood: Nature, **290** (1981) 230.

[46] K. Ebihara, H. Takahashi: J. Met. Finish. Soc. Jap., **34** (1983) 548.

[47] J. Li, C. Papadopoulos: Nature, **402** (1999) 253.

[48] N. I. Kovtyukhov, B. R. Martin: Mater. Sci. Engin. C, **19** (2002) 255.

[49] A. Govyadinov, P. Mardilovich: Electrochem. Soc. Porceedings, **28** (2000) 74.

[50] George F. Vander Voort, " Metallography Principles and Practice ", McGraw-Hill book company, 1984.

[51] C. A. Huber, T. E. Huber, Science, 263(1994) 800.

[52] D. Routkevitch, J. M. Xu, Trans. Electron. Dev., 43(1996)1646.

[53] L. Young, " Anodic oxide films", Academic Press, New York, 1961.

[54] D. A. Vermilyea, Adv. Electrochemistry and Electrochemical Eng., 3 (1963) 211.

[55] S. Tajima, Adv. Corros. Sci. and Technology, 1 (1970) 229.

[56] T. P. Hoar, Corros. Sci., 7 (1967) 341.

[57] S. Tajima, Metall., 18 (1964) 581.

[58] P. G. Sheasby, W. E. Cooke, Trans. Ins. Metal Finis., 52 (1974) 103.

[59] British Patent, 223 (1923) 994.

[60] Italian Patent, 741 (19363) 753.

[61] R. Keller and F. hunter: J. Electrochem. Soc., 100 (1953) 411.

[62] H. Lewis and L. Plumb: J. Electrochem., Soc., 105 (1958) 496.

[63] T. Edwards and R. Keller: Metals Technol., 11 Techn. Publ., 1 (1944) 710.

[64] G. E. Thompson and G. C. Wood: Trans. Inst. Metal Finishing 58 (1980) 21.

[65] Spooner, R.C., J. Electrochem. Soc., 102 (1955) 156.

[66] G. C. Wood, J. P. O'Sullivan, Electrochim. Acta, 15 (1970) 1865.

[67] G. C. Wood, A. J. Brock, Nature London, 209 (1968) 773.

[68] A. J. Brock, G. C. Wood, Electrochim. Acta, 12 (1967) 395.

[69] G. Thompson and G. C. Wood, "Anodic films on aluminum", 23 (1983) New York.

[70] O. Jessensky, F. Muller, Appl. Phys. Lett., 72 (1998) 1173.

[71] M. Hill, Nature, 272 (1978) 433.

[72] Setoh, S, Miyata, A., Sci. Pap. Inst. Phys. Chem. Res., Tokyo, (1932) 189.

[73] G. C. Wood, P. Skeldon, J. Electrochem. Soci, 143 (1996) 74.

[74] K. T. Sunil and C. C.Hsueh: Chaos, 12 (2002) 240.

[75] H. Masuda and F. Hasegwa: J. Electrochem. Soc., 144 (1997) 127.

[76] T. Iwasaki, T. Motoi, Appl. Phys, Lett, 75 (1999) 2044.

[77] Y. T. Pang, G. W. Meng, Nanotechnology, 14 (2003) 20.

[78] Y. W. Wang, G. W. Meng, Chem. Phys. Lette., 339 (2001) 174.

[79] V. G. Stoleru, E. Towe, Appl. Phys. Lett., 85 (2004) 5152.

[80] J.P. O'Sullivan, G.C. Wood, Proc. Royal Soc. London A, 317 (1970) 511.

[81] J. W. Diggle, T. C. Downie, Chem. Rev., 69 (1969) 365.

[82] M. S. Hunter, P. Fowel, J. Electrochem. Soc., 101 (1954) 481.

[83] M. S. Hunter, P. Fowel, J. Electrochem. Soc., 101 (1954) 514.

[84] E. Miller: United States Patent, Patent No.: 5747180 (1998).

[85] Akahori, J. Electronmicroscopy, Japan, (1962).

[86] P.P. Mardilovich, A.N. Govyadinov, J.Mem.Sci., 98 (1995) 131.

[87] K. Liu, C.L. Chien: Appl. Phys. Lett.,,73 (1998) 1463.

[88] T.A. Taton, C.A. Mirkin: Science, 289 (2000) 1757.

[89] K.K. Sandhu: Bioconjugate Chem., 13 (2002) 3.

[90] J. Heremans, C.M. Thrush: Phys. Rev., B59 (1999) 12579.

[91] X. F. Wang, L. D. Zhang, J. Phys. D: APPL. Phys. 34 (2001) 418.

[92] H. Yu, P. C. Gibbons, J. mater. Chem., 34 (2004) 595.

[93] T. Y. Tan, N. Li., Appl. Phys. Lett., 83 (2003) 1119.

[94] M. Tian, J. Wang, Appl. Phys. Lett., 83 (2003) 1620.

[95] S. H. Jo, J. Y. Lao, Appl. Phys. Lett., 83 (2003) 4821.

[96] C. Ji, P. C. Season, Appl. Phys. Lett., 81 (2002) 4437.

[97] W. I. Park, D. H. Kim, Appl. Phys. Lett., 80 (2002) 4232.

[98] B. D. Yao, Y. F. Chan, Appl. Phys. Lett., 81 (2002) 757.

[99] J. Y. Lao, J. G. Wen, Nano Lett., 2 (2002) 1287.

[100] D. Banerjee, J. Y. Lao, Appl. Phys. Lett., 83 (2003) 2061.

[101] C. K. Xu, G. D. Xu, Solid State Commun., 122 (2002) 175.

[102] Alexander Moroz, Phys. Rev. Lett., 83 (1999) 5274.

[103] Z. Q.Liu, Z. W. Pan, J. phys. and Chem. of solids, 61 (2000) 1171.

[104] Z. Zhang, D. Gekhtman, Chem. Mater., 11 (1999) 1659.

[105] V. A. Tracey and C. P. Cutler: Powder Met., 24 (1981) 32.

[106] V. Anand and A. J. Kaufman: Rapid Solidification Processing: Principles and Technologies II, Claitor's Publication New York 1980,

273.

[107] A. R. Cox and J. B. Moore: Superalloys Metallurgy and Manufacture, Claitor's Publication New York 1976, 45.

[108] L. Konitzer and K. W. Walters: Met. Trans. B, 15B (1984) 149.

[109] G. Friedman: Proc. AGARD Conf. No. 200 Canada (1976) 1.

[110] J. Devillard and J. P. Herteman: Powder Metallurgy of Titanium Alloys Warrendale, Pa. New York 1980, 59.

[111] R. V. Raman and A. N. Patel: Prog. Powder Met., 38 (1982) 99..

[112] T. S. Daugherty: J. Metals, 16 (1964) 827.

[113] R. G. Reddy: Rev. Adv. Mater. Sci., 5 (2003) 121.

[114] J.A. Dean: Lange's Handbook of Chemistry, McGraw-Hill, New York 14th edition, (1992), 19.

[115] A. Brandes: Semithells Metals Reference Book 6th edition, Butterworth & Co. Publisher Ltd. New York 6th edition (1983), 14-8.

[116] Z. F. Yuan, K. Mukai, J. Coll. and Interface Sci, 254 (2002) 338.

[117] J.A. Dean: Lange's Handbook of Chemistry, McGraw-Hill, New York 14th edition, 1992, 19. Eric

[118] Taylor Lyman, Metals Handbook 8th, American Society for Metals, USA, (1973), 155.

[119] P. Cotterill, and P. R. Mould: Recrystallization and Grain Growth in Metals, Surrey University Press, USA., (1976) 60.

[120] Syverud: JANAF Thermochemical Table, 3rd., ed., J. Phys. Chem. Ref. Data 1985.

[121] John D. Verhoeven: Fundamentals of Physical Metallurgy, John Wiley & Sons Inc, New York (1975) 228.

[122] F. H. Wohlbier: Diffusion and defect data, 1 (1967) 2.

[123] F. H. Wohlbier: Diffusion and defect data, 3 (1969) 469.

[124] J. H. Christian and H. L. Taylor: J. Appl. Phys., 38 (1967) 3843.

[125] F. H. Wohlbier: Diffusion and defect data, 24 (1981) 75.

[126] T. L. Woods, R. M. Garrels, “Thermodynamic Values at Low Temperature for Natural Inorganic Materials.“ Oxford University Press (1987), New York.

[127] M.Tian, J.Wang, Appl. Phys. Lett., 83 (2003) 1620.

[128] NASA Goddard Space Flight Center

[129] M. W. Barsoum, E. N. Hoffman, Phys. Rew. Letts, 93 (2004) 206104-1

[130] Y. Chen, X. Cui, Chemical Phys. Letts., 369 (2003) 16.

[131]N. Furuta, K. Hamamura, Jpn. J. Appl. Phys, 8 (1969) 1404.

[132]X. L.Ma, Y. Li, Chemical Phys. Letts., 376 (2003) 794.

[133]Z. Ying, Q. Wan, Nanotechnology, 15 (2004) 1682.

[134]J. Q.Hu, Y. Bando, Chemical Phys. Letts., 372 (2003) 758.)

[135] W. J. Choi, T. Y. Lee,[136] Syverud, "JANAF Thermochemical Table, 3rd., ed., J. Phys. Chem. Ref. Data, 1985.

# Appendix

## A.1 Electrochemistry of titanium

Using similar process, the active metal of titanium could be polished too. For the titanium EP, highly pure titanium plates (99.995%) with an area of 2 $cm^2 \times 0.5$ cm were used. The specimens were abraded using 4000-grit SiC papers and mechanical polishing by 0.05 μm alumina powder. They were then annealed below the temperature of α - β phase transformation in an air furnace for 1 hour at 800 $^oC$. The EP equipment setup is the same as Fig. 3.1. However, the electrolyte used is 5% perchloric acid ($HClO_4$, 70% ) – 53% ethylene glycol monobutylether ($(CH_3(CH_2)_3OCH_2CH_2OH)$, 85%) - 42% methanol ($CH_3OH$, 99%). 52 V were applied for one minute, followed by 28 volts and 70 $mA/cm^2$ for 14 min, at a constant stirring rate of 200 rpm. The morphology of titanium surface after EP was observed by optical microscopy (OM), showed as Fig. A.1

Compared to AAO process, the ATO template process is easier than the AAO process. The EP for the surface of titanium used a single anodization by 1.2 vol. % hydrofluoric acid (HF, 55%) + 10 vol. % sulphuric acid ($H_2SO_4$, 98%) electrolyte at 25 $^oC$ and 20 V for 90 seconds. The SEM image of the ATO template is shown in Fig. A.2, and the flow sheet of ATO process is shown in Fig. A.3.

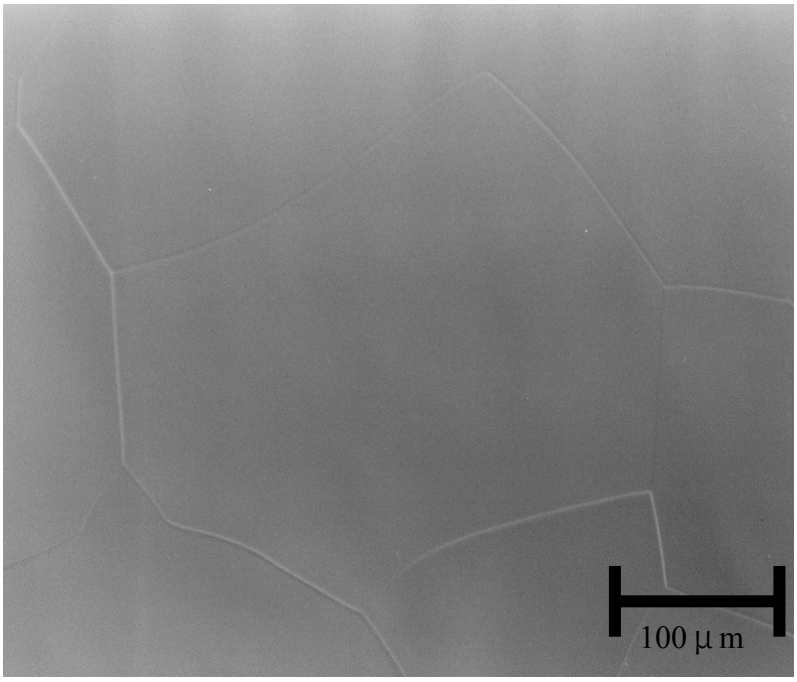


***Fig. A.1*** *The optical microscopy image of titanium surface after electropolishing.*

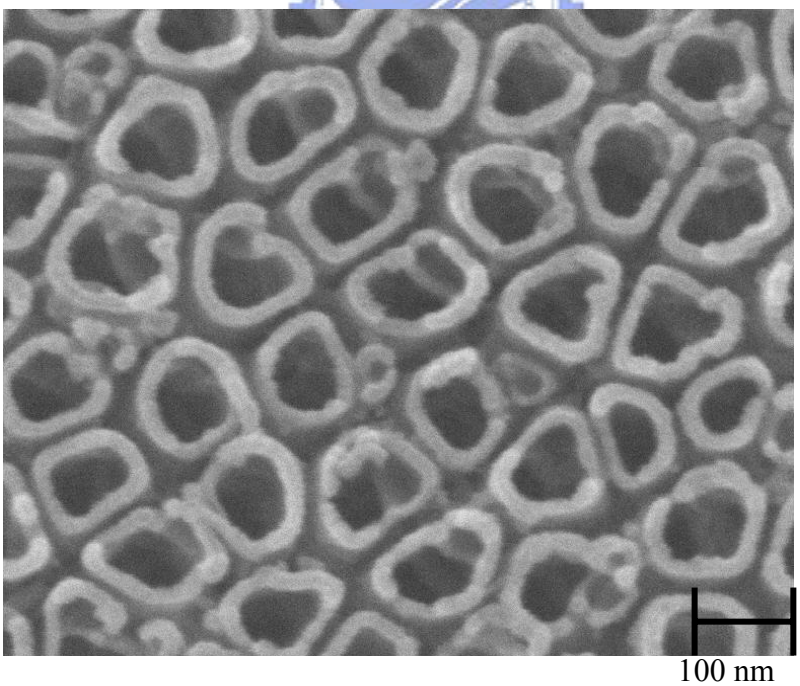


**Fig. A.2** The SEM image of ATO.

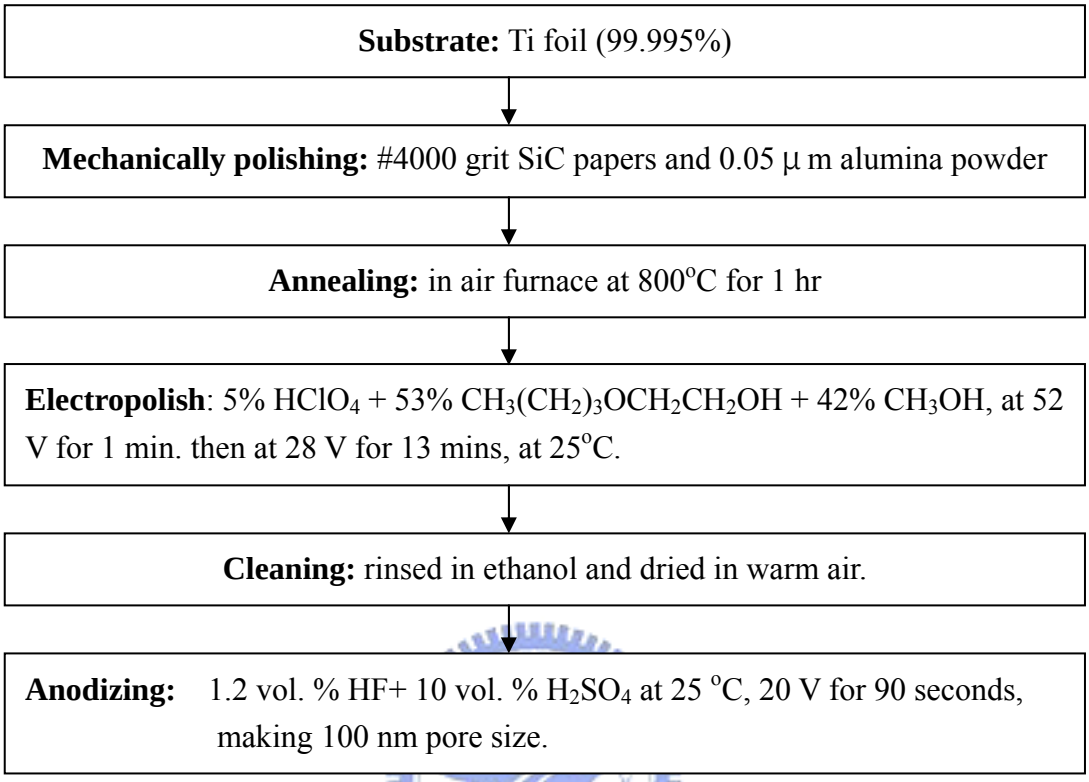


**Fig. A.3** The flow sheet of ATO process.

## A.2 Electropolishing of Ti

Based on the AAO fabrication process, nanotemplate of anodic titanium oxide (ATO) could form on the titanium. Titanium is an active metal similar to aluminum; its surface is always covered with a dense oxide layer when it is in the ambient atmosphere. The oxide layer could form a template with ordered nanotubes under the controlling of electrochemical processes. Figure A.4 shows the electrolytic polishing (EP) curve of titanium. Polishing is performed at the plateau (C); the oxide film is removed from the substrate at low voltage (A), etching is performed at (B), and gas is evolved and pitting occurs at high voltages (D). The appropriate polishing voltage for titanium was between 20 and 39 V; 28V was chosen as the working voltage of anodization in this experiment. The EP process initially formed the black porous film, which had to be removed as quickly as possible. Two methods could be used to remove the film: the first is to increase the voltage; the second is to increase the stirring rate in the electrolyte. However, increasing the stirring rate can easily cause over polishing. In this study, the voltage was initially modified to 53V for one minute and then the working voltage reduced to 28V for 14 min. Hence, the cleaning and plating of the grains of α-phase Ti could be observed clearly. By the way, the lamellar microstructure of β-phase (Fig. A.5(a)) Ti is less flat than α-phase (Fig. A.5(b)) Ti. Therefore, in order to obtain a flat EP surface of Ti, the sample should be annealed in the α-phase before EP.

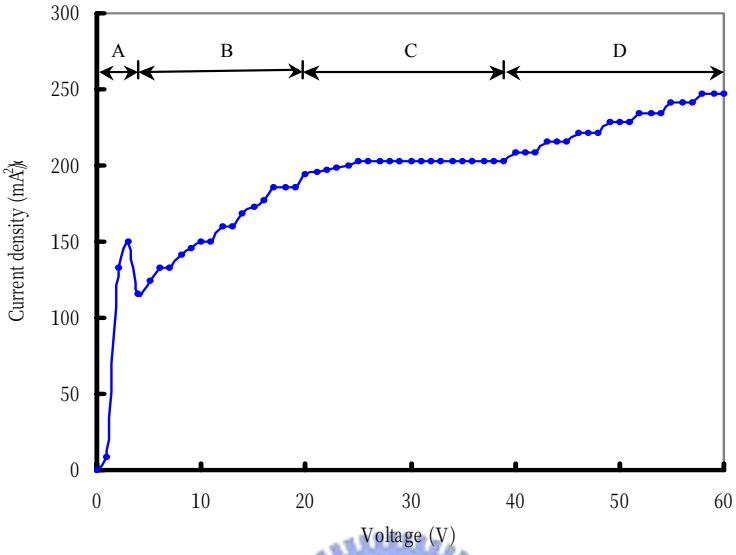


**Fig. A.4** The electro-polishing curve of titanium.

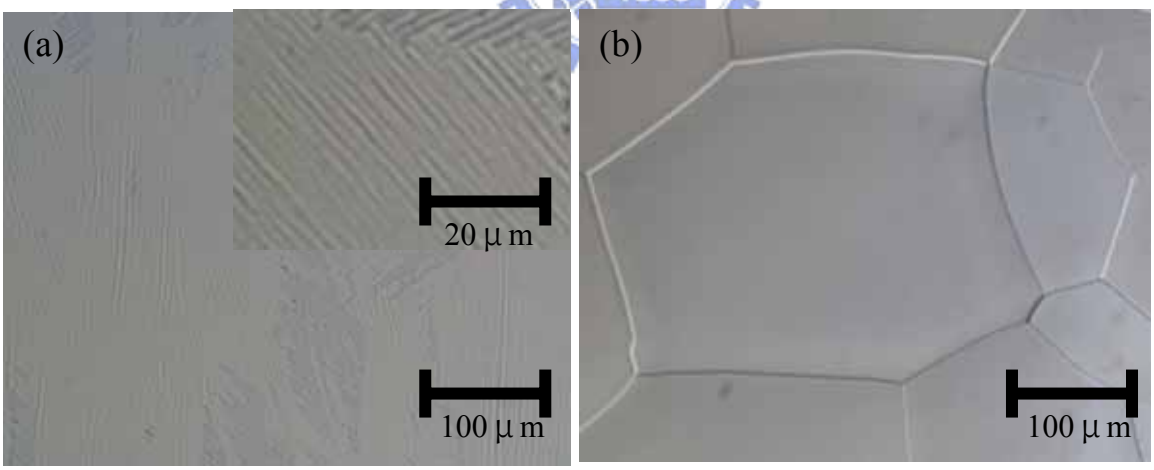


**Fig. A.5** The OM images of EP on β phase (a), and α phase Ti surface (b).

Figure A.6 displays a series of optical micrographs of EP obtained after various polishing times. EP was rough after it was abraded using 1500-grit SiC papers, as in Fig. A.6 (a). Polishing from 1 to 14 min, as shown in Figs. A.6 (b) - (h) did not suffice; the black porous film was removed first and the surface of the substrate was bright. The grain-boundary was observed but unclearly, after three minutes. Increasing polishing time caused the grain-boundary to become distinct and the surface to become smooth. A favorable polishing time was 14 min, after which time the surface was flat, without scrapes with no pitting: as in Fig. A.6 (i). When the polishing time exceeded 14 min, the grain-boundary was over-etched and the grain became pitted, as shown in Figs. A.6 (j) - (l).

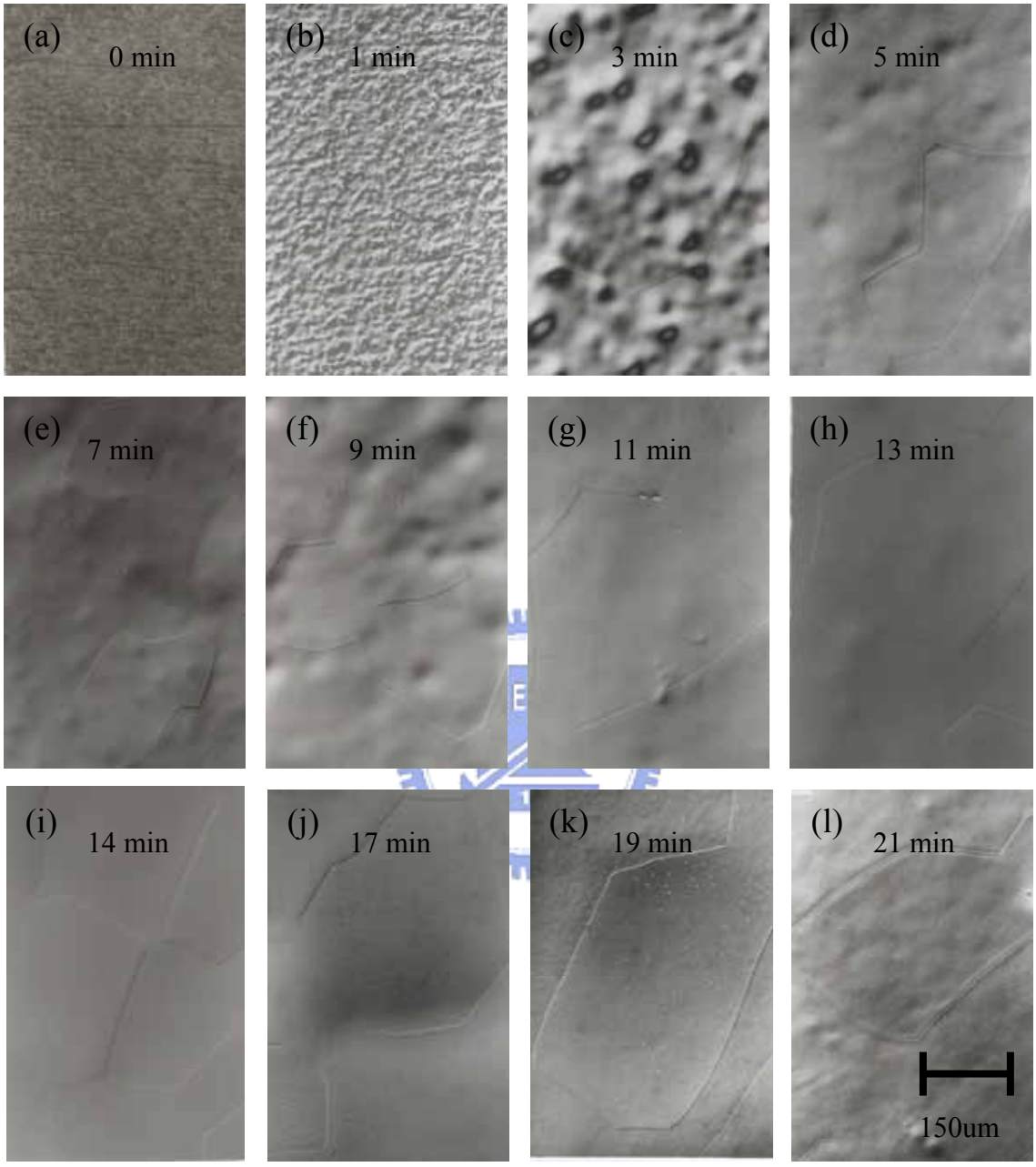


**Fig.** A.6. The optical micrographs of electro-polishing progress from 1 to 21 minutes on the titanium surface; (a) original titanium surface; (b)-(h) insufficient polishing, 1 to 13 minutes; (i) suitable polishing, 14 minutes; (j)-(k) excess polishing, 17 to 21 minutes.

## A.3 Pourbaix diagram of Ti

Immersing the titanium in electrolyte generated various substance of titanium ions and titanium oxide. They included nine solids: titanium ($Ti$), titanium monoxide ($TiO$), hypotitanous hydroxide ($TiO \cdot H_2O$ or $Ti(OH)_2$), titanium sesquioxide ($Ti_2O_3$), titanium hydroxide ($Ti_2O_3 \cdot H_2O$ or $Ti(OH)_3$), blue oxide ($Ti_3O_5$), titanium dioxide or rutile **($TiO_2$),** hydrated dioxide ($TiO_2 \cdot H_2O$ or $Ti(OH)_4$), hydrated peroxide ($TiO_3 \cdot 2H_2O$)and seven dissolved substances hypotitanous: ions ($Ti^{+2}$),titanous ions ($Ti^{+3}$), titanyl ions ($TiO^{+2}$), titanate ions ($HTiO_3^-$), pertitanyl ions ($TiO_2^{+2}$), acid pertitanate ions ($HTiO_4^-$) and pertitanate ions ($TiO_4^{-2}$). [36] A complex reaction occurs among the 16 forms of titanium in aqueous solution. The Pourbaix diagram is useful in simplifying the complex reaction. The diagram is constructed by considering the Gibbs free energy and the Nernst equation. In the Tab. A.1, the reactions and equations that involve Ti, $Ti^{+2}$, $Ti^{+3}$, $TiO^{+2}$, $TiO_2^{+2}$, TiO, $HTiO_3^-$, $Ti(OH)_3$ and $TiO_2 \cdot H_2O$ are used to construct a Pourbaix diagram of titanium in aqueous electrolyte. Based on Tab. A.1, when the 22 reactions are placed on the pH – V diagram, the initial Ti Pourbaix diagram can be constructed, as in Fig. A.7. Furthermore, the final Ti Pourbaix diagram showed as Fig. A.8.

## A.4 Anodizing of titanium

A dense oxide film was formed on the titanium surface when the electrolyte was 10 vol% $H_2SO_4$; however, an ordered nanochannel-array of ATO was obtained when 1.2 vol % HF was added to the sulfuric acid base electrolyte. Figure A.9(a) presents a plane view of an SEM micrograph image of ATO that was anodized in 1.2 vol. % HF+ 10 vol % $H_2SO_4$ as an electrolyte at 25 $^{o}$C and 20 V for 90 seconds. The long-range ordered nano-channel had a 170 nm-thick film, pores with a diameter of 100 nm, an inter-pore distance of 120 nm, a 25 nm-thick pore wall, a pore density of $8\times10^{9}$ pores/cm$^2$ and a porosity of 68.2%. Figure A.9(b) shows the barrier layer on the bottom of ATO. In addition, the color on the titanium surface changed from blue to almost transparent during the initial anodizing process to the final porous film form, because a 68.2 % porous film formed on the ATO, reducing the interference between the titanium and ATO. The detailed SEM images of ATO forming in various anodization time between 10 ~ 90 sec, showed as Figs. A.10(a) - (i). Numerous gases $TiF_{(g)}$, $TiF_{2(g)}$, $TiF_{3(g)}$, $TiF_{4(g)}$, $TiOF_{(g)}$ and $TiOF_{2(g)}$ are formed in the Ti-F-O system, according to the thermochemical data [37, 38]. When the titanium is anodized, the above gases and $H_{2(g)}$ escape from the titanium substrate through titania film, leaving nanopores and forming ATO. The Pourbaix diagram of titanium shows that Ti dissolved as cations when the pH of the electrolyte was under 2.5, and the standard electrode potential exceeded –1.81 V (SHE). Applying a constant voltage of 20V to the titanium

**Tab.** A.1 The chemical reactions and Nernst's law when titanium is immersed in aqueous solution.

| *No.* | **Oxidation number** | **Reactions** | **Equations** | **Coexistence items** | **Brief equations** |
|---|---|---|---|---|---|
| *1* | **+4** | $TiO^{+2} + 2H_2O \rightarrow HTiO_3^- + 3H^+$ | $\log \frac{[HTiO_3^-]}{[TiO^{+2}]} = -16.82 + 3pH$ | $TiO^{+2}$ / $HTiO_3^-$ | $pH = 5.64$ |
| *2* | **+2 → +3** | $Ti^{+2} \rightarrow Ti^{+3} + e^-$ | $E_o = -0.368 + 0.0591 \log \frac{[Ti^{+3}]}{[Ti^{+2}]}$ | $Ti^{+2}$ / $Ti^{+3}$ | $E_o = -0.368$ |
| *3* | **+2 → +4** | $Ti^{+2} + H_2O \rightarrow TiO^{+2} + 2H^+ + 2e^-$ | $E_o = -0.135 - 0.0591pH + 0.0295 \log \frac{[TiO^{+2}]}{[Ti^{+2}]}$ | $Ti^{+2}$ / $TiO^{+2}$ | $E_o = -0.135 - 0.0591pH$ |
| *4* | **+2 → +4** | $Ti^{+2} + 3H_2O \rightarrow HTiO_3^- + 5H^+ + 2e^-$ | $E_o = 0.362 - 0.1475pH + 0.0295 \log \frac{[HTiO_3^-]}{[Ti^{+2}]}$ | $Ti^{+2}$ / $HTiO_3^-$ | $E_o = 0.362 - 0.1475pH$ |
| *5* | **+3 → +4** | $Ti^{+3} + H_2O \rightarrow TiO^{+2} + 2H^+ + 2e^-$ | $E_o = 0.100 - 0.1182pH + 0.0591 \log \frac{[TiO^{+2}]}{[Ti^{+3}]}$ | $Ti^{+3}$ / $TiO^{+2}$ | $E_o = 0.100 - 0.1182pH$ |
| *6* | **+4 → +6** | $TiO^{+2} + H_2O \rightarrow TiO_2^{+2} + 2H^+ + 2e^-$ | $E_o = 1.800 - 0.0591pH + 0.0295 \log \frac{[TiO_2^{+2}]}{[TiO^{+2}]}$ | $TiO^{+2}$ / $TiO_2^{+2}$ | $E_o = 1.800 - 0.0591pH$ |
| *7* | **+4 → +6** | $HTiO_3^- + H^+ \rightarrow TiO_2^{+2} + H_2O + 2e^-$ | $E_o = 1.303 + 0.0295pH + 0.0295 \log \frac{[TiO_2^{+2}]}{[HTiO_3^-]}$ | $HTiO_3^-$ / $TiO_2^{+2}$ | $E_o = 1.303 - 0.0295pH$ |
| *8* | **0 → +2** | $Ti + H_2O \rightarrow TiO + 2H^+ + 2e^-$ | $E_o = -1.306 - 0.0591pH$ | $Ti$ / $TiO$ | $E_o = -1.306 - 0.0591pH$ |

| | | | | | |
|---|---|---|---|---|---|
| 9 | +2 → +3 | $2TiO + H_2O \rightarrow Ti_2O_3 + 2H^+ + 2e^-$ | $E_o = -1.123 - 0.0591\,pH$<br>$E_o = -0.894 - 0.0591\,pH$ for hydroxide | $TiO / Ti_2O_3$<br>$TiO / Ti(OH)_3$ | $E_o = -1.123 - 0.0591\,pH$<br>$E_o = -0.894 - 0.0591\,pH$ |
| 10 | +3 → +3.3 | $2Ti_2O_3 + H_2O \rightarrow 2Ti_3O_5 + 2H^+ + 2e^-$ | $E_o = -0.490 - 0.0591\,pH$<br>$E_o = -1.178 - 0.0591\,pH$ for hydroxide | $Ti_2O_3 / Ti_3O_5$<br>$Ti(OH)_3 / Ti_3O_5$ | $E_o = -0.490 - 0.0591\,pH$<br>$E_o = -1.178 - 0.0591\,pH$ |
| 11 | +3 → +4 | $Ti_2O_3 + H_2O \rightarrow 2TiO_2 + 2H^+ + 2e^-$ | $E_o = -0.5560 - 0.0591\,pH$<br>$E_o = -0.091 - 0.0591\,pH$ for hydroxide | $Ti_2O_3 / TiO_2$<br>$Ti(OH)_3 / TiO_2 \cdot H_2O$ | $E_o = -0.5560 - 0.0591\,pH$<br>$E_o = -0.091 - 0.0591\,pH$ |
| 12 | +3.3 → +4 | $Ti_3O_5 + H_2O \rightarrow 3TiO_2 + 2H^+ + 2e^-$ | $E_o = -0.589 - 0.0591\,pH$<br>$E_o = -0.453 - 0.0591\,pH$ for hydroxide | $Ti_3O_5 / TiO_2$<br>$Ti_3O_5 / TiO_2 \cdot H_2O$ | $E_o = -0.589 - 0.0591\,pH$<br>$E_o = -0.453 - 0.0591\,pH$ |
| 13 | +2 → 0 | $Ti^{+2} + H_2O \rightarrow TiO + 2H^+$ | $\log[Ti^{+2}] = 10.91 - 2\,pH$ | $Ti^{+2} / TiO$ | $pH = 8.455$ |
| 14 | +3 → 0 | $2Ti^{+3} + 3H_2O \rightarrow Ti_2O_3 + 6H^+$ | $\log[Ti^{+3}] = -8.09 - 3\,pH$<br>$\log[Ti^{+3}] = 2.03 - 3\,pH$ for hydroxide | $Ti^{+3} / Ti_2O_3$<br>$Ti^{+3} / Ti(OH)_3$ | $pH = -0.69$<br>$pH = 2.68$ |
| 15 | +4 → 0 | $TiO^{+2} + H_2O \rightarrow TiO_2 + 2H^+$ | $\log[TiO^{+2}] = -12.94 - 2\,pH$<br>$\log[TiO^{+2}] = -1.18 - 2\,pH$ for hydroxide | $TiO^{+2} / TiO_2$<br>$TiO^{+2} / TiO_2 \cdot H_2O$ | $pH = -3.47$<br>$pH = 2.41$ |
| 16 | +4 → 0 | $HTiO_3^- + H^+ \rightarrow TiO_2 + H_2O$ | $\log[HTiO_3^-] = -29.76 + 1\,pH$<br>$\log[HTiO_3^-] = -18 + 1\,pH$ for hydroxide | $HTiO_3^- / TiO_2$<br>$HTiO_3^- / TiO_2 \cdot H_2O$ | $pH = 23.76$<br>$pH = 12$ |

| | | | | | |
|---|---|---|---|---|---|
| 17 | 0 → +2 | $Ti \rightarrow Ti^{+2} + 2e^{-}$ | $E_o = -1.630 + 0.0295\log[Ti^{+2}]$ | $Ti / Ti^{+2}$ | $E_o = -1.807$ |
| 18 | +2 → +3 | $2Ti^{+2} + 3H_2O \rightarrow Ti_2O_3 + 6H^{+} + 2e^{-}$ | $E_o = -0.478 - 0.1773\,pH - 0.0591\log[Ti^{+2}]$<br>*for hydroxide*<br>$E_o = -0.248 - 0.1773\,pH - 0.0591\log[Ti^{+2}]$ | $Ti^{+2} / Ti_2O_3$<br>$Ti^{+2} / Ti(OH)_3$ | $E_o = -0.123 - 0.1773\,pH$<br>$E_o = 0.107 - 0.1773\,pH$ |
| 19 | +2 → +4 | $Ti^{+2} + 2H_2O \rightarrow TiO_2 + 4H^{+} + 2e^{-}$ | $E_o = -0.502 - 0.1182\,pH - 0.02951\log[Ti^{+2}]$<br>*for hydroxide*<br>$E_o = -0.169 - 0.1182\,pH - 0.02951\log[Ti^{+2}]$ | $Ti^{+2} / TiO_2$<br>$Ti^{+2} / TiO_2 \cdot H_2O$ | $E_o = -0.325 - 0.1182\,pH$<br>$E_o = 0.008 - 0.1182\,pH$ |
| 20 | +3 → +4 | $Ti^{+3} + 2H_2O \rightarrow TiO_2 + 4H^{+} + e^{-}$ | $E_o = -0.666 - 0.2364\,pH - 0.0591\log[Ti^{+3}]$<br>*for hydroxide*<br>$E_o = 0.029 - 0.2364\,pH - 0.0591\log[Ti^{+3}]$ | $Ti^{+3} / TiO_2$<br>$Ti^{+3} / TiO_2 \cdot H_2O$ | $E_o = -0.311 - 0.2364\,pH$<br>$E_o = 0.384 - 0.2364\,pH$ |
| 21 | +3 → +4 | $Ti_2O_3 + 3H_2O \rightarrow 2HTiO_3^{-} + 4H^{+} + 2e^{-}$ | $E_o = -0.601 - 0.1182\,pH + 0.0591\log[HTiO_3^{-}]$<br>*for hydroxide*<br>$E_o = 0.973 - 0.1182\,pH + 0.0591\log[HTiO_3^{-}]$ | $Ti_2O_3 / HTiO_3^{-}$<br>$Ti(OH)_3 / HTiO_3^{-}$ | $E_o = -0.246 - 0.1182\,pH$<br>$E_o = 0.618 - 0.1182\,pH$ |
| 22 | +4 → +6 | $TiO_2 \rightarrow TiO_2^{+2} + 2H^{+} + 2e^{-}$ | $E_o = 2.182 + 0.0295\log[TiO_2^{+2}]$<br>*for hydroxide*<br>$E_o = 1.835 + 0.0295\log[TiO_2^{+2}]$ | $TiO_2 / TiO_2^{+2}$<br>$TiO_2 \cdot H_2O / TiO_2^{+2}$ | $E_o = 2.005$<br>$E_o = 1.658$ |

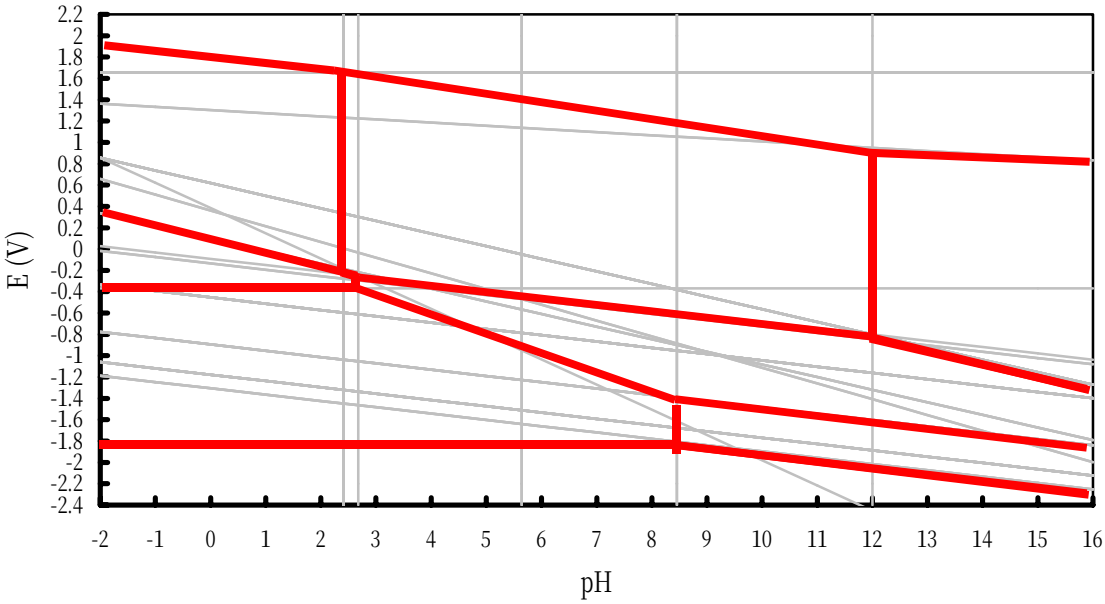


**Fig.** A.7 The initially Ti Pourbaix diagram constructed by 22 reactions.

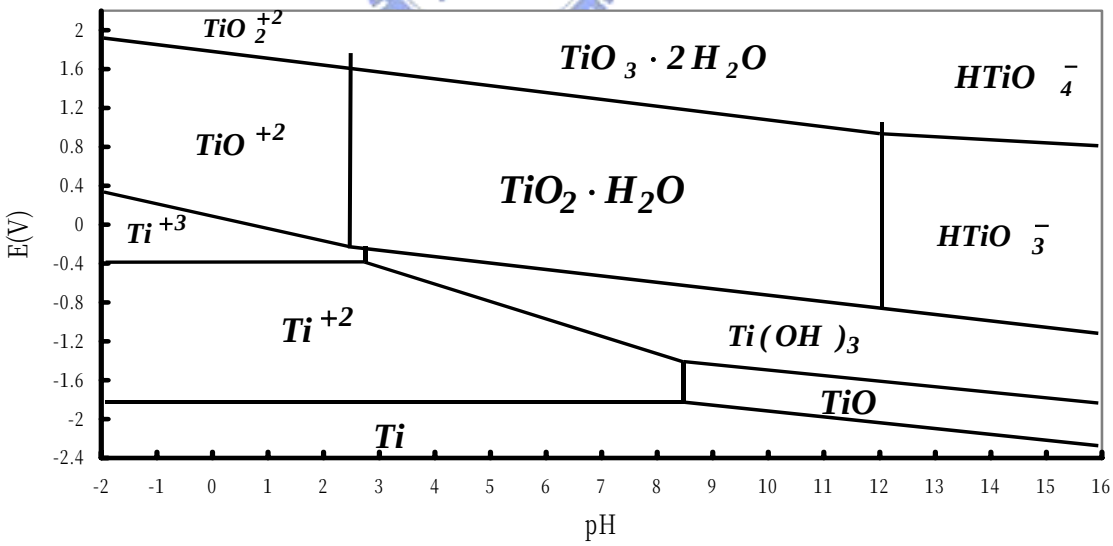


**Fig.** A.8 The Pourbaix diagram of titanium in electrolytes

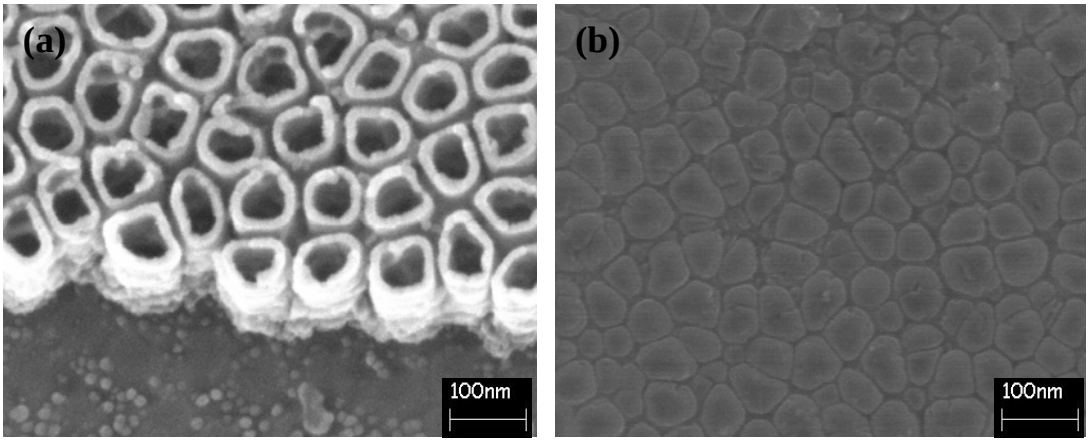


**Fig.** A.9 10% $H_2SO_4$ + 1.2% HF as the electrolyte, the ordered nanochannel array of ATO formed on the surface of titanium; (a) nanochannel of top view, (b) barrier layer of bottom view.

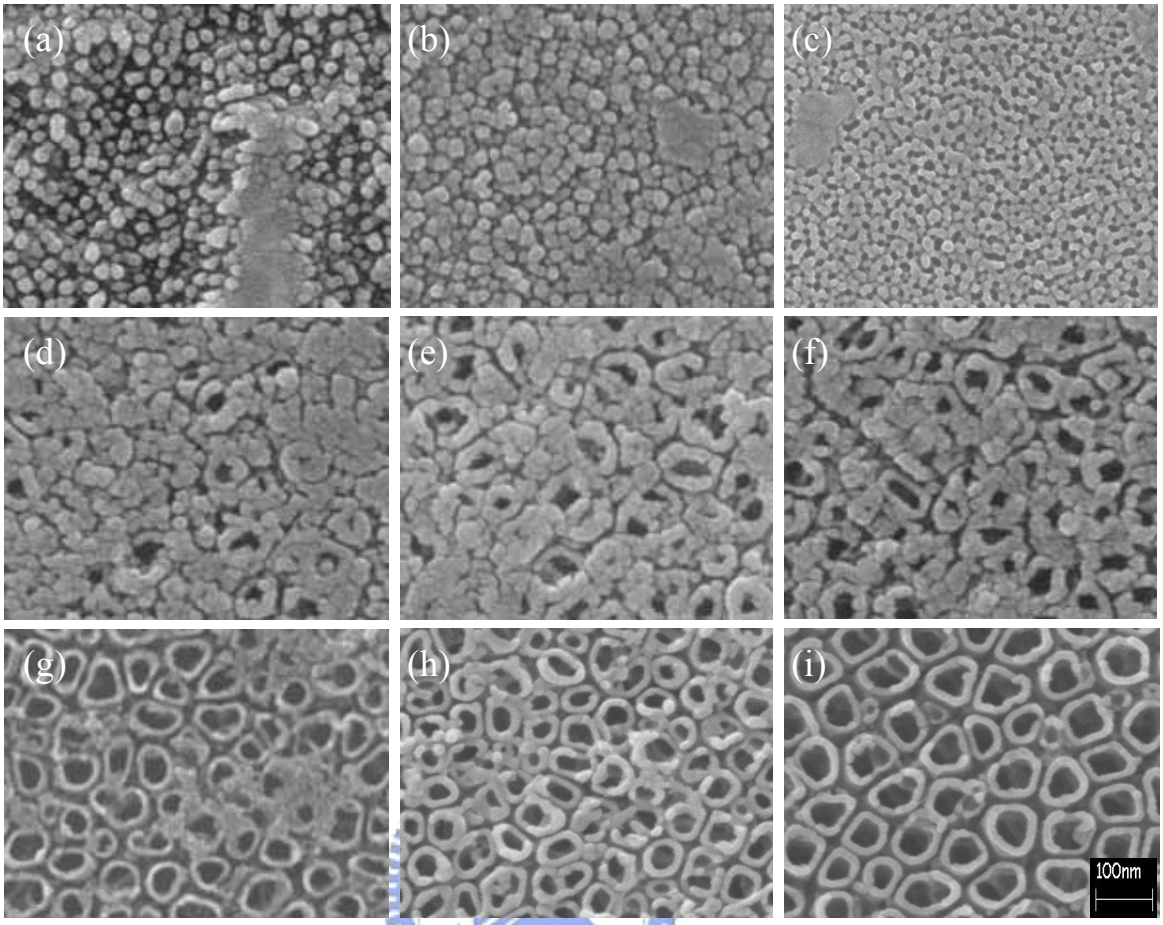


**Fig.** A.10 The SEM images of ATO forming when anodization time at 10 sec (a), 20 sec (b), 30 sec (c), 40 sec (d), 50 sec (e), 60 sec (f), 70 sec (g), 80 sec (h), and 90 sec

effectively dissolved Ti according to $Ti \rightarrow Ti^{+2} \rightarrow TiO^{+2}$. $TiO^{+2}$ combined easily with $OH^-$ to form $TiO_2$. $H_2O$ or $Ti(OH)_4$ when the pH of the solution of titanly ions $TiO^{+2}$ was increased to yield strongly acidic conditions. The enthalpy of formation of the precipitate of $Ti(OH)_4$ is unknown. It is an unstable substance, which changes gradually, by dehydration, into $TiO_2$. $H_2O$. A thin film of titania always forms on the surface of titanium after it is anodized. The thin film interference effect makes the thin $TiO_2$ film formed

on the titanium surface easy to observe. In the experiment performed herein, when the electrolyte was 10% $H_2SO_4$ as, anodizing produced a dense dark blue oxidized layer on the titanium. The reaction equations as: Reacts. (21) and (22). When HF added in the $H_2SO_4$ electrolyte, the anodic Ti changes to Reactions (23) and (24).

$$TiO^{+2} + 6OH^- + 2e^- \rightarrow Ti(OH)_4 + H_2 + 3O^{-2} \quad \text{.....(21)}$$

$$TiO^{+2} + 2OH^- \rightarrow TiO_2 \cdot H_2O \quad \text{.....(22)}$$

$$TiO^{+2} + 6OH^- + 2e^- + F^- + S^{-2} \rightarrow Ti(OH)_{4(s^{-2},F^- \text{ in the porous film})} + H_{2(g)} + 3O^{-2}$$

$$\text{.....(23)}$$

$$TiO^{+2} + 2OH^- + F^- + S^{-2} \rightarrow TiO_2 \cdot H_2O_{(S^{-2},F^- \text{ in the porous film})} \quad \text{.....(24)}$$

## A.5 Decomposition of ATO

The AAO or ATO were always used as the templates for nanorolds, nanodots or nanowires fabrication. Whenever it was necessary to obtain net nanowires, it's necessary to remove AAO or ATO, which is done by immersing the templates in the basic NaOH solution, acid $H_3PO_4$ solution or dilute HF solution. However, it's easy to pollute the nanowires which were filling inside of the template. Therefore, a dry method was used to remove the template in order to avoid the solution pollution. Generally, when $TiO_2$ is in the chamber with an argon furnace ($P_{O2}$= 4×$10^{-9}$ atm), the temperature should be higher than 2505 °C, so that the $TiO_2$ can be decomposed. However, in the same conditions for the porous ATO, when the temperature was at 581 °C, the ATO was removed from the substrates easily. We also checked the critical temperature by differential thermal analysis (DTA). The samples were tested with high purity argon contained at $P_{O2}$= 4×$10^{-9}$ atm in the chamber. Fig. A.11 shows that a clear exothermic peak was observed at 581 °C for porous ATO.

On the other hand, for dense ATO or porous but non-electrolytic polishing ATO, there have not been any decomposed peaks in the diagram. The decomposition equation of dense titania can be expressed as:

$$TiO_{2(s)} \rightarrow Ti_{(s)} + O_{2(g)} \quad \text{.....(25)}$$

the equilibrium partial oxygen pressure could be calculated from

$$\log P_{O_2} = \frac{\Delta G_f^o}{-19.147T} \quad \text{.....(26)}$$

the $\Delta G_f^o$ in the equation (25) for dense $TiO_2$ bulk is 833.97 kJ/mol [135]. at 581 $^oC$ therefore, the partial pressure of oxygen should be lower than $10^{-50.94}$ atm in the equation (26) that titania can decompose. However, the nanochannel ATO has more defects or pores than dense titania therefore, the decomposition of the partial oxygen pressure was just $4\times10^{-9}$ atm at 581 $^oC$, and the $\Delta G_f^o$ can be calculated as 137.48 kJ/mol.. The cluster of titania is easy to decompose depending on the cluster size deduced. The following equation is used to describe the possibility of titania decompose depended on the cluster size [117]:

$$\Delta G = \Delta G_v + \Delta G_\gamma \quad \text{.....(27)}$$

where $\Delta G$ is the free energy associated with the formation of the cluster, $\Delta G_v$ is the free energy associated with the volume of cluster, and $\Delta G_\gamma$ is the energy of the surface that is created. Since the surface energy depends on the area of the particle and the volume energy depends on its volume, it may be writing as:

$$\Delta G = A_1 h_1 r^2 + A_2 h_2 r \quad \text{.....(28)}$$

where $A_1$ and $A_2$ are constants, $h_1$ and $h_2$ are the thickness of clusters, and $r$ is the compound radius. When the cluster radius is enough small, the surface free energy is larger than the volume free energy, and the total free energy is positive, therefore the particle is not stable. The ATO with nanochannels had a 68.2 % porosity, and 25 nm pore wall thickness. Therefore, a large area and small radius of $TiO_2$ was exposed in the argon

chamber. Even when the partial oxygen pressure was $4 \times 10^{-9}$ atm, the $TiO_2$ could be discomposed at 581 $^{o}$C, and the Gibbs free energy reduced from 833.97 kJ/mole to 137.48 kJ/mole.

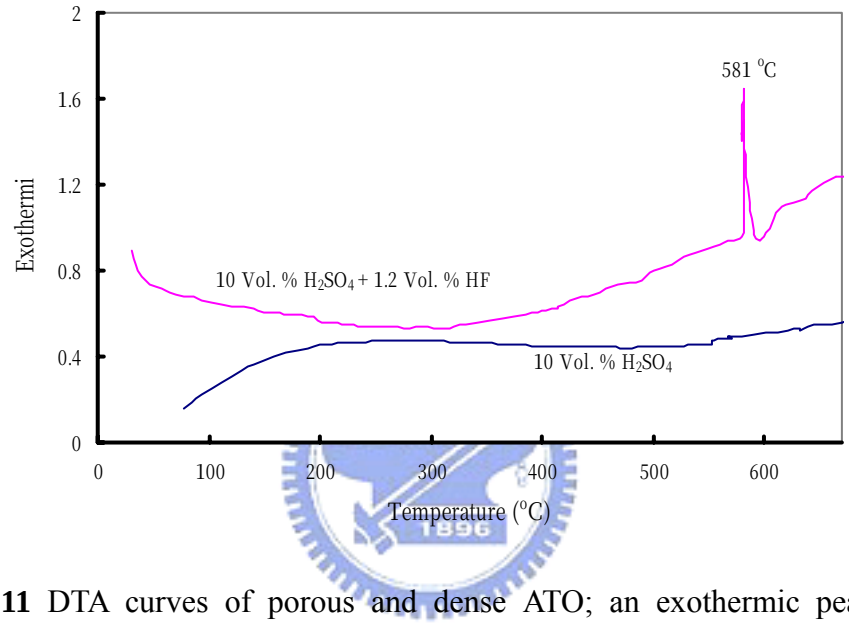


**Fig. A.11** DTA curves of porous and dense ATO; an exothermic peak was detected at 581$^{o}$C for porous ATO, but no any peak be detected relatively dense ATO until 670 $^{o}$C.